Faculty of Aerospace Engineering

Micromechanical Modelling of Fracture Behaviour in Self-Healing Thermal Barrier Coatings

S. Murali

November 16th 2017

Delft University of Technology

Challenge the future

Micromechanical Modelling of Fracture Behaviour in Self-Healing Thermal Barrier Coatings

MASTER OF SCIENCE THESIS

For obtaining the degree of Master of Science in Aerospace Engineering
at Delft University of Technology

S. Murali

November 16th 2017

Faculty of Aerospace Engineering · Delft University of Technology

Delft University of Technology

DELFT UNIVERSITY OF TECHNOLOGY
DEPARTMENT OF
AEROSPACE STRUCTURES AND MATERIALS

The undersigned hereby certify that they have read and recommend to the Faculty of Aerospace Engineering for acceptance a thesis entitled **“Micromechanical Modelling of Fracture Behaviour in Self-Healing Thermal Barrier Coatings”** by **S. Murali** in partial fulfillment of the requirements for the degree of **Master of Science**.

Dated: November 16th 2017

Readers:

Dr. S.R. Turteltaub

Prof.dr.ir. S. van der Zwaag

Dr. B. Chen

Abstract

Crack initiation and propagation in composite structures exists as a prominent knowledge gap in computational fracture mechanics. Prior to the development and implementation of fracture modules in FEM solvers, most studies were constrained to simple geometries and load cases. The set of parametric studies that constitute this thesis aims to partially fill this knowledge gap by studying the fracture behavior of air-plasma sprayed thermal barrier coatings (APS-TBCs) using cohesive zone modelling (CZM) in conjunction with FEM. Two-dimensional projections of the TBC microstructures were developed and subjected to a thermomechanical analysis involving thermal strains between the different components of the TBC system. The parametric study was split into three sections. The preliminary study, set O, was executed to discern the most appropriate set of boundary conditions that would produce realistic crack patterns in an expedient manner. Set A and Set B studied the fracture behaviour of conventional TBCs and the recently developed self-healing TBC composite, comprised of lamellae and pores and for Set B, self-healing particles. Qualitative observations reveal the influence of feature dimensions and relative placement to one another. The results appear to indicate that TBC top-coats that are comprised of finer lamellae exhibit higher fracture resistance on both conventional and self-healing systems, and that smaller particles in self-healing systems mitigate damage caused by pores less than larger particles.

Contents

List of Figures

Chapter 1

Introduction

Thermal Barrier Coatings (TBC) are heat insulating coatings pre-eminently used to augment the combustive efficiency of aircraft turbine engines extending the allowable temperature range for the gas in the interior while keeping the structural components at a level temperature. A TBC system traditionally consists of two main components (excluding the substrate) categorized as the Top Coat (TC) and Bond Coat (BC). The TC performs the intended function of the system by reducing the heat flow between the outside environment and the substrate. It is usually a refractory material that exhibits a high melting point, low thermal conductance, good thermal stability, and a coefficient of thermal expansion close in range to that of the substrate and the BC. TBC top coats are normally composed of zirconia in combination with a stabilizing agent, with the state-of-the-art commercial variation being 7-8wt% ytrria-stabilized zirconia (YSZ). The BC, aside from adhering the TC to the substrate, also protects the substrate from oxidation through the formation of an intermediate layer that attenuates oxygen diffusion towards the substrate. Since the oxygen permeability of the TC may be quite high, the BC composition is selected so that the resulting oxide, known as the thermally grown oxide (TGO), exhibits minimum phase transformation kinetics during oxidation so as to minimize any damage that may occur due to residual stresses. Generally speaking, the BC selection procedure typically involves a trade-off between oxidation and corrosion. The two most used BC compositions are NiAl and MCrAlY (when M is typically either cobalt or nickel, and Y is composed of reactive elements such as yttrium, hafnium, or silicon).

Numerous TBC deposition methods exist, but the two most prevalently used are air-plasma spraying (APS) and electron-beam physical vapor deposition (EB-PVD). This work mainly concerns TBCs fabricated through the former method. Plasma spraying consists of firstly molting the TBC precursor powder at approximately 10 000 K. The high-temperature liquid is subsequently deposited onto the substrate, where it will flatten and solidify into minute pancake-like units know as splats which accumulate to form the coating. APS-TBCs can be recognized by their porous morphology interspersed with many microcracks that form from thermal stresses that occur during the cool-down phase that follows the high-temperature deposition. Typical APS-TBC systems are comprised of a top-coat which provides the main heat-protection function and a bond coat, which allows the top-coat to adhere to the substrate. The bond-coat also protects the substrate from oxidation by oxidating first, engendering a tertiary layer known as the thermally-grown oxide (TGO) between the TC and BC. While it may at first sight appear that the irregularity of the microstructure will act as a detriment to the coating performance, the pores and pre-existing cracks actually enhances coating performance by decreasing thermal conductivity (thereby reducing heat flow across the thickness) and relieving thermal expansion stresses that occur during operation, respectively. Nevertheless, the characteristic inhomogeneity of the APS-TBC microstructure, in conjunction with its sensitivity to multiple environmental variables, makes life-cycle prediction and fatigue behaviour of the APS-TBC a complex endeavor. Generally speaking, the durability of APS-TBCs produced from YSZ will rapidly decrease when exposed to temperature cycles above 1300°C, or the temperature when the composition is no longer stable, and therefore will degrade. At temperature cycles below this point, numerous mechanisms contribute to spallation of the top coat, the most common failure mode. These mechanisms include stress concentrations that occur at the rough TC/BC interface, gradual TGO growth, thermal mismatch strains between the various layers and property degradation due to hot corrosion and sintering.

A recent attempt to prolong the operative life of YSZ-based TBCs has consisted of developing a composite coating to produce a "self-healing" variation of the traditional TBC set-up, comprised of a 7-8wt% YSZ matrix and $MoSi_2$ particulate fillers acting as the healing agent. In such a system, cracks that propagate towards a healing capsule will ideally rupture the capsule, which will subsequently discharge the healing agent. The healing agent will then oxidize into a solid that will fill the penetrating crack and other flaws within its proximity. This attempt at prolonging the lifetime of the coating is markedly different from the traditional approach of fine tuning the microstructure to attain damage resistant material properties. It must be noted that in this traditional approach, longevity may be attained at the cost of another relevant property, such as thermal conductance. The self-healing philosophy circumvents such a trade-off by enabling the material to regain a portion of its functionality that will inevitably deteriorate with use. Taking into the consideration the TBC operating environment, the choice of a filler material is constrained by three main requirements. Firstly, the healing agent must remain solid at the operating temperature range (15-2000 °C). A liquid filler is unacceptable since they may introduce excessive thermal strain to the system because of their higher CTE and higher thermal conductivity levels. Secondly, the agent must form into a liquid when penetrated by the crack. Lastly the liquid/viscous solution secreted into the crack must transform into a solid by chemically reacting with the matrix material. $MoSi_2$ is an appropriate choice since it shows a tendency to flow when alloyed with boron while at the same time possessing a melting point above 2000°C, enabling it to stay solid at operating temperatures. When exposed to high temperatures, $MoSi_2$ will decompose into SiO_2 and Mo-oxides . While the Mo-oxides will vaporize and remain unreacted, the SiO_2 will react with the surrounding YSZ matrix to produce $ZrSiO_4$ (Zircon), a compound with elastic and thermal properties compatible to that of YSZ.

The research undertaken in this thesis project was geared towards discerning the optimal microstructrual morphology to conduce self-healing. This was done through a parametric study which combined the generalized Finite Element Method (FEM) and the Cohesive Zone Model (CZM) to simulate crack behaviour in a randomized domain incorporating multiple TBC microstructural properties, such as splats and pores, in addition to the self-healing particles. The FEM analysis was carried out in the finite element software Abaqus. CZM is a phenomenological model of fracture that allows the modeler to circumvent the inclusion of an asymptotic stress field that would otherwise occur at crack tips, as would be the case if Linear-Elastic Fracture Mechanics (LEFM) were to be applied. CZM laws represents the crack tip region as a plastic zone in which load transfer between the crack surfaces reduces with increasing levels of separation, until a threshold value is reached and the traction between the solid elements is zero. These laws are tied to so-called “cohesive elements”, which are essentially zero-thickness quadrilateral elements enmeshed between triangular continuum elements that constitute the geometry. Though the separation laws are not grounded on elastic theory, it is noteworthy that comparisons have been made between these constitutive relations and empirical observations involving “material bridges” nucleating between crack tip surfaces that enable load transfer between the surfaces. The stiffness assigned to these elements irreversibly decreases when damage is initiated after the stress at the nodes exceed the material strength value. Total damage damaged is resultant when the energy dissipated due to cohesive element separation reaches the fracture toughness value of the material, at which point the stiffness of the element is zero.

The random microstructure generator that was developed for the parametric analyses produces a two-dimensional projection of arbitrary microstructural morphologies. The geometry acquired from this generator consists of a top-coat comprised of a contiguous lamellae structure, pores and healing particles, as well as a homogeneous thermally-grown oxide layer and bond coat. The substrate is excluded from the geometry since its influence is represented via the boundary conditions. The generator allows variation in the average size of splats, the irregularity of splat stacking sequence, the pore and healing particle density and the TC/BC interface shape. After the output geometry has been derived from the generator, it is meshed using GMSH. A Python script is then run to produce the Abaqus input file, in which cohesive elements are embedded between the continuum elements and the boundary conditions are defined. The boundary conditions were chosen to simulate a subset of experiments undertaken at Institut für Werkstoffe und Verfahren der Energietechnik studying TBC fracture behaviour. The samples used in these experiments are disk-shaped specimens exposed to TBC operating temperatures and cooled from the bottom surface. The simulations consisted of a single-step analysis representing a cooling down cycle. A cooling-down cycle was chosen because at peak operating temperatures, the TBC system is at a state of zero residual stress, since the high temperature is comparable to the processing temperatures used during deposition. Two temperature fields are therefore assigned, for the initial and final step. For the initial step, the nodes constituting the mesh are assigned a temperature value directly proportional to their spatial y-coordinate, such that nodes at the top surface have an initial temperature value of 1200°C and the nodes at the substrate/BC have a value of $800°C$. The final step consists of a homogeneous temperature field in which all the nodes ultimately attain room temperature value of $30°C$. Because the continuum elements in the model are attributed coefficients of thermal expansion, the model is allowed to respond thermo-mechanically. The lateral sides of the geometry are constrained so that the TBC system conforms to the substrate contraction, since the former is usually an order-of-magnitude smaller in dimension than the latter. This induces a predominantly mode II damage at and above the TC/TGO interface.

Following a set of preliminary studies examining the sensitivity of the boundary conditions, two sets of parametric studies were executed. Parametric study A examined the effect of varying lamellae properties in the conventional TBC model. Parametric study B was designed to provide insight on the interaction between the lamellae, healing particles and pores. After the section outlining background information on fracture modelling using CZM and on TBC systems is presented, the results for Sets O,A and B are presented in chapters 4, 5, and 6, respectively. The insights from each study are then assembled to produce a list of directions for changing TBC microstructure in order to control fracture properties.

Chapter 2

Theoretical Background

The development of a microstructural optimization tool necessitates the consideration of two separate fields of inquiry. Since the tool derives its output from accumulated results of FEM simulations, it is of primary importance to examine the mechanical relations that will principally inform model behaviour. The first part of this section, therefore, outlines the theoretical principles of LEFM and CZM as well as its practical incorporation into general FEM. In order to produce an accurate geometrical representation, it is also important to empirically examine the categorical features that qualitatively characterize the TBC microstructure that consequentially engenders its mechanical properties. In addition to this, the microstructural evolution throughout operative use must be considered. It follows that the second part of this section compiles information on TBC properties and known failure modes. An in-depth delineation of the self-healing TBC concept is then presented. A foundational basis for the optimization tool is presented in the form of a discussion synthesizing these three elements.

2-1 Modeling Fracture

2-1-1 Cohesive Zone Model

The asymptotic nature of the LEFM equations governing the stress field in the proximity of a crack bar straight-forward implementation into a finite element model (FEM). To overcome this obstacle, several strategies have been developed and a portion of these have been implemented in the finite element software Abaqus. The two main methods is the cohesive zone model (CZM) and the Extended FEM (XFEM). The XFEM models fracture behaviour through explicit incorporation of LEFM equations. This is done by “enriching” elements that contain a crack or a crack tip with functions that include the stress-intensity functions, in addition to the conventional polynomial functions governing first-order elements. CZM, while borrowing from LEFM by utilizing quantities such as the J-integral, is in essence an alternate model. A main advantage of the former method is that the incorporation of a crack into the geometry is mesh-independent. In CZM, cracks can be defined or formed along the interfaces of the continuum elements comprising the model. A disadvantage of XFEM is that two cracks cannot penetrate the same element. In this thesis project, CZM was chosen as the fracture response being tested is crack propagation. To date, a straight-forward implementation of XFEM for crack-growth behaviour has not be developed for ABAQUS. This makes CZM the more efficient option.

CZM allows the modeler to circumvent incorporating a stress singularity into the FE model. Rather than assuming an asymptotic stress field at the crack tip, a CZM approach reproduces crack surface behavior by involving traction-separation laws that attenuates the elastic properties around a predefined fracture process zone. In this way, the cohesive zone approach is essentially a phenomenological model and not one rooted from physical laws, like the stress intensity factor in Linear Elastic Fracture Mechanics (LEFM). These laws express the traction t across two crack surfaces after initiation had taken place, as a function of the distance between the two surfaces δ_n. Although several traction-separation relations have been developed to emulate responses arising from different material classes, e.g. linear (Camacho & Oritz), trapezoidal (Tvergaard & Hutchison), polynomial (Needleman), the essential pattern of behavior being described is as follows: the tractions stress decreases from a peak value as displacement between the two crack surfaces increases and eventually drops to zero after a threshold separation value δ_c has been reached. Though the separation law is not grounded on elastic theory, it is noteworthy that comparisons have been made between this constitutive relations and empirical observations involving “material bridges” that allow for load transfer in ceramic and concrete material when a crack initiates. Nevertheless, the approach can be related to LEFM since the area under the traction-separation curve is equated to the strain energy release rate:

$$G_c = \int_0^{\delta_c} \sigma(\delta_n)\mathrm{d}\delta_n$$

A cohesive crack will initiate or grows when the J-integral (which yields the strain energy released about a closed path) exceeds G_c. The J-integral applied about the perimeter of a cohesive crack in an isotropic material under pure Mode I loading produces an output that can be expressed through two components:

$$J = -\int_0^{\rho} \sigma \frac{\partial \delta}{\partial x} dx + \frac{K_{I^2}}{E}$$

The material-specific properties required for the implementation of CZM model are the material ultimate strength σ_c, fracture energy G_c and the critical separation δ_c. While the former two properties are easily available, there is limited experimental observation associated with the latter property. CZM implementation in a FEM model involves special elements called cohesive elements. Abaqus offers a number of options from this element family i.e. finite or zero thickness, number of nodes, 2D or 3D. These cohesive elements will separate when the threshold displacement level had been reached, reproducing the phenomena of crack growth. This is why crack propagation can only occur along cohesive elements and must be implemented along the crack path when it is known a priori. When the purpose of the FEM model is to discern the crack path in a given problem, cohesive elements must border all the ordinary structural elements that constitute the model. Naturally, the discretization of the domain must be fine enough such that a propagation direction can be as independent from mesh size as possible. It is also important that the elements employed have lengths less than the characteristic length of the material, which is a measure of the size of the fracture process zone surrounding the crack tip zone, in which LEFM theory applies

$$l_c = \frac{G_c E}{\sigma_{c^2}}$$

Where G_c, E and σ_c are the fracture toughness, Young's modulus, and strength of the material in question. The characteristic length is essentially an inverse measure of the brittleness of these material. Thus, a smaller characteristic length indicates a smaller fracture process zone, and therefore a more brittle material.

Modeling cohesive fracture in Abaqus CAE involves two classes of inputs: damage initiation and damage evolution. The damage initiation criteria involves choosing the damage initiation law and the strengths of the material in the three planar direction. Damage evolution is specified by the fracture toughnesses and the traction-separation curve shape. The properties specified are then attributed to the cohesive elements that constitute the model. In addition to this, the cohesive elements can also be assigned a viscosity value to encourage solution convergence.

For cohesive fracture, damage initiation laws can be defined in terms of critical stresses and critical strains. The damage initiation criteria characterized by maximum stress (MAXS), for instance, induces separation between cohesive elements when any one of the ratios between the principal stresses and it correspond strength exceeds 1. QUADS, on the other hand, uses a quadratic combination of the three ratios to determine the state in which the material will yield. Analogous criteria exist for critical strain, namely QUADE and MAXE. These damage initiation conditions resemble crack-path heuristics such as the maximum principal stress criteria used in LEFM studies.

Damage evolution, on the other hand, is governed by the fracture energy (assuming an isotropic material) and the critical displacement specified. Throughout the analysis, traction t_n ascribed to a cohesive element is quantified with the use of a damage parameter D. This parameter has a value of zero prior to damage initiation, and increases to unity until the critical displacement separation has been reached:

$$t_n = \begin{cases} (1-D)\bar{t}_n & t_n \geq 0 \\ \bar{t}_n & \text{no damage} \end{cases}$$

In this project, a linear-damage evolution law was used. This damage evolution law can be defined used the critical displacement δ_m^t, the maximum separation value of the cohesive element attained (not instantaneous, as the cohesive element may close due to compressive loads, but will still exhibit weakened behaviour) and the initial displacement δ_m^0 have been defined:

$$D = \frac{\delta_m^t(\delta_m^{max} - \delta_m^0)}{\delta_m^{max}(\delta_m^t - \delta_m^0)}$$

2-1-2 Qualitative Fracture Behaviour

TBCs, as a type of ceramic, shows brittle fracture, meaning fracture damage is preceded by low amounts of plastic behaviour, in contrast to ductile materials. They are typically able to uphold much higher compressive loads as opposed to tensile loads. Pores in the microstructure (which as previously mentioned, are characteristics of plasma-sprayed YSZ coatings) introduce stress concentrations, explaining why most microcracks develop at curvatures parallel to the predominant loading direction.

In the study of the fracture of materials, a distinction is made between extrinsic and intrinsic mechanisms that affect crack propagation. Intrinsic mechanisms refer to the characteristics of the microstructure that would exist without the crack there, such as microcracks and voids. Extrinsic mechanisms, on the other hand, refer to explicitly to the inelastic zones surrounding the crack wake, which locally diminishes crack-tip stress intensity. It had been observed that the former mechanism plays a more dominant role in brittle materials since, as mentioned previously, brittle materials show very little plasticity during fracture.

Microcracking is an example of a crack-tip shielding mechanism very characteristic to ceramic materials, however from an alternative standpoint, its occurrence may contribute to crack growth (Ruhle, Evans, Mcmeeking, Charalambides, & Hutchinson, 1987). Microcracks occur in any region of high stress concentration, and can either release residual stresses and thereby homogenize the stress field, or coalesce with an incoming macrocrack and ultimately feed its crack-growth driving force.

Particulate composites have been subject to extensive experimental observations. Proportionally high amounts of research effort have been allocated to investigate the behavior of silicon carbide reinforced aluminum (SiC-Al). Ceramic-matrix composites are not exceedingly popular due to the fact that their fracture properties are as low, if not lower, than pure ceramic materials. Evaluating the effect of a single inclusion can be approached from a number of perspectives. When considering energy principles, toughness is favored by increased fracture surface area since this increases the amount of energy absorbed that would otherwise be allocated to increase the crack driving force. Inclusions increase the crack surface area by virtue of causing crack deflections by either acting as an obstruction, a repeller, or an attractor. On the other hand, inclusions also may act as stress concentrators that make the local area susceptible to crack nucleations. A weak particulate-matrix interface also has a detrimental effect on the overall toughness of the material.

Generally speaking, most research papers attribute CTE mismatch as the primary cause behind crack deviation in the proximity of an inclusion in case of thermal cycling. If the filler has a higher CTE than the matrix, it will expand more when exposed to a temperature change and as a consequence engender compressive stresses in the matrix. This will toughen the area; recall that the K_I is directly proportional to the applied tensile stress. If compressive stresses arise, the effective tensile stress reduces, thereby also decreasing K_I. Cutler (Cutler & Virkar, 1985) described a relation between the residual stresses and the toughness augmentation experienced by the matrix:

$$K_{IC,2} = K_{IC,1} + 2q\sqrt{\frac{2D}{\pi}}$$

Where $K_{Ic,2}$ and $K_{Ic,1}$ are the fracture toughnesses of the composite and the matrix, respectively;

q is the magnitude of residual stresses;

D is the interparticulate spacing.

A more extensive expression was put forward by Taya (Taya, Hayashi, Kobayashi, & Yoon, 1990), which incorporated the particulate-matrix stiffness ratio, Poisson's ratios of the matrix and particulate volume fractions and the CTE misfit strain. The results from the expression were validated by experiments involving SiC matrix with TiB_2 particulate reinforcement and showed that the expression underestimated the toughness increase.

Such an effect can also arise due to elasticity mismatches, which similarly results in an inhomogeneous stress field that cause cracks to behave in a number of identified ways. Ahlquist (Ahlquist, 1975) used the term "crack-bowing" to refer to the decrease in crack-tip stress intensity within proximity of a hard inclusion in a soft matrix, and an increase when considering a soft inclusion in a hard matrix. In the latter case, cracks propagate from the inclusion towards the matrix. When there are more contractive strains in the inclusions, peripheral stresses arise. When the contractive strains are higher in the inclusion, microcracking occurs, whereby the cracks form on the perimeter of the inclusion. Microcracking in the vicinity of an inclusions has been a topic of interest, as they serves as a toughening mechanism for the surrounding matrix material (Hillig, 1987). Rice (Rice, R. W. and Pohanka, 1979) shows that spontaneous microcracking (which results from internal stresses between microscopic material structures i.e grains or splats, due to disparate strains) occurs only when the secondary phase reaches a threshold size:

$$D_c \approx \frac{\alpha \gamma_B}{E_c(\Delta\epsilon)^2}$$

Where α is a proportionality constant that depends on the shape of the filler (for spherical particulates, $\alpha = 9$);

K_c is the elastic modulus of the composite;

$\Delta\epsilon$ is the strain mismatch;

γ_B is the interfacial fracture energy.

Green (Green, 1981) developed another analytical expression to describe the so called critical grain size which determines whether or not spontaneous microcracking (as opposed to external microcracking) will take place and discovered that this condition is actually a function of the ratio of applied stress to residual stresses that remain post-processing. This means that at applied stress levels that are similar in magnitude to the residual stresses will encourage the formation of microcracks. Another type of plastic behavior is crack bridging. Crack bridging has been a phenomena observed in the fracture behavior of silicon carbide (SiC) whiskers-reinforced ceramics. In this mechanism, the whiskers debond from the matrix when perpendicular to with the trajectory of a crack, and fall onto the crack tip wake and effectively stitch the crack together. A conflicting observation was put forward by Chawla (Chawla, 1998), who asserted that the presence of short fibers effectively diminishes composite toughness because cracks tend to originate at the fiber ends due to thermal mismatches.

Becher (Becher, Hsueh, Angelini, & Tiegs, 1988) also argues that whiskers introduce residual stresses following conventional ceramic processing, since they are not formed from powders which sinter under no added pressure.

2-2 Thermal Barrier Coatings

State-of-the-art TBCs top coats are normally composed of yttria-stabilized zirconia (YSZ), typically with 8 wt% yttria. Pure zirconia is not used without a stabilizing agent due to the unfavorable phase transformation from tetragonal to monoclinic that occurs when the ambient temperature is elevated beyond 950 °C. The addition of stabilizing agents (such as yttria, CaO, MgO or CeO_2) followed by a high cooling rate during processing allows for the retention of the tetragonal crystal structure throughout the operative temperature range. The composition originally used to coat jet turbine blades was yttria stabilized with MgO_2. Though this material was very effective during the initial thermal cycles, it was observed that the thermal diffusivity progressively increased, consequentially deteriorating the TBCs key functionality of minimized heat flow to the substrate. This is because MgO_2 has a tendency to precipitate at high temperatures, so the coating composition would evolve from a homogeneous mixture to a two-phase material. When the oxidizing agent was replaced by $\mathrm{Y_2O_3}$, there was a four-fold increase in lifetime when maximum exposure temperatures exceeded 1100°C. 7-8wt%YSZ has been the most widely used and tested composition since.

The bond coat is normally composed of an intermetallic substance, typically MCrAlY or NiAl. The most important requirement regarding the design of this layer is that it must have good bonding strength (mechanical or chemical) with both the top layer and the substrate.

2-2-1 Processing

Ceramic TBC coats are usually plasma-sprayed (PS) onto the substrate, but a popular alternative is electron-beam physical vapor deposition (EB-PVD). Plasma spraying consists of molting powdered feedstock material through an electrically charged heat source with temperatures in the range of 10,000 K. The molten powder is then deposited on the surface through a jet, where it flattens and solidifies, increasing in thickness at a rate of a few micrometers per second. PS-TBCs possess microstructures that are porous and characterized by the presence of many microcracks. The microstructure is composed of distinct features known as lamellae, which consist of "splats" or flat elliptical depositions of material layered horizontally. Splats have diameters measuring between 10-50 microns and thicknesses between 1-50 microns. A number of process parameters have direct effects on the resulting microstructure and therefore, in essence, on the intended performance of the coating; plasma characteristics(power supply, type of gas used), powder feed (shape of the powder), plasma jet (velocity, temperature) and particle impact (impact angle, degree of molten state of particle) all influence the quality of the coating.

EB-PVD produces a relatively more regular microstructure, identifiable by columnar structures. It yields a coating with a smoother finish along the external surface as well as the BC/TC interface. A smoother interface contributes to stronger chemical bonds between the two layers, which effectively increases the strength of the coating. This leads to a reduction in spallation and subsequently an increase in durability. Furthermore, the regularity of the microstructure allows for a more uniform transference of load in the in-plane direction, which endows the coating with the favorable attribute of compliance. However, this same feature also contributes to more efficient heat transfer, allowing more heat to reach the substrate and thus diminishes its insulating properties. Fabrication using EB-PVD allows the manufacturer more control of the microstructure and thus the mechanical properties of the coating.

Other processing methods include solution precursor plasma spraying, which utilizes liquefied feedstock material rather than powder. This process allows the manufacturer more control over porosity content and produces lamellae shorter in length. Chemical vapor deposition have been used to make very thin films of YSZ, but not thick enough to be applied as a TBC. Metal-organic chemical vapor depositions have been a focus of research in an attempt overcome this restriction.

2-2-2 Properties

The properties of TBCs composed of different materials and produced using different processing routes yields coatings with widely varying microstructures that are cannot be suitably equated to one another. In the interest of conciseness, the following discussion concerning the mechanical properties will be constrained to specifically addressing air-plasma sprayed 7-8 wt% yttria-stabilized zirconia. This is principally because the matrix of the self-healing TBC composite under development is composed of this variant. Also, 7-8wt%YSZ is also the most widely used TBC, and purvey to the most studies.

Process-property relationships have been an area of intensive study, since the morphology has been proven to have a deep impact on the mechanical properties of the TBC, which in turn exerts a multi-faceted effect on the global TBC performance. Increasing the porosity, for instance by increasing the substrate temperature or lowering the ejection velocity (Kulkarni, Vaidya, Goland, Sampath, & Herman, 2003), will reduce the thermal conductivity of the coating, thereby enhancing its insulative function. Pores however also reduce the elastic modulus of the coating, effectively reducing the durability of the coating due to having lower compliance with the substrate. Properties that can be controlled through the manipulation of processing parameters principally include the porosity and lamellae dimensions, but features such as the vertical crack density and bonding ratio have also been considered (Yao et al., 2016).

The bonding ratio α between lamellae refers to the ratio between their total interfacial area and the area that is bonded:

$$\alpha = \frac{A_{bonded}}{A_{interfacial}}$$

The relationship between the bonding ratio and the fracture toughness of the coating is as follows:

$$G_{Ic} = 2c_p\gamma_e\alpha$$

Where γ_e is the bulk toughness, and c_p is a material related constant ≈1.2.

The bonding ratio has been shown to be augmented by increasing the plasma power and increasing the spray distance (C. J. Li, Yang, & Li, 2013):

Another counter-intuitive and oft-cited beneficial characteristic of YSZ microstructure is the presence of many segmentation cracks. Segmentation cracks are cracks that are aligned normal to the substrate, and arise primarily during the quenching phase of processing, when the coating material is subjected to a steep negative temperature gradient after leaving the very hot spray and land at a cool substrate. When compressive stresses arise in the TC t compensate for relatively larger expansion of the substrate due to a CTE mismatch, the vertical cracks can separate, ensuring that excess strain energy is not retained in the system (Taylor, Brandon, & Morrell, 1992). However, a microstructure characterized by porosity and defects makes its physical behaviour intrinsically non-linear and hysteretic (Evans, He, & Hutchinson, 2001). The unfavorable retention of strain is also the main reason why thinner coatings have higher thermal shock resistances. When thicker coatings are used, the elastic strain energy stored in the coating also increases, which accelerates degradation (Tsipas & Golosnoy, 2011).

2-2-3 Failure Mechanisms

The properties of a TBC will gradually deteriorate during its life cycle due to its constant exposure to harsh environments. While the functionality of the coating progressively lessens due to a combination of mechanisms, final failure most typically occurs when the top coat chips away from the bond- a process called spallation. A number of factors contribute to the inhomogeneity of the stress field in this sensitive area, the most eminent being:

- roughness of the interface, which leads to maximum and minimum stresses in the trough and crest region, respectively;
- CTE mismatch between the bond coat/top coat;
- residual stresses post-fabrication;
- thermal stresses from thermal cycling;
- the development of a thermally grown oxide barrier (TGO).

Two modes of failure at the TC/BC interface have been identified: edge delaminations and buckle delaminations (Evans et al., 2001). Generally speaking, both modes appear to occur primarily due to the CTE mismatch between the different components of the system. The substrate, which is metallic, will expand more than the intermetallic bond-coat and ceramic top coat, meaning that the upper two coats will carry strain energy resulting arising from compressive stresses. The second leading cause for delamination is the growth of the TGO layer. YSZ possesses a large amount of oxygen ion vacancies, which, at elevated temperature, combine with metallic ions originating from the bond coat to form a TGO layer between the top coat and the bond coat interface. The TGO affects the local stress field in two ways: (i) stresses arise due to the thermal expansion mismatch with its surrounding layers and (ii) introduction of compressive stresses due its accretion throughout the coating life cycle. The TGO will grow continuously throughout the coating's operative life, but this growth will decrease in rate as the a thicker layer impedes incoming oxygen atoms from reacting with metallic ions originating from the BC. It has been observed that when exposed to monotonical loading, transverse edge cracks nucleate near the TC/BC boundary. These cracks increase in number as stress levels increase, and eventually either break through the interface or branch out into separate trajectories right before propagating into the interface. It must also be mentioned that the growth rates acceleration, as the stress concentration at the track tip increase with increasing length, which means that damage occurs at an increasingly faster rate as the lifecycle continues. The TC/BC interface is even more vulnerable to damage due to the fact that the tensile gradient that occurs due to thermal expansion produces a bending moment that exposes this region to tensile stresses. When the coating is exposed to high temperature, the upper region of the TC will expand more than the lower layer. This effect is accentuated when thicker coatings are used (Gilbert, Dauskardt, & Ritchie, 1997).

As a consequence of thermal cycling, an additional two modes of fracture have been identified: segmentation, which refers to cracks oriented in the direction of coating thickness, and delamination cracking, which refers to cracks oriented normal to the coating thickness. Wessel (Wessel & Steinbech, 2002) noted that segmentation cracks follow the pre-existent inter-splat routes (the boundaries between splats directly after processing) while delamination cracks follow inter-lamellar cracks. While delamination is undesirable due to its expedition of spalling, segmentation may contribute to toughening since it increases the strain tolerance of the coating. Malzbender (Malzbender, Wakui, & Steinbrech, 2004) suggested that the convoluted path followed by segmentation cracks brings about energy-absorbing surface interaction. However, depending on the quality of the coating, weak cohesion of splats could give way to crack branching, which ultimately weakens the material.

Other high temperature time dependent process include sintering, creep and hot corrosion. Sintering and creep increase the thermal conductivity and the elastic modulus of the coating, which consequentially gives rise to cracks caused by shrinkage. This is because sintering reduces the porous nature of the microstructure, making it more dense and therefore making heat flow through its thickness more efficient. Hot corrosion may occur when vapor originating from a marine environment deposits salt into the coating. YSZ-based coatings are especially susceptible to corrosion, as it reacts readily with species such as Na_2O, SO_3 and V_2O_5. YSZ also undergoes significant attenuation when exposed to SiO_2 molecules even at very low concentrations. (Ma & Dong, 2011) Impact damage is also a source of failure, as it causes defects that continue to grow with every load cycle. These failure mechanisms are markedly different from the preceding two modes due to the fact that damage originates at the surface of the top coat, rather than at the BC/TC interface.

The gradual deterioration of a TBC system is governed by a number of factors - the top coat microstructure, the choice of bond coat and the application. While the former two have been elaborated on, the latter has not been explicitly treated. The application of the TBC, whether it be for jet turbine blades or power generation equipment, determines the kind of load case the coating would be subjected to. In the case of jet turbine blades, the coating will be subjected to cyclic thermal loads (thermal cycles) and could be subject to micro-impact loading. In power generation equipment on the other hand, the coating will primarily be subjected to monotonic thermal loading for extended periods of time with few oscillations.

In summary, failure upon thermal cycling is mostly driven by the CTE mismatch between the different layers of the system. TGO growth has been the attributed cause for nucleating interfacial cracks that continue to grow with every thermal cycle, with unfavorable stress concentrations at the crests of the uneven TC/TGO interface. Sintering of the ceramic top coat increases the Young's modulus and its thermal conductivity. An increase in thermal conductivity implies that more heat will be allowed to surpass the TC as the life-cycle progresses, which may cause damage to the interior layers, i.e creep. The other routes for failure, such as impact-damage, pre-existing flaws and hot corrosion cannot accurately be modeled, but nevertheless contribute to the deterioration of the coating. Needless to say, the behavior of the TBC system over its lifetime until failure is complex. The behavior of the coating is not simply determined by material constants, but equally so from the microstructure, which is a function of a multitude of variable processing parameters. Furthermore, each individual failure mechanism effects and is effected by the other mechanisms, giving rise to per mutative behavior. Simplifying assumptions, like ignoring hard to predict parameters such as impact and corrosion or modelling the porous TC as a continuum, detracts from the model accuracy.

2-2-4 TBC FEM Models

Many FEM models of TBC systems are used to measure field responses to cyclic thermal loads, which usually entails a ramp-up from room temperature to operating temperatures in order of 1000°C, which causes mismatch stresses arising from the interfaces of the separate layers in the TBC system. Another reoccurring feature in these investigations is the incorporation of sinusoidal interfaces, with an approximate thickness of 1 micron, meant to represent the TGO layer. Baker(Bäker, 2014) performed a cyclic thermal analysis, while varying the shape of the TC/TGO interface and crack initiation sites. He found that along the TC/TGO interface, crests provide more crack driving force that valleys as the former is prone to accumulate tensile stresses while the latter accumulates compressive stresses. He also pointed out that this effect only becomes evident after a minimal TGO thickness has been surpassed. His findings were corroborated by Ranjbar-Far (Ranjbar-Far, Absi, & Mariaux, 2012). Al-Athel (Al-Athel, Loeffel, Liu, & Anand, 2013) remarked that larger interface amplitudes encourage more crack growth. Comparable numerical investigations were performed by Bednarz (Bednarz, 2006) and Nair (Nair, Singh, & Grimsditch, 2004). Modelling gradual TGO growth in a constrained environment can be an arduous endeavor when choosing to implement extensive mechanical-chemical theory to accurately reproduce the phenomenon.

Hille (Hille, 2009), in a study that consolidates microcrack growth the accretion of the TGO layer, incorporated the diffusivity parameters for the TC, TGO and the BC for oxygen, a reaction rate parameter, oxygen molarity, a calibration parameter, an estimate of the oxygen concentration at the TBC top-coat surface and the oxygen flux at the substrate-BC interface, to complete his model of TGO growth. Pindera (Pindera & Arnold, 2003) employed the Higher-Order Theory of Functionally Graded Materials" to study the fatigue characteristics of a two-phase TBC comprising of 8-YSZ and aluminum particulates (which were earlier shown to increase the coating durability) in response to the growing TGO layer, and found that in such a problem, crack propagation is primarily governed by complex mixed-mode loading.

2-3 Self-Healing Materials

The philosophy of designing self-healing materials is markedly different from that of conventional materials when the primary objective is to attain optimal durability. While in conventional material design this is accomplished by fine-tuning the microstructure of a given substance to attain maximal damage resistance, the design of a self-healing system entails equipping the material with the life-mimicking capability of recovering structural integrity from the unpreventable wear and tear that follows use. Though current interest in this divergent line of thought was catalyzed by White et. al in their seminal paper (White et al., 2001) delineating the working mechanism of a self-healing polymer, the existence of self-healing materials precedes this. Limestone, when calcined prior to use, decomposes into lime when the carbon-dioxide components are removed. When lime reacts with moisture and subsequently carbon dioxide, it will be transformed into limestone again. This is an example of an extrinsic self-healing system, meaning that the damage recovery process requires external simulation, whether it be mechanical, chemical or electric, to initiate. The self-healing TBC of interest in this report incorporates such as a strategy.

Self-healing systems are developed with the characteristics of the constituting material in mind. Polymers, for instance, are able to heal via mechanisms (i.e cross-linking, Diehl-Adler reactions) not reproducible in other kinds of materials. As such, a significant portion of the research effort directed towards developing self-healing ceramics has utilized favorable oxidation reactions that may occur when metallic or intermetallic particulates are embedded into the bulk material. Notably surface crack healing has been shown to occur in SiC particle reinforced ceramics. If a crack propagates into the surface of a material, oxidation of silicon ions originating from the particles occurs and fills the crack. Niihara (Ohji, 1998) demonstrated this with alumina containing 5 vol% SiC particles less than a micron in diameter, but the healed part was significantly weaker than in its initial condition prior to damage. Ando et al. (Ando et al., 1999) observed comparable phenomena in mullite, with approximately 10% higher particulate volume fraction. However, in this case, the healing would hypothetically be able to take place autonomously when considering service conditions of certain applications as well as produce a healed region that maintains or exceeds the initial strength. While experimental results for monotonic loading after healing are positive, lifetime predictions of these composites cannot in practice be validated empirically considering the long service time of most applications and so analysis at the time being is limited to computational models. This has however also posed a challenge, as the behavior of the system is determined by a variety of mechanical and chemical processes, and would therefore require complex constitutive relations. Genet (Genet et al., 2012) developed a macrophysics macroscopic model specific to self-healing ceramic matrix composites from a structural point of view. Cluzel's (Cluzel, Baranger, Ladevèze, & Mouret, 2009) model of the same system was produced from a chemical point of view, and was based on mapping the diffusion of oxygen.

The self-healing TBC system under development also relies on oxidation of the filler material. The requirements constraining the selection of a filler material for a self-healing TBC system are three-fold:

1. the healing agents must remain solid at operating temperature range (15- 1200$°C$) This is because liquids tend to have an unacceptably large CTE, which would introduce unwanted thermal strain to the system. Liquids also have higher thermal conductivities,

necessitating the application of a thicker coating, increasing the weight of the component and thus incurring higher costs.

2. agents must form into a liquid when penetrated by a crack
3. liquid/viscous medium flown into the crack must transform at the healing temperature into a solid by chemically reacting with the matrix material.

$MoSi_2$, which along with YSZ is categorized as a refractory ceramic, meets all the above criteria as it has a high melting point above $2000°C$ (therefore remaining solid throughout operation) but a tendency to flow when alloyed with boron. The healing mechanism is as follows: $MoSi_2$ decomposes at higher temperatures to Mo oxides and Si_2. These oxidation reactions are as follows:

$$2\mathrm{MoSi_2} + 7\mathrm{O_2} \rightarrow 2\mathrm{MoO_3} + 7\mathrm{SiO_2}$$

$$5\mathrm{MoSi_2} + 7\mathrm{O_2} \rightarrow \mathrm{Mo_5Si_3} + 7\mathrm{SiO_2}$$

While the Mo-oxides will ideally vaporize and remain unreacted, SiO_2 will react with and bond to the surrounding YSZ matrix to produce $ZrSiO_4$ (Zircon)— a compound similar in thermal and mechanical properties to YSZ that will partially restore the coating's performance. Experiments that involved a notched free-standing TBC created from an even mixture containing YSZ powder and 8 micron-diameter $MoSi_2$ had suggested that this mechanism can bring about successful self-healing — the notch (crack) had been mostly filled by Zircon.

Research efforts intended to further the development of the self-healing TBC composite have included a proof-of-concept experiment that demonstrated the formation of amorphous SiO_2 and its subsequent reaction with the surrounding zirconia to form the crack-filler material $ZrSiO_4$. The results also revealed the necessity of an external covering for the healing particles in order to prevent premature oxidation occurring prior to any fracture. In response to this realization, particles encapsulated in alumina (Carabat, Zwaag, & Sloof, 2015) were developed and tested. The ensuing observations showed that the alumina exhibited changes in microstructure and properties when exposed to different heat treatments. While the alumina retained its composition at temperatures in the range of 800-850°C, it was observed that the alumina changed into mullite when exposed to temperatures above 1000°C, which weakened the external coating by introducing cracks. Instituting an annealing period allowed for the filling of these cracks by mullite, demonstrating that several processing routes are feasible. Material characterization was also performed (Ruiz, 2016), firstly through point-indentation tests measuring the mechanical properties of YSZ and $MoSi_4$ seperatley, and secondly through the design of a modified Wedge-Loaded Cantilever Beam and Brazilian Disk Test in order to induce controlled crack growth in a self-healing YSZ composite for fracture toughness quantification. The variation in thermal conductance with healing-particle concentration was also tested in a separate study(Kulczyk-Malecka et al., 2016), yielding results that indicate that the thermal conductance increases non-linearly with increasing healing-particle concentration.

Ponnusami (Ponnusami, Turteltaub, & van der Zwaag, 2015) conducted a parametric study studying the effect of an inclusion in a monolithic matrix on fracture behaviour using

CZM. Parameters that were varied included the property mismatch between the two constituent phases (i.e the strength, toughness and Young's modulus) and the interface strength. Nielsen(Nielsen, Legarth, & Niordson, 2011) conducted a comparable, yet less extensive, study using XFEM. It is interesting to note that their results corroborate one another, showing that particles with stiffnesses lower than the matrix will tend to attract an incoming crack and a harder particle will repel it.

Chapter 3

Simulation Set-up

The study conducted on the morphology of the self-healing TBC system consisted of two parts. First, the effect of splat properties on the thermomechanical response of a particle-free system during cooling down phase was investigated. TBC microstructures form incrementally as each TBC particle impacts the substrate surface after it is ejected from the plasma spray at high temperatures (>1000°C), forming a thin pancake-like structure known as a splate or lamella (see Figure 3-1a). Splats stack on top of one another to form a brick structure morphology (see Figure 5-11b). Past research efforts (Wang, Kulkarni, Deshpande, Nakamura, & Herman, 2003) (C. Li & Ohmori, 2002) (Tan, Longtin, Sampath, & Wang, 2009) have used a brick-like schematic to study in particular the effect of the bonding ratio on the top-coat toughness. However, no numerical analyses have been carried out using a concatenated domain. The second study focused on the effect of healing particles in addition to pores.

The parametric analysis was carried out using the finite element software Abaqus/Standard. A virtual randomized microstructure generator was developed to provide model geometry input for the each individual simulation that comprised the study. This generator produces a geometric representation of the TBC cross-section containing individuated features such as lamellae, pores and healing particles. The geometries consisted of a heterogeneous TC layer, comprised of pores, lamellae and healing particles, and a homogeneous TGO and BC layer. The "roughness" characteristic of the TC/BC interface which often gives rise to a non-flat TGO is expressed as a sinusoidal curve, with the stacks of lamellae above this layer conforming to the sinusoid by an adjustable degree.

The lamellae that are found in real TBC coatings are essentially flattened particles, typically circular or elliptical in shape with a high radius-to-thickness ratio. Because they are tightly stacked one atop another, the geometry tool creates the lamellae as an irregular grid of thin rectangular blocks of varying lengths as a representation of the cross section of the lamellae. Pores and healing particles, depicted by circular and elliptical geometry, were randomly distributed throughout the TC domain. The parameters that can be varied in the geometry generator are listed below:

- TBC domain Dimensions (TC/TGO/BC)

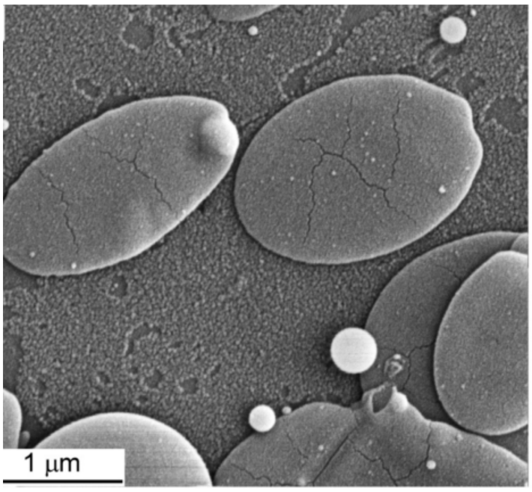

Figure 3-1a: Individual Lamella (Joulia et al., 2014)

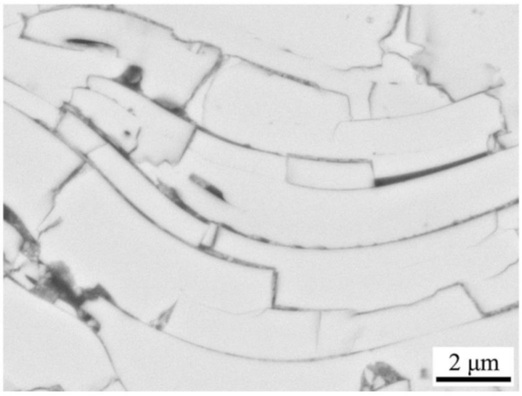

Figure 3-1b: Lamellae Structure (Yao et al., 2016)

- Average lamellae length
- lamellae stacking irregularity
- sinusoidal interface amplitude
- number of peaks and troughs on interface
- damping factor of lamellae distribution above the interface
- size and volume fraction of healing particles
- size and volume fraction of macro-pores/ micro-pores.

3-1 Randomized Microstructure Generator

The TBC Microstructure generator consists of two programs. The first program, which is an executable on MATLAB, produces a .geo file that can be uploaded into the free-ware GMSH for meshing. The .geo file contains the coordinates of all the spatial points that define the geometry, which are then categorized into separate groups to define two-dimensional lines and circular or elliptical arcs, which are in turn used to define surfaces. GMSH reads this file and returns the mesh information in Abaqus input file format. The second program incorporates cohesive elements into the mesh, in addition to specifying all the other attributes (such as the boundary conditions) necessary to complete the model to generate a new ABAQUS file primed for analysis.

The randomization of the geometry is effectuated through the MATLAB random number generator, which produces sequences of pseudo-random numbers. This means that the every time the program is restarted, the same sequence of the seemingly random numbers of repeated. However, the microstructure generator shows chaotic behaviour, since the resulting morphology is as effected by dimensional factors (such as the number of lamellae) as it is by the random number function input.

The geometry generator creates the TC morphology by first creating a regular lattice of points derived from the user-specified average number of lamellaes in both the vertical an horizontal direction. This lattice is adjusted so that the lower horizontal rows of points take on a sinusoidal shape to represent the asperity characteristic of the TC/BC interface. The user can adjust the degree at which the amplitude of the curve damps with every successive row closer to the top-coat surface. The horizontal rows are split into rectangular sections by the incorporation of vertical lamellae interface members connecting two neighboring lamellae rows , with the length of each lamellae taken from a randomized distribution of values characterized by a user-defined irregularity coefficient.

The implementation of inclusions (pores and healing particles) is governed by two parameters: the radius distribution of the inclusion (as well as aspect ratio, if an elliptical geometry is specified) and the area fraction of the inclusion with respect to the area of the TC. A function is executed to successively attribute a randomized location for each particle sequentially, avoiding geometrical overlaps, until the area-fraction limit has been reached. When a model includes pores and healing particles, the inclusion distribution is first transposed over the secondary lamellae lattice, so that circular and elliptical arcs that composed their final description, can be created using coincident points between the two geometries. The vertical members are then implemented and adjusted further to prevent geometrical overlap with the inclusions.

In addition to information regarding the points, lines and surfaces that comprise the final microstructure geometry, the .geo file also contains field variables that determine the element lengths. As explained in Section 2-1-1, this is a non-trivial characteristic of CZM models, as fracture behaviour can only be reproduced if the element lengths are below the characteristic length values. After the MATLAB program has finished writing the .geo file, it is uploaded into GMSH, which returns the mesh data in the form of an Abaqus .inp file. The Abaqus input file derived from GMSH is affixed with element sets (specifying TC elements, BC elements, etc) and node sets required for building the model.

An Abaqus CAE script is then executed in order to produce the final input file, and performs two main functions:

1. implementing cohesive elements between all the continuum elements: The mesh is reconstructed with each continuum element defined by a set of unique nodes. The cohesive elements are then defined by grouping the two pairs of nodes in each internal element edge in a counter-clockwise direction.
2. specifying the rest of the model, Additional model specifications, such as boundary conditions, predefined fields and material property assignments are carried out.

3-2 Model Specifications

3-2-1 Elements

The meshing consisted of linear plane strain triangular continuum elements. Rectangular zero thickness elements were embedded between the continuum elements, such that each

TBC Region	Bulk Element Properties			Cohesive Element Properties		
	E [MPa]	ν [-]	α [-]	σ [MPa]	G [MPa mm$^{-\frac{1}{2}}$]	l_c[μm]
TC Lamellae	200e3	0.15	11e-6	400	0.16	100
TGO	380e3	0.25	7.2e-6	380	0.042	110
BC	200e3	0.30	14e-6	500	0.30	240
Particle	450e3	0.16	8.0e-6	280	0.16	918
TC Lamellae Interface	-	-	-	Variable	Variable	-
TC/TGO Interface	-	-	-	600	0.20	-
TGO/BC Interface	-	-	-	390	0.27	-

Table 3-1: Material Properties (cohesive stiffness 10e10 for all).

continuum element was defined by a unique set of nodes. This scheme is illustrated in the schematic shown in Figure 3-2.

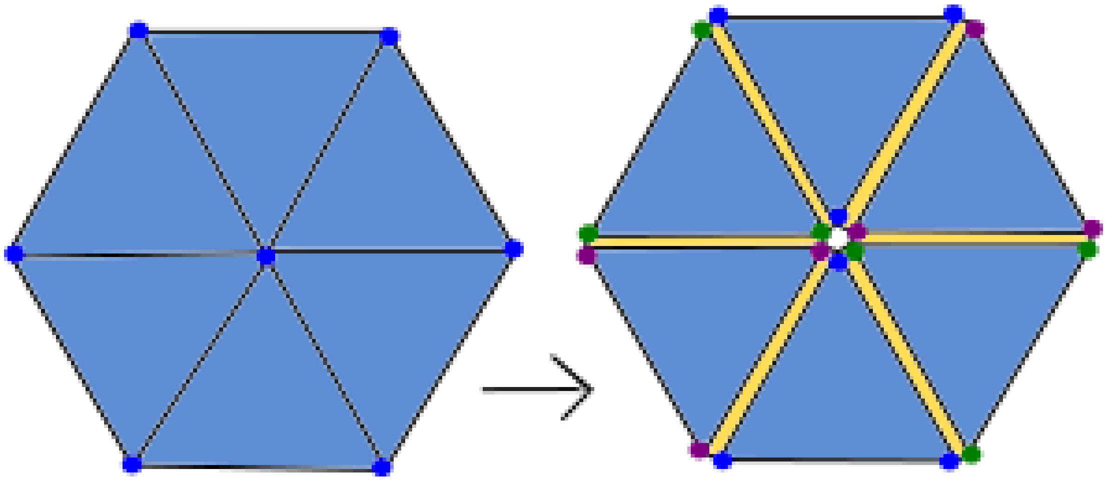

Figure 3-2: Cohesive Element Implementation

The maximum element lengths were set to be less than the lowest fracture process zone length. As mentioned in Section 2-1-1, the fracture process zone length (fpzl) is a measure of a material's brittleness and is a function of its strength and toughness. Crack behavior corroborated by LEFM theory can be simulated as long as the crack length is less than this parameter. Because the models contain three or four different materials, the element lengths were determined by the lowest of these values.

3-2-2 Properties

The material properties assigned to all continuum and all non-interfacial cohesive elements were taken from empirical observations. A complete summary of the section properties is outlined in Table 3-1.The continuum elements are assigned the Young's moduli E and coefficient of thermal expansions α in order simulate a thermo-mechanical response. The cohesive elements, whose constitutive behaviour is explained in detail in SECTION, are attributed strength and fracture toughness in order to indicate the stress value required for crack initiation to occur and for the cohesive element to experience complete damage, respectively. Strength and toughness values designated to bi-layer interface cohesive elements were computed by taking the average of the values assigned to the two materials creating the interface, since empirical observations of these regions are not readily available. In Abaqus, a finite elasticity must be assigned to the cohesive elements. Although in theory, the elasticity of the cohesive elements should be infinite, a very high value of 10e10 MPa was assigned to the cohesive elements in the model. Lamellae interface values were varied in the parametric study and so do not remain fixed for all simulations. However, most simulations use a reference value that is 80% of the bulk lamellae properties. The cohesive properties of the lamellae and the lamellae interfaces are what distinguish the lamellae from one another, since matching values would result in a homogeneous top-coat. The materials themselves were assumed to behave isotropically.

3-3 Boundary Conditions

The load case and boundary conditions were selected to simulate the testing conditions of TBC measurements carried out at Institut fr Werkstoffe und Verfahren der Energietechnik. Research efforts focusing on air-plasma sprayed YSZ samples in particular have typically involved a TBC system deposited onto a disk-shaped nickel-based specimen. The FEM geometry derived from the microstructure generator contains the morphological features present in a hypothetical cross-section of this disk geometry. The load case specified for the analysis is derived from the experimental set-ups that were designed to measure a thermomechanical-response from the TBC specimen. In such studies, a “free-standing” sample is exposed to a heat-source, with factors such as heating rate and dwell time varying from experiment to experiment. While the methodology of these measurements are similar, these slight differences necessitate variation in the predefined conditions enforced onto the model. This section contains discussion on the results derived from three different sets of analyses using different initial conditions, pertaining to a particular variation in the basic experimental set-up.

3-3-1 Reference Model

The Basic Model, designated as such due to its widespread use, refers to a set-up consisting of a flat-disk shaped specimen placed free-standing into an oven without any external coverings or substrate cooling system in place. In such a scenario, it can be assumed that the initial temperature of the entire specimen is uniform throughout. The principal load imposed on the model is a negative thermal gradient, starting from an initially high temperature and terminating at room temperature at the end of the analysis step. The continuum elements are assigned a positive thermal expansion coefficient, and will therefore contract during the analysis. A cooling down cycle is used because the TBC system is assumed to contain zero residual stresses at operating temperatures (>1000°C). This is because the powder TBC particles are ejected from a plasma spray during processing at high temperatures and will contract after impact. This contraction induces residual stresses which dissipate when expanded to its initially-formed dimensions. (Guo, Vaßen, & Sto, 2005) (Ahrens, Lampenscherf, Vaßen, & Stöver, 2004) (Czech, Mallener, Stamm, & Stover, 2001) (Karger, Vaßen, & Stöver, 2011)

The substrate is not explicitly modeled into the domain, but it is assumed to have a dominant influence on the thermo-mechanical response of the system, as the thickness of the substrate is typically an order of magnitude larger than that of the coating. To enforce this condition, two boundary conditions are included. The first set is applied to nodes lying on the base of the BC, where the substrate would otherwise begin. The elements are constrained from displacing along the vertical direction, ensuring BC/substrate spallation does not occur. They are also subject to the substrate thermal strain:

$$\epsilon_{sub,th} = \alpha_{sub} B \Delta T (1 + \nu_{sub})$$

$$U_{1,bn} = \epsilon_{sub,th} (\frac{x}{B})$$

The second set is applied on the nodes comprising the two lateral sides of the domain. To enforce this condition, the mesh must be constructed such that the nodes lying on the left and right perimeter are aligned with one another. The relative horizontal displacement of the two nodes are then constrained to cumulatively equate to the thermal strain experienced by the substrate:

$$U_{1,r} + U_{1,l} = \epsilon_{sub,th}$$

3-3-2 Non-Uniform Initial Temperature Distribution

Some experimental set-ups (Guo, Vaßen, & Stöver, 2004) have involved fixing the substrate to a cooling system, so as to ensure an even temperature gradient through the thickness of the specimen. Because the presence of TBC systems in actual structures induces such a temperature gradient during operating conditions, this set-up may be more appropriate for making extended comparisons to more realistic TBC durability studies and for estimating lifetime. In order to simulate this modified set-up, the temperature magnitude assigned to each node at the initial step of the analysis was a function of its spatial y-coordinate, producing a non-uniform initial temperature field:

$$T_{N_i} = (1 - \frac{y_{N_i}}{H} \frac{T_{surf}}{T_{sub}}) T_{sub}$$

Where T_{N_i} is the temperature specified for node N_i, y_{N_i} is its spacial y-coordinate, H is the height of the domain, and T_{surf} and T_{sub} are the initial temperatures of the surface and substrate respectively.

3-3-3 Curved Specimen

Disk-shaped specimens with a slight curvature were used by researchers to allay the effect of stress concentrations that occur at the free edges of the crack. This condition is introduced into the basic model by modifying the side-node constraint equations by including another spatially varying coefficient that reduces the effect of the substrate contraction:

$$k = 1 - \frac{y_{N_i}}{H}\delta$$

$$U_{1,r} + U_{1,l} = k\epsilon_{sub,th}$$

3-3-4 Axisymmetric Model

A model composed of axissymmetric elements was also created with the left edge of the domain acting as the rotational axis of symmetry. The left edge nodes are constrained from any displacement, so only the right edge nodes are allowed to contract inward.

$$U_{1,r} = k\epsilon_{sub,th}$$

$$U_{1,l} = 0$$

The key benefit of this model is that the effect of z-stress can be incorporated into the analysis. However, the irregularity of the TGO asperity has to be forfeited, which can be seen by comparing Figures 3-3a and 3-3b.

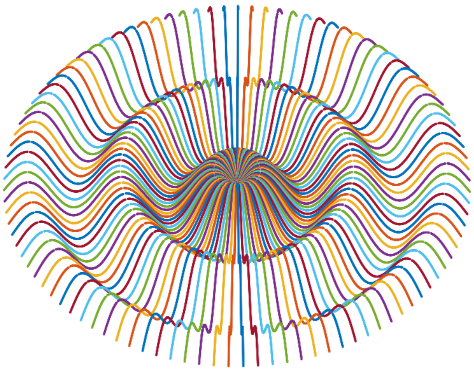

Figure 3-3a: TGO morphology representation in an Axisymmetric Model

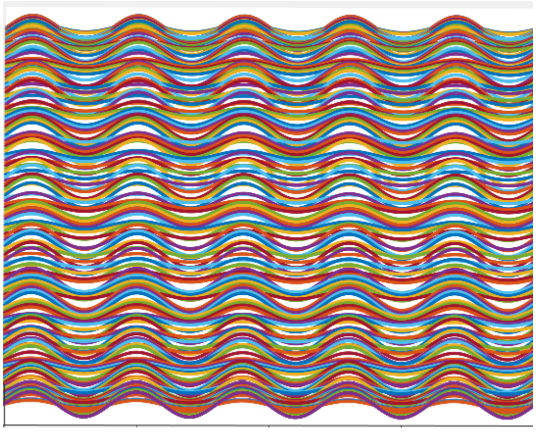

Figure 3-3b: Actual TGO morphology

3-3-5 Weakened TC/TGO interface

Within the context of practical use, the TC/TGO is widely accepted to be a weakened area within the TBC system. This is due to two reasons:

1. There are higher concentrations of post-processing residual stresses in this region, as during deposition, the temperature gradient between the TC particles and the bond coat will be higher than between the TC-particles themselves as the coating gains in thickness.

2. the TGO, which develops due to the oxidation of the bond-coat, accretes into the TC layer, introducing high local compressive stresses

The latter phenomena has been incorporated into numerical analyses through a number of methods, including re-meshing or utilizing special swelling elements. Due to the added computational costs of these features, the TGO growth stresses are not explicitly included in the analysis. The model was instead built with weakened cohesive elements branching from the TGO into the TC, chosen at random locations along the TC/TGO interface. The weakened elements were attributed a strength value of 10 MPa and a toughness value of 0.03.

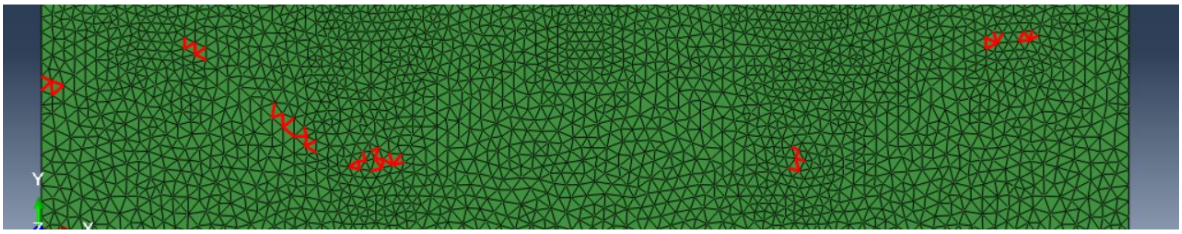

Figure 3-4: Weakened TGO interface elements

3-3-6 Mode II fracture suppression

Upon analysis of the cracks that run diagonally from the free surface to the lateral edges, it is clear that the cracks are primarily dominated by mode II loading, which causes the cohesive element faces to slide along one another rather than separate, resulting in Mode II fracture or shear tearing. By using increased values for the mode II strength and toughness of the TC cohesive elements, Mode II fracture can artificially be suppressed. This can be partly justified by the fact that the crack propagation laws in LEFM are not extensively verified or validated for mixed-mode cases. Studies on the mixed mode behaviour of TBCs yield ambiguous results. Furthermore, studies using two-parameter fracture behaviour dictate that another factor known as the T-stress becomes relevant when considering mixed-mode loading. Both these cases are elaborated further:

Measurements of mode II fracture behaviour in TBCs have been limited in number, but do seem to reveal variability. Choi (Choi, Zhu, & Miller, 2005) showed that APS TBCs exhibit a mode I to mode II fracture toughness ratio larger than in the initial stages of crack propagation, but this ratio decreases as the crack length increases. A similar trend was note by Arai (Arai, Okajima, & Kishimoto, 2007) for fracture along the TC/BC interface. Both quantities were shown to vary significantly with the exposure temperature. Jian (Jian, 2016), in documenting the relationship between porosity and fracture energies, remarked that as cracks propagated within a TBC, they tended to become more Mode II dominated.

While the heuristic criteria implemented in the cohesive zone model have derived from ramifications of the one-parameter damping theory of fracture, many attempts at understanding fracture in complicated loading conditions have involved a two-parameter approach. A two-parameter fracture criterion was first put forward by Williams (Williams & Ewing, 1972) in which th 2D crack tip field is described as an symmetric (pure Mode I) and asymmetric component, represented by an infinite series. While the stress intensity factor comprised the first parameter, the second parameter introduced is called the T-stress. The T-stress is a constant stress value acting parallel to the plane containing the crack tip, and is a component of the symmetric stress near-crack stress field equations. The T-stress describes the constraining effect incurred upon the crack due to loading and geometry. It is readily agreed upon that the T-stress value describing a crack has a discernible effect on its stability, the size of its plastic zone and its fracture toughness (Omar, 2016) (Aliha & Saghafi, 2013) (Smith, Ayatollahi, Pavier, & A, 2006) concluded, in his experimental and numerical analysis studying the brittle polymer PMMA, that the relationship between T-stress and mode II fracture toughnesses is markedly positive and linear.

It is also important to consider that 3D effects are not taken into consideration. Material coincident to faces of the idealized model will foreseeably exert some effect as a buffer, which is not taken into account in the 2D planar representation.

3-4 Parametric Study

The entire study consisted of three sub-studies. The first study, Parametric Study O, is a preliminary investigation on the model's sensitivity to non-geometry related initial parameters. This includes testing the different boundary conditions outlined in the previous section, as well as the model's sensitivity to overload cycles and finally a mesh convergence study. Parametric Study A focused on the response of a conventional TBC system without healing particles. The models in this set were comprised of geometry that integrated pores and lamellae in the TC. Parametric Study B studied the response of TBC systems with healing particles. The list of variables studied in studies A and B are listed below:

- A_p: cumulative area percentage of pores [%]
- l_l: average length of lamellae [μm]
- t_l: lamellae thickness [μm]
- σ_{li}: lamellae interface strength [MPa]
- G_{li}: lamellae interface toughness [MPa$\sqrt{\text{mm}}$]
- A_{sh}: cumulative area of self-healing particles [%]
- r_{sh}: radius of self-healing particles [μm]
- σ_{sh}: self-healing particle strength [MPa]
- G_{sh}: self-healing particle toughness [MPa$\sqrt{\text{mm}}$]

Set ID	$T_{sub.initial}$	$T_{surf,initial}$	T_{final}
O2.1/O3.1	800	1200	30
O2.2/O3.2	850	1200	30
O2.3/O3.3	900	1200	30
O2.4/O3.4	800	1250	30
O2.5/O3.5	800	1300	30

Table 3-2: O2 and **O3** Parameters

- $\sigma_{sh,i}$:self-healing particle interface strength [MPa]
- $G_{sh,i}$: self-healing particle interface toughness [MPa$\sqrt{\text{mm}}$]

Both the lamellae-only set and the lamellae-pore-particle system set of parametric analyses used fixed domain dimensions, with a width of 500 microns, and the TC, TGO, BC height of 500, 8, and 700 microns respectively. This information is summarized in Table 3-4. The original asperity on the post-processed TC/BC interface that results in a non-smooth TGO layer was modeled using a sinusoidal curve with a phase of 5π (3 peaks). The rate at which the lamellae conform to a straight horizontal interface through the thickness of the TC was set at 70%.

3-4-1 Set O: Preliminary Study

O1 Selecting Boundary Conditions: The sets of prescribed conditions outlined in the previous section are tested for their response. The results are then used to determine which model will be used for the ensuing studies.

O2 TBC Temperature Distribution Sensitivity: The parametric studies focused on the TBC system response to one cooling down cycle during typical operative conditions. Since the load is primarily thermally driven, this sub-study documented how the system responds to an overload cycle.

O3 Self-Healing TBC Temperature Distribution Sensitivity : Since the presence of particles changes the global thermo-mechanical response of the TBC system, another set of models testing overload was created.

O4 Mesh Convergence Study: The element lengths used for the remainder of the parametric study were chosen in accordance to the characteristic lengths derived from material properties of the different constituents in the system. Because the dimensions of the domain are in the same order of magnitude as the characteristic length of the most brittle material, the range of available values did not present a trade-off to computation time. Nevertheless, to ensure that crack propagation convergences with mesh refinement, a set of models were developed with a variety of element lengths less than μm.

Set ID	Average cohesive element length
O4.1	0.008
O4.2	0.003
O4.3	0.002

Table 3-3: O4 parameters

Parameter	Value	Units
TC/BC/TGO Thickness	500/8/200	μm
Domain Width	500	μm
Interface Peaks	3	-
Interface Amplitude	1.5	μm

Table 3-4: Base Parameters

3-4-2 Set A: Conventional TBC

A1 Varying Strength Properties: The pore distribution and lamellae morphology are kept constant, while the lamellae strengths are varied. The base model used in the remainder of the study incorporates lamellae interface strength properties that are 80% of the bulk value. The strength properties in this sub-set, the lamellae interface values were reduced by 60% and 30%. A lamellae-free model is also considered for further reference. The results will be used to gain insight on if and how the bonding ratio between lamellae interfaces, a property that can be manipulated during processing, effect fracture behaviour.

A2 Varying Lamellae Morphology: This subset consists of six trials in which the lamellae dimensions and morphology are varied while the pore distribution and strength properties are kept constant, and is designed to determine whether lamellae consistency drives fracture behaviour.

A3 Varying Lamellae Morphology and Pore Distribution: In order to measure the variability of fracture behaviour to overall morphology, three sets of five trials were conducted in which both the pore distribution and the lamellae morphology are varied.

A4 Varying Lamellae Morphology (No Pores): To separate the influence of pores on the lamellae morphology, a set of models were created composed of monolithic TCs.

3-4-3 Set B: Self-Healing TBC

B1 Varying Lamellae Morphology: The particle and pore distribution is kept constant while the lamellae morphology is varied.

B2 Varying Particle/Pore Distribution and Lamellae Morphology: The influence of the overall morphology on fracture behaviour is once again surveyed in three sets of five trials in which the pore, particle and lamellae morphologies are all varied.

Set	ID	A_p	l_l	t_l	σ_{li}	G_{li}
A1	A1.1-3a	12	55	17	320	0.153
A1	A1.1-3b	12	55	17	200	0.08
A1	A1.1-3c	12	55	17	120	0.048
A2	A2.1	12	55	17	320	0.153
A2	A2.2	12	100	17	320	0.153
A2	A2.3	12	20	17	320	0.153
A2	A2.4	12	55	17	320	0.153
A2	A2.5	12	55	12.5	320	0.153
A3	A3.1a-c	12	55	17	320	0.153
A3	A3.2a-c	12	100	17	320	0.153
A3	A3.3a-c	12	20	17	320	0.153
A3	A3.4a-c	12	55	17	320	0.153
A3	A3.5a-c	12	55	12.5	320	0.153
A4	A4.1	0	55	17	320	0.153
A4	A4.2	0	100	17	320	0.153
A4	A4.3	0	20	17	320	0.153
A4	A4.4	0	55	17	320	0.153
A4	A4.5	0	55	12.5	320	0.153

Table 3-5: Set A Parametric Variables

B3 Varying Particle Size: In Set B3a, the pore and particle distribution, as well as lamellae morphology are kept constant, while the size of the particles are changed. In Set B3b, the lamellae are removed and the same pore and particle distributions used in Set B3a are implemented with varying particle sizes.

3-5 Post-Processing Methodology

The primary response of interest in the parametric studies is the damage undergone by the cohesive elements. The history output variables extracted from the Abaqus odb files of the parametric sets includes the scalar degradation factor (SDEG), strain and displacement for all the cohesive elements within the model. In ABAQUS, this is represented by the damage variable (SDEG). Damage is initiated when the material strength is exceeded, and from that point proceeds to irreversibly increase. This normalized variable increases from 0 to 1, which causes the elasticity of the cohesive element to reduce by a factor of (1-D).

The cohesive elements are ascribed a very high initial stiffness value of 10^{10}. This was done in order to ensure that cohesive elements show no displacement until crack initiation occurs While all cohesive elements showing damage values above 0 indicate that stress in that region has exceeded the material strength and fracture energy is being dissipated, the cohesive elements only begin to exhibit non-negligible strain at D≈0.9999, since the cohesive elastic modulus is then in the same order of magnitude as the elastic moduli of the bulk elements.

Since the analyses only considers one load, elements that show relatively more damage provide information on morphology-fracture interaction. It should be noted that since the area under

Set	ID	A_p	t_l	l_l	σ_{li}	G_{li}	A_{sh}	r_{sh}	σ_{sh}	G_{sh}	$\sigma_{sh,i}$	$G_{sh,i}$
B1	B1.1	12	17	55	320	0.153	10	10	280	0.126	310	0.11
B1	B1.2	12	17	100	320	0.153	10	10	280	0.126	310	0.11
B1	B1.3	12	17	20	320	0.153	10	10	280	0.126	310	0.11
B1	B1.4	12	17	55	320	0.153	10	10	280	0.126	310	0.11
B1	B1.5	12	17	55	320	0.153	10	10	280	0.126	310	0.11
B1	B1.6	12	n/a	n/a	320	0.153	10	10	280	0.126	310	0.11
B2	B2.1a-c	12	17	55	320	0.153	10	10	280	0.126	310	0.11
B2	B2.2a-c	12	17	55	320	0.153	15	10	280	0.126	310	0.11
B2	B2.3a-c	12	17	55	320	0.153	5	10	280	0.126	310	0.11
B2	B2.4a-c	12	17	55	320	0.153	10	20	280	0.126	310	0.11
B2	B2.5a-c	12	17	55	320	0.153	10	7.5	280	0.126	310	0.11
B3	B3.1a	12	17	55	320	0.153	5	10	280	0.126	310	0.11
B3	B3.2a	12	17	55	320	0.153	10	10	280	0.126	310	0.11
B3	B3.3a	12	17	55	320	0.153	15	10	280	0.126	310	0.11
B3	B3.1b	12	17	55	320	0.16	5	10	280	0.126	310	0.11
B3	B3.2b	12	17	55	320	0.16	10	10	280	0.126	310	0.11
B3	B3.3b	12	17	55	320	0.16	15	10	280	0.126	310	0.11

Table 3-6: Set B Parametric Variables

the traction-separation curve, equating to the fracture toughness of the material, is fixed throughout the analysis, the energy required to induce an incremental increase in the damage variable reduces as the damage variable increases. In other words, much less energy is required to progress from a damage parameter of 0.999 to 0.9999, than from 0.99 to 0.999. The dissipated damage energy is another output that is complementary to the damage variable, and can be calculated as a function of the cohesive element tensile strain δ_n and shear strain δ_s:

$$D = \frac{\lambda - \epsilon_0}{\epsilon_u - \epsilon_0};\ \epsilon_0 = \frac{\sigma}{K}; \epsilon_u = \frac{2G}{\sigma}$$

$$\lambda{=}\sqrt{\langle\delta_n\rangle^2 + \delta_s^2};\ \langle x\rangle = \frac{1}{2}(\delta_n + |\delta_n|)$$

The damage dissipation energy (in contrast to the damage variable) can be used to distinguish whether the failure of the cohesive element is mode I or mode II.

The damage variables derived from the ABAQUS job are used to develop three additional output to facilitate comparison between the models in the parametric set. The sum of cohesive elements exceeding the damage threshold value at a given point in the analysis is plotted against the step increment to evaluate crack progression. From this information, it is possible to discern the rate at which crack growth took place i.e. whether damage progression was taking place at an increasing rate, or whether initial damage alleviated stress from the model so as to slow down damage progression. Conversely, the severity of the fracture within the model was evaluated by implementing the strained area of the cohesive elements following damage. While this factor may be used as a measure of the severity of the cracks, this holds special relevance to the models containing healing particles as the diffusion of healing liquid is enabled by higher fracture volumes. Both the cumulative crack length and crack area at a given time increment is plotted for each region in the TBC system; namely, the BC, the lamellae, the lamellae interfaces, the TGO and the healing particles(for parametric sets B). The damaged elements are implemented into a plot of the model microstructure for qualitative assessment of the crack trajectories.

Chapter 4

Set O: Preliminary Study

4-1 O1 Selecting Boundary Conditions

The purpose of preliminary study O1 was to study the effect of varying the boundary conditions of the model to represent different experimental conditions. The models used in this sub-study contained lamellae only, an no pores or healing particles in the TC. The same average lamellae dimensions were used (average width of 55 μm and thickness of 17 μm). Insight gained from the study was used to select the boundary conditions for the sets of parametric studies that follows, judged on computational efficiency and degree of agreement with empirical observations. The crack patterns derived from each model in the set is displayed in Figure 4-2. All crack patterns were derived from damage values exceeding 0.9999, with the exception of O.2, which used 0.999. A description of the output derived from each model is elaborated upon below:

Model 1: produces a solution in which the top-coat surface spallates primarily through mode II fracture. The shear tearing is followed by the spallation of the top-coat from the TGO. Both modes of failure occurred within the span of 0.001 increment of the step, so they appear to fracture in a brittle manner, as load is not allowed to dissipate to other regions following crack initiation. The coating experiences top coat failure because of the thermal strain differences between the three layers of material and the substrate. The substrate, always being a metal, has the highest thermal expansion coefficient of the system, and will therefore experience the highest contractive strain. Because the three TBC layers are enforced to comply to this strain, the compressive stress they experience will be the difference between the substrate strain and their own.

This result is not supportive of the empirical observations of fracture modes made in TBC systems, which mostly document cracks nucleating at the TGO substrate and eventual spallation of the top coat from the TGO. The top coat surface does not typically fragment due to shear loading. This fragmentation may prove to be suppressed if a 3D rendition were used as the geometry instead, as external material will provide resistance. Total failure may also have occurred due to the absence of strain relief that segmentation cracks and pores offer.

Layer	Thermal Contraction Strain	Difference with Substrate	Stress [MPa]
TC	-0.0064	0.0027	540
TGO	-0.0042	0.0042	1862
BC	-0.0085	0.0085	120
Substrate	-0.0091	-	-

Table 4-1: Thermal Contraction Strains of TBC System

Model 2: The substrate temperature was decreased to 800, 900 and 1000°C and the top-coat surface was kept at 1200°C. The load case resultant from a model with a non-uniform thermal load is markedly different from when the thermal field is initially uniform. Figure 4-1 shows how the relatively high temperature of the top coat surface makes its thermal strain more compatible with that of the substrate, which experiences a net lower strain due to the lower temperature it is attributed.

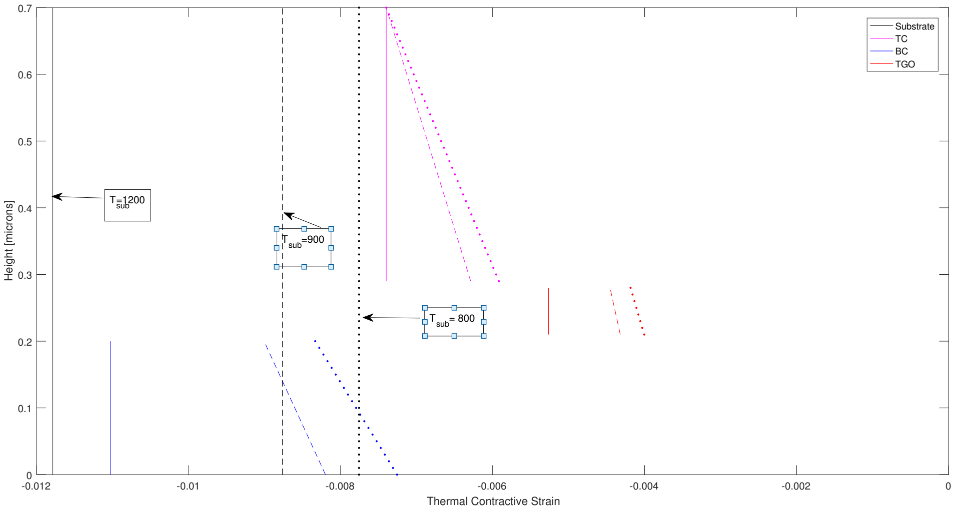

Figure 4-1: Non-uniform Initial Temperature Field Thermal Strains

The effect becomes more pronounced when using higher initial temperature ratios. The model with a substrate temperature of 1000°C still showed top-coat spallation, but the crack nucleates at the base of the model instead of the surface. However, below this temperature, the surface of the top-coat was completely undamaged. The results reflect this, as the top-coat does not spallate as it does in Model 1. Instead, cracks nucleate at the TGO and propagate into the BC. Substrate temperatures of 900°C and 1000°C both instigate top-coat shear failure, though to a lesser degree, since crack nucleation begins at the TC/TGO interface prior to shear failure of the top surface, allowing fracture energy to dissipate through the length of the TC.

Model 3: The strain imposed on the left and right side nodes were alleviated at the top-coat surface between 2%, 5% and 10%. Model 3 did not yield results showing significant differences from Model I, as failure still nucleated at the top-coat surface. This is to be expected when examining the results attained from Model 2, since the thermal mismatch strain alleviation due to an initial temperature gradient is much larger, and yet top-coat spallation still occurs at substrate temperatures 900°C and 1000°C .

Model 4: The use of axisymmetric model necessitated distinguishing an axis of symmetry within the model, and for the purpose of the simulation, this was the right lateral side of the geometry. The symmetric axis was prescribed zero displacement for the duration of the analysis, meaning that only the left lateral side was allowed displacement due to thermal contraction. The contractive load directed toward the symmetric axis caused occurring damage to be localized to this region.

Model 5: The “damaged” cohesive elements that were imposed on the TC/TGO interface were attributed a strength of 10 MPa and a toughness of 0.01, causing them to be significantly weaker than their surrounding elements. However, it was shown that the weakened elements did not propitiate crack nucleation. This is true even when in combination with Model II, which showed crack propagation to occur in the TGO. With respect to LEFM, cracks tend to nucleate in regions of lower strength, as these areas will yield earlier at cause stress concentrations to occur. However, since fracture initiates at the top surface, the expected stress concentrations occur after shear-failure has taken place.

Model 6: In Model 5, the mode II strength and toughness values were artificially increased so as to prohibit cohesive elements from separating due to high σ_{12} values. In combination with Model 1, which by itself produced mode II failure, the elements do not separate but rather slide against each other, both on the TC surface and from the TGO into the TC. This is because the toughness value determines the area under the traction-separation curve that governs the response of the cohesive elements. Increasing this value subsequently extends the load necessary for complete separation to occur.

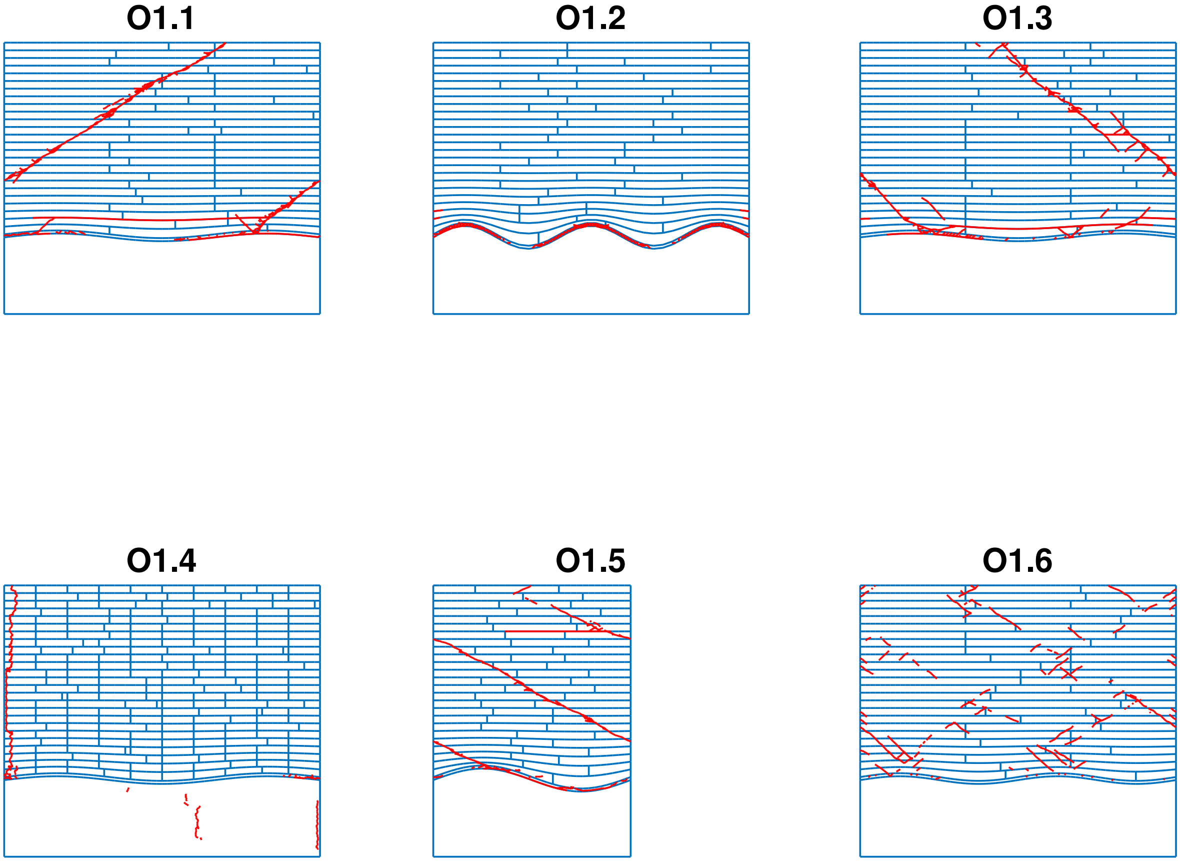

Figure 4-2: **O1** Crack Patterns

4-1-1 O1 Summary and Discussion

In the selection procedure for the parametric study base model, Model 4 (the axisymmetric model) was not taken in consideration. Since the axisymmetric model essentially represents the 2D representation of the microstructure as rotationally symmetric about one of the lateral axes, which is to remain stationary, the stress state that develops is more of a uniaxial compressive stress case than a symmetric thermal loading. Model 1, regardless of the microstructure morphology implemented, always incurred shear-tearing of the top-surface followed by delamination of TC/TGO interface. Model 2 and 3, to a higher and lesser degree respectively, included mechanisms that alleviated the strain mismatch that acts as the main driving mechanism for failure. Model 5 prohibited the top-surface tearing by suppressing Mode II fracture, maintaining a stable stress distribution so that the TBC remains intact. Models 1,3 and 5 essentially exhibit the same mode of fracture while Mode 2 implicates a significantly different load distribution. The selection procedure therefore consisted of deliberating between the two failure modes observed.

The primary advantage of Model 2 is that it shows better correlation with empirical results. The primary disadvantage is that there are comparatively less experimental set-ups that implement a uniform thermal gradient along the coating thickness. This disadvantage is offset by the considering that Model 2 more accurately represents operative conditions. While Model 1 is representative of four of the five studies surveyed prior to this analysis, the high flexure stress that drives the shear tearing along the top-coat surface may be alleviated by free-edge and other 3D effects that cannot be directly enforced into the 2D geometric representation, nor can these effects be easily identified or quantified during experiments. Conservative values of strain alleviation implemented in Model 3 do not alleviate the flexural stresses enough to suppress the shear tearing. Since this tearing is the first crack to nucleate within the model, subsequent cracks that nucleate at the TGO region will be effected by the shifted stress distribution, which will induce an effect on their trajectories.

Model 2 was chosen for the parametric analysis because it produced results that more accurately reflects empirical observations and furthermore, is more aligned with actual operative conditions. To further refine this model, non-destructive techniques can be used to measure the temperature distribution through the thickness of the TC so as to refine the initial temperature field equation, which was assumed to be linear. An additional reason for choosing this model is that typical convergence periods are four times less than that required for Model 1.

4-2 O2: TBC Model Temperature Sensitivity

Study O2 tested the sensitivity of the TBC system model to varying initial temperature assignments. The results shown in Figure 4-3 show that the models are highly sensitive to the substrate temperature. Increasing the substrate temperature increases the damage induced on the specimen, while increasing the surface temperature has the opposite effect. The reasoning behind this trend can be understood by referring to Figure 4-1. Increasing the temperature essentially decreases the thermal strain mismatch between the substrate and the separate TBC components. Increasing the substrate temperature , on the other hand, widens the mismatch strain and introduces higher stresses into the analysis, since essentially, this would be the same as increasing the prescribed displacement. The growth in crack length displayed in Figure 4-4 shows gradual crack growth for every instance except when the substrate temperature is 900°C. Shear tearing that the overload produces causes instable crack growth that brings about intervals of brittle fracture that occur throughout the domain due to compromised load-bearing capacity.

4-3 O3: Self-Healing TBC Model Temperature Sensitivity

The results from sub-study O3, as judged by the cracks patterns presented in Figure 4-5 , are in agreement with the insights gained from O2 on how substrate temperature exerts a higher degree of influence on fracture behaviour. Study the crack lengths (Figure 4-6) however, shows that the particular geometry used in O3 shows more consistent crack patterns than O2, though it should be noted that this is not necessarily the case due to the presence of healing particles. The overload cycle, rather that showing sporadic growth as O2.1 does, instead exhibits controlled growth until brittle fracture occurs towards the end of the load cycle.

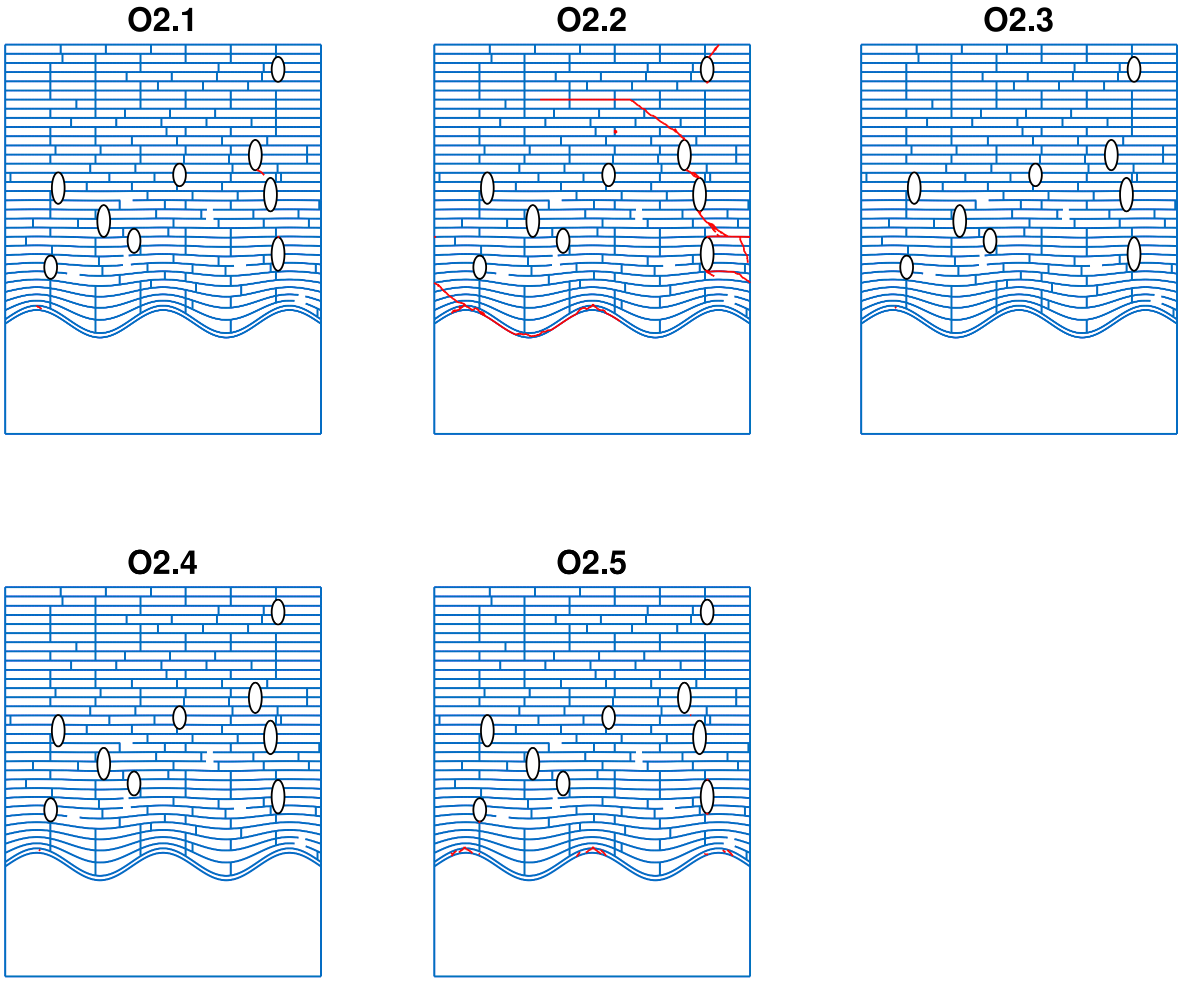

Figure 4-3: O2 Crack Patterns

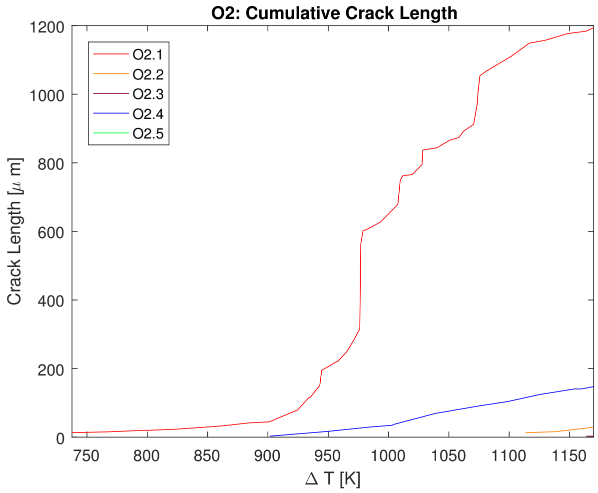

Figure 4-4: O2 Cumulative Crack Length

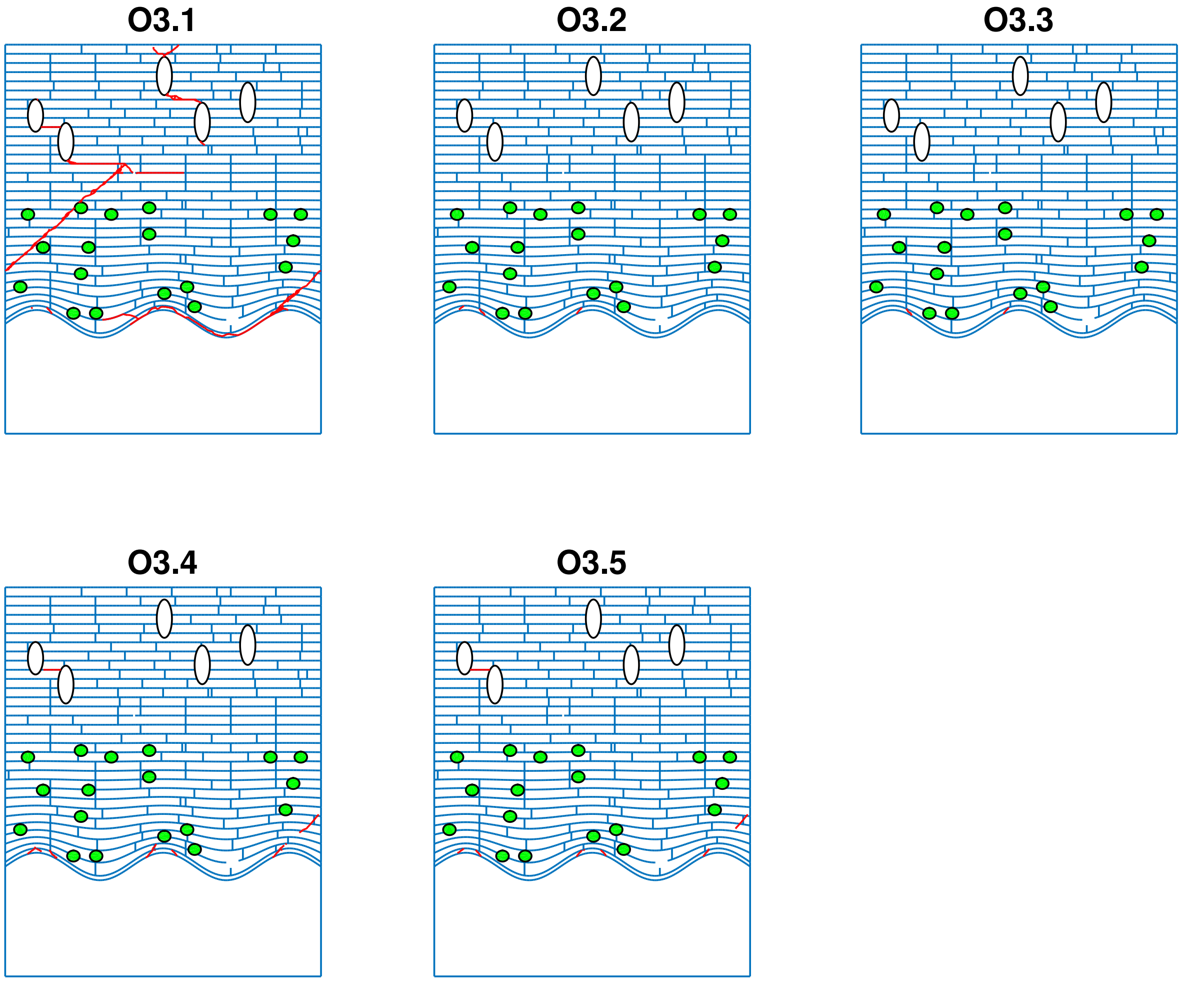

Figure 4-5: O3 Crack Patterns

4-4 O4: Mesh Convergence

The mesh convergence study comprised of three models with the same geometry but with differing mesh element parameters. The average cohesive lengths used in the three models is summarized in Table 3-3.

Observing the SDEG distribution chart shown in Figure 4-8, it can be seen that the percentage of damaged cohesive elements consistently decreases with decreasing length of the cohesive element. This is true for all intervals except 0.999<D<1 and D<0.9. O4.3, which has the smallest average cohesive element length, the percentage of elements that fall within these intervals is slightly more than O4.2. Another metric from convergence is the damage energy dissipated with time increment. Figure 4-7 shows that the energy dissipation rates for O4.2 and O4.3 are comparable, but O4.1 clearly shows a much higher damage rate.

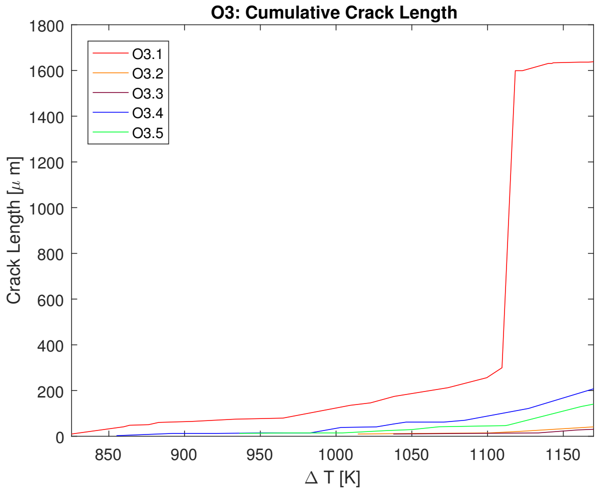

Figure 4-6: O3 Cumulative Crack Length

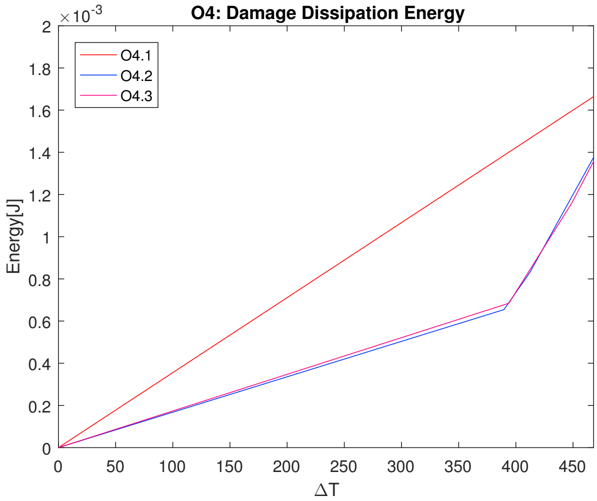

Figure 4-7: O4 Damage Dissipation Energy

4-5 Discussion

The purpose of the preliminary study was to establish the prescribed conditions for the ensuing studies that test the fracture response of conventional and self-healing TBC systems. The first step towards achieving this objective was selecting a set of boundary conditions that would simulate TBC testing conditions. The criteria utilized to select among one of the options was the degree of resemblance that the output had to empirical observations and convergence time. After deliberation over the results, Model 2 was chosen, which is distinguished by the implementation of a initial temperature field that varies along the length of the TBC system. Figures 4-9 and 4-10 show the maximum in-plane stress, S11, S12 and S22 distributions along the domain for the conventional and self-healing TBC variants respectively.

Observing 4-9, it can be seen that the pores appear to produce a field of positive S11 stresses and negative stresses in their vicinity, while the bulk material in the TC possess S11 and S22 stresses that are positive and negative respectively. Another noteworthy observation are that

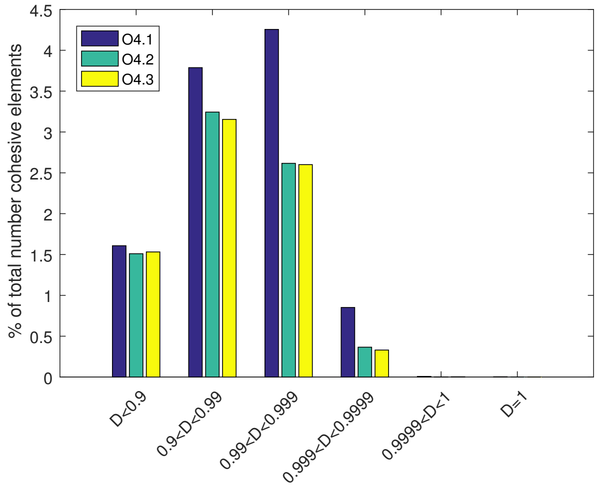

Figure 4-8: O4 SDEG distribution

the stress concentrations that develop at the top and bottom of pores merge with another when situated close to one another, producing a combined effect that is greater than the sum of their individual severity. In the self-healing model, this effect is perceivable between clustered self-healing particles only when observing the maximum in-plane stress distribution, but the combined severity does not manifest to the same degree. This is due to the circular geometries, which produce milder stress concentrations than highly elongated ellipses. The healing particles noticeably introduce compressive stresses to the domain, causing the in-plane stresses in the bulk material of the TC to be positive instead of negative in the TC.

Studies O2 and O3 tested the model sensitivity to using different initial temperatures for both the substrate and the TC surface. Both studies yielded results that suggest that damage is alleviated by increasing surface temperature. Finally, a mesh convergence study was executed (O4). The results revealed that the percentage of damaged elements decreases with decreasing cohesive element length. It was concluded that an average cohesive element length of 0.008 is too coarse, as the energy dissipated due to damage clearly reduces as the element length is lessened. Considering this, the average element length implemented in the model is 0.003.

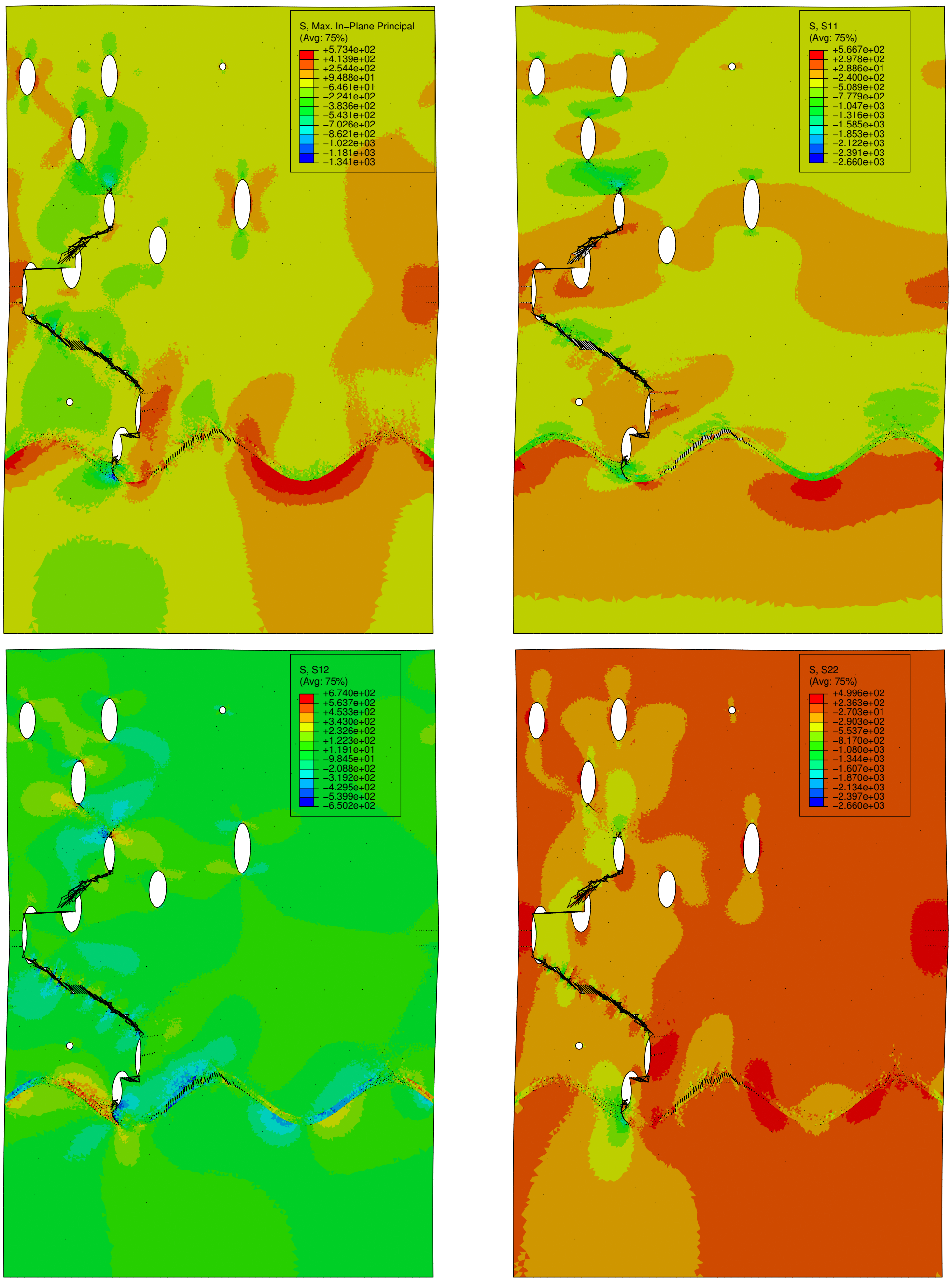

Figure 4-9: Conventional TBC Stress Distributions

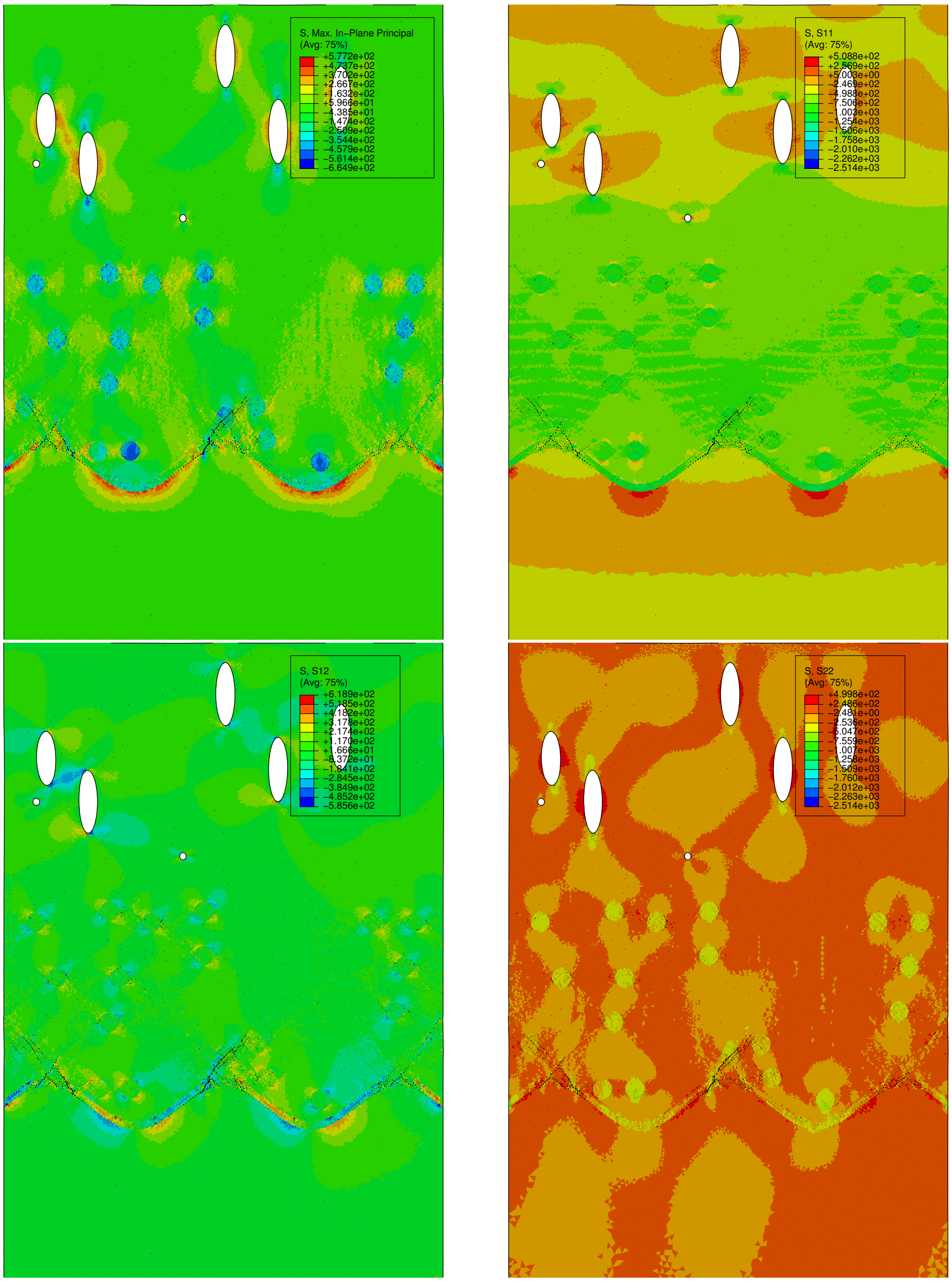

Figure 4-10: Self-Healing TBC Stress Distributions

Chapter 5

Parametric Study A

This section presents the results achieved from Parametric Study A, which focused on model geometry that is representative of conventional TBC coatings consisting of a heterogeneous top-coat comprised of lamellae and pores, and monolithic TGO and BC layers. The lamellae were distinguished from one another by assigning the cohesive elements lying along the interface attenuated material toughness and strength values. This value is 80% of the full cohesive properties of the top-coat unless otherwise stated. The pores were randomly distributed throughout the domain at a surface area percentage of 12%. They were elliptical in shape and oriented vertically, with the minor-major axis ratios between 1:2 and 1:3. A1 studied the effect of varying the lamellae strength properties. A2 focused on the effect of changing lamellae dimensions while keeping the pore morphology constant. A3 comprised of geometries that had arbitrary pore distributions with fixed lamellae dimensions, thus examining whether a generalized response can be attributed to varying lamellae morphologies. A4 examined the fracture behaviour of TBCs without pores. The intended purpose of Set A was to gauge whether or not the presence of lamellae influenced fracture behavior, and if my controlling the microstructure, the fracture behaviour can also be controlled. Post-processing of the results utilized a D_{thres}value of 0.9999. After the results for each separate sub-study have been presented and discussed, this section conclusion with a consolidation of the implications of the results.

5-1 A1

Parametric study A1 examined the effect of varying lamellae interface strength and toughness on fracture behaviour using the same morphology. Decreasing the strength will hasten damage initiation, and decreasing the toughness will lower the fracture energy required for complete failure to occur. Essentially, these properties can be used to define the bonding ratio between the lamellae, which can be controlled during TBC processing. A perfectly bonded top-coat will entail that the lamellae interface strength and toughness values match that of the bulk material. Therefore, the lamellae interface properties assigned in this set do not exceed that

	p	b		p	b		p	b
A1.1a	3.484	-12.26	A1.2a	3.625	-12.67	A1.3a	3.726	-12.891
A1.1b	3.644	-12.55	A1.2b	3.877	-13.26	A1.3b	4.237	-14.18
A1.1c	3.651	-12.33	A1.2c	3.501	-12.00	A1.3c	4.408	-14.52

Table 5-1: Log-log fit A1 DDE distribution: $DDE = (\Delta T)^p + b$

of the bulk material. The purpose of this set was (a) to discern whether lamellae interface properties asserted an effect on the number of cracks initiated, the crack trajectories and cumulative crack length and areas. Three trial sets were run to (b) measure the degree to which the lamellae interfaces alone have an effect on fracture behaviour.

General trends that can be distinguished from Figure 5-4 are that both the cumulative crack length and area increase in an almost exponential manner with a reduction in strength properties. Another observation that holds true for all trials is that the D_{thres} is reached latest in model with the intermediate strength properties (A1.1-3b). In terms of crack trajectory, which are displayed in Figure 5-3, the results show that cracks do not exclusively extend in response to varying strength properties, but the entire crack morphology also changes. For instance, trial A1.1a has been shown to appear more robust that A1.2a and A1.3a, but the same microstructure with strength properties attenuated by 30% shows the most damage out of the entire subset of trials. This is also noticeable when examining subset A2. The singular crack originating at the TGO interface noticeable in right-lower corner of A1.2a and A1.2b bifurcates into 3 separate cracks in A1.2c. At the end of the analysis, it is shown that relatively more damage occurs at the right-hand side of the geometry. In general, fracture behaviour in stronger models are driven more by pore placement. In weaker models, fracture behaviour is significantly influenced by lamellae interface position.

The consistent increase of the energy dissipated with lowering fracture properties, shown in Figure 5-2 can be used to produce quantitative correlations between the model response and fracture strength and toughness. It is evident from the graph that the damage dissipation curves appear to display a power-law function, with the power increasing with decreasing lamellae interface strength properties. The powers and intercepts from the fitted functions are displayed in Table 5-1. Fitted functions computed for both A1 and A3 confirm this trend. The observation u also holds true for A1.2a-A1.2b, but since the rate of energy dissipation begins to level off towards the end of the analysis in A1.2c, the inverse power-strength relation does not hold for A1.2. Nevertheless, the increase in the power value does hold for earlier increments in the analysis. The data-fitted curves can be viewed in Figure 5-1. It is also interesting to note that the rate of damage dissipation experiences a sudden shift at the same ΔT value for all the trials in each set. The weaker models experience this shift earlier in the load-case than the stronger models. The time-lag can be used to correlated fracture response to lamellae properties even further.

To summarize, it can be stated that the effect on both the numbers of cracks initiated and the crack trajectory are influenced by the strength and toughness values. It was observed in one case how a singular crack that formed in the the stronger two models bifurcated into three separate cracks in the weakest model, in reference to set A1.1. The crack trajectory was also shown to change (A1.1b and A1.1c). Comparisons made between the three trials indicate that decreasing lamellae interface strength values do not produce a consistent degradation

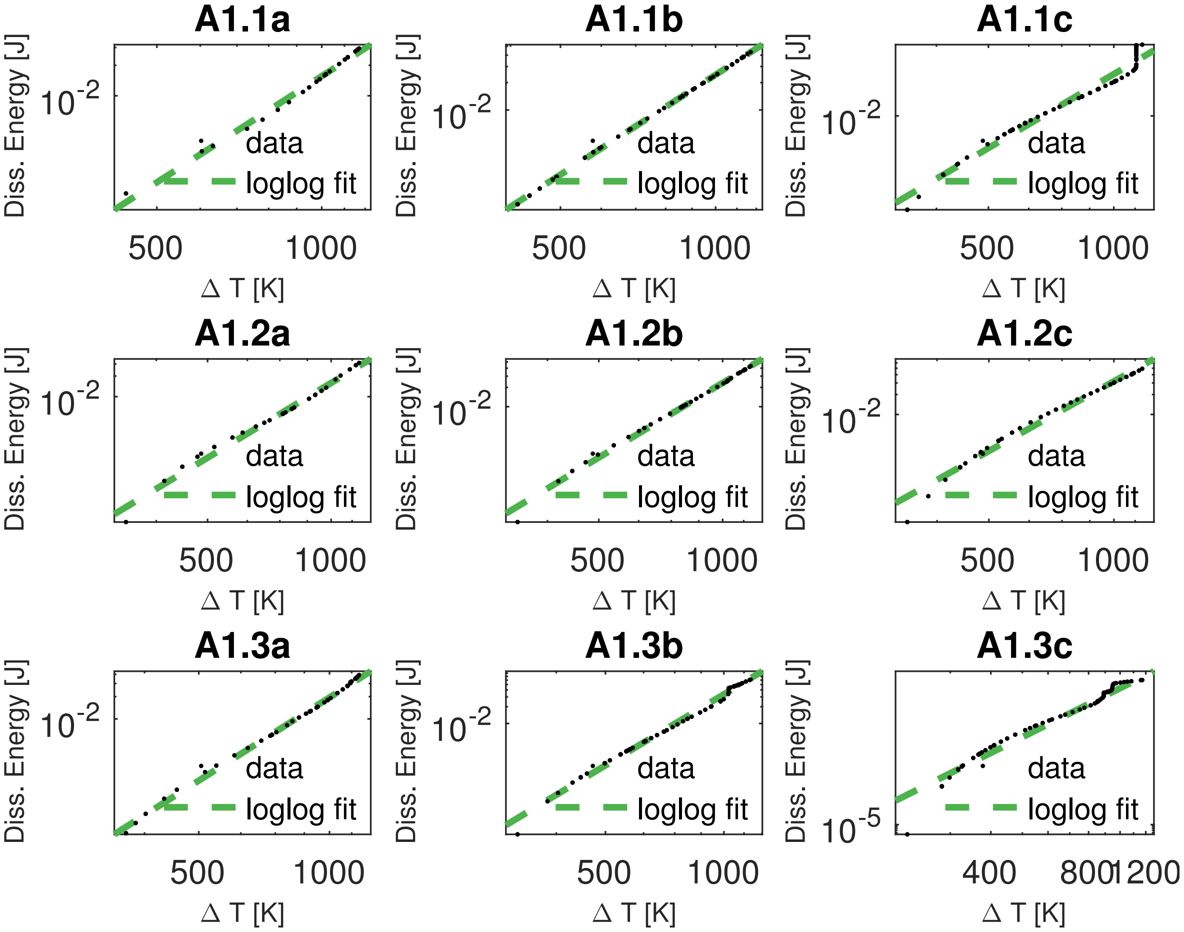

Figure 5-1: A1 Data-Fitting Curves

in fracture resistance. While predictably, in all cases, cumulative damage increased with decreasing strength properties, the degree to which this increases is variable and presumably more dependent on the lamellae morphology and pore distribution. Phenomena identified in this parametric study includes crack branching, which was shown to be facilitated by weak lamellae, the existence of stable and unstable configurations, crack-upon-crack interactions and variability in crack growth rates.

5-2 A2

Parametric Study A2 tested the effect of lamellae morphology in a set of six trials in which the pore distribution and strength properties of the models are kept constant. A survey of the solutions show that the domain contains specific areas that are vulnerable to fracture. An interesting insight that can be taken from the results is that the lamellae morphology alone has an effect on which of the cracks will extend and in which direction. When comparing the crack patterns resultant in models A2.1 and A2.2, for instance, it can be observed that the crack originating at the TGO propagates to the left in the former and towards the right in the latter. Because the placement of the horizontal surfaces of the lamellae in the two models

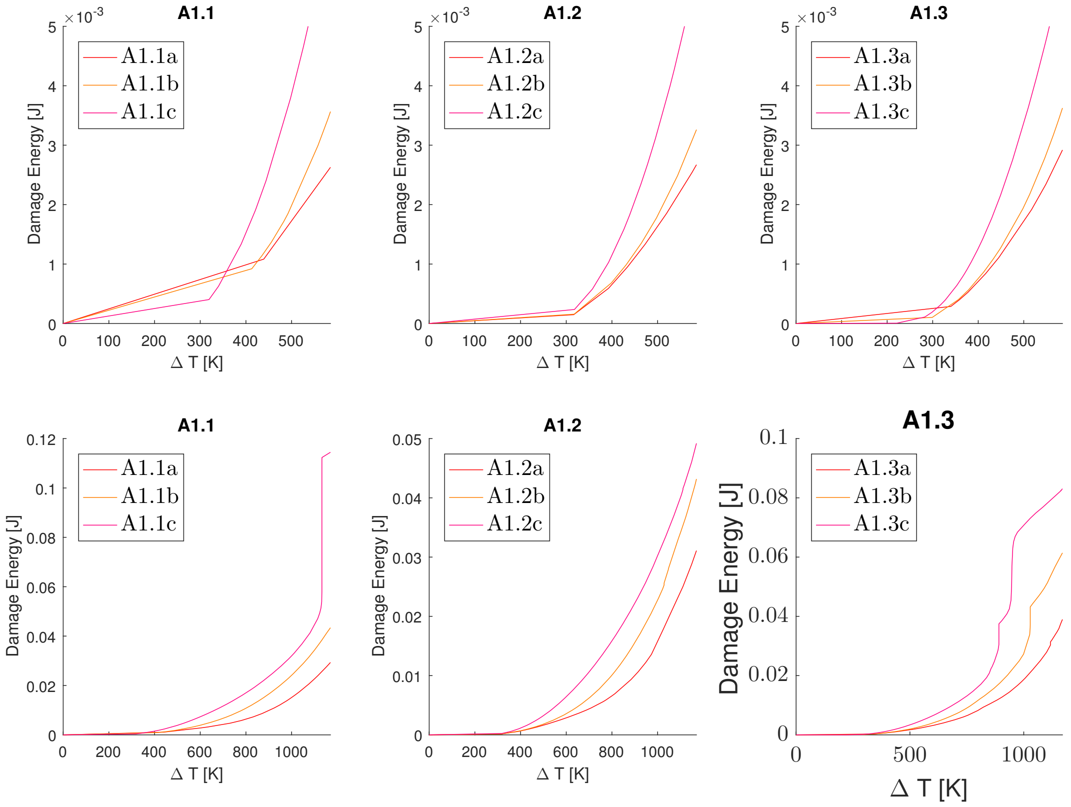

Figure 5-2: A1.1-3 Damage Dissipation Energy

are identical, this effect is presumably due to the difference in number and position of the vertical lamellar interfaces.

Model A2.6, which is representative of a homogeneous top-coat, is revealed to be the most resilient to damage. This supports empirical observations citing that a higher bonding ratio, a value thought to be proportional to the lamellae interface toughness, yield more resilient coatings (see Section 2-2-2). Its changes in crack-length over time increment is characterized by a steady gradient, as seen on the right-hand side of Figure 5-6. The inclusion of a lamellae morphology causes fracture behaviour that is distinguished by more abrupt changes in cumulative crack length, as can be seen in the same figure. Instances of crack interaction are also evident in this set of results. In Model A2.3, for example, the crack coalescence that takes place in all the other models (excluding A2.6) between the two cracks at the right corner of the geometry, is blocked from taking place due to the nucleation of a secondary crack along the TGO.

More insight can be gained by examining the SDEG distribution graph in Figure 5-7 . It is seen that A2.6 has the highest number of cohesive elements that had 0.999<D<0.9999, but the lowest percentage in every other interval. A2.3, which notably resulted in less completely damaged cohesive elements (D=1) than A2.6, contains a proportionally higher amount of elements with D<0.999, which may explain why the response of A2.3 produces less highly damaged cohesive elements than the A2.6. Considering that finer lamellae result originally contain more weakened cohesive elements at the beginning of the analysis, the conclusion that can be drawn from these findings is that weakened elements distributed throughout the

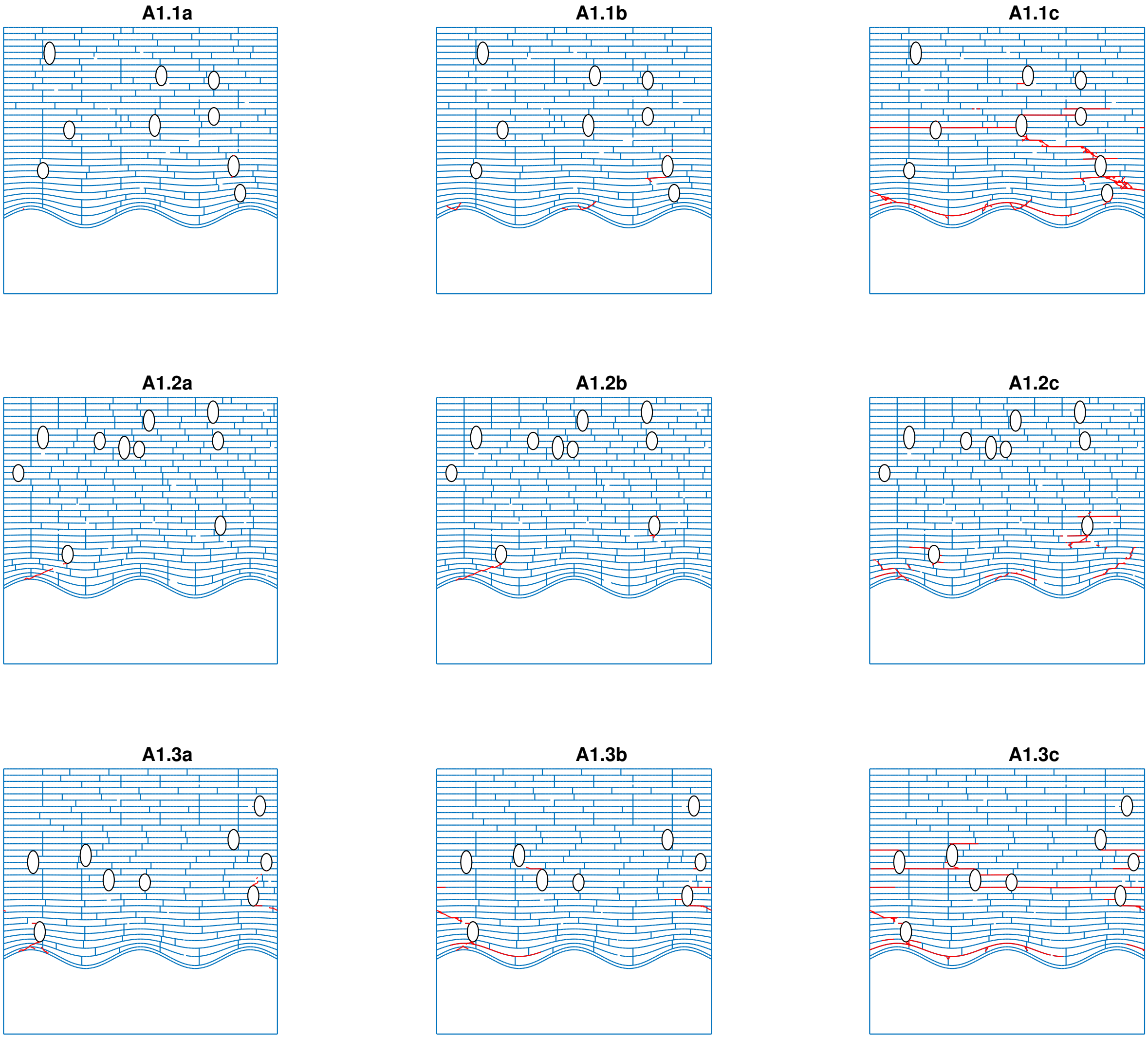

Figure 5-3: A1 Crack Paths

geometry can augment fracture resistance by spreading out the dissipated damage energy across a larger area.

All in all, it is evident that the lamellae morphology does influence fracture behavior. This can be prominently seen by observing A2.1 and A2.2, which shows crack growth directions reversed due to the presence of vertical lamellae interfaces. The results also indicate that larger lamellae lengths are detrimental to fracture resistance. It was seen that the model containing finer lamellae possess fracture resistance properties comparable of that to that of monolithic top-coat.

5-3 A3

Parametric Study A3 was used to discern the relative influence that the pore distribution, lamellae morphology and lamellae dimensions each have on fracture behaviour by comparing several trials that use the same pore volume fraction but not the same pore distribution. Since the lamellae are generated over the new pore distribution, the lamellae morphology changes as well, though the average dimensions are kept the same.

In summary, the results suggest that crack behaviour is more dependent on pore distribution than it is on lamellae morphology. This can be inferred by examining the SDEG distribution graph in Figure 5-9, which shows that each sub-set exhibits more or less the same range as one another. When considering damage initiation as a qualifier for fracture resistance, Figure 5-8 seems to indicate that finer lamellae (A3.3) show D_{thres} values in general later into the load case. While A3.1, A3.2 and A3.5 contain noticeable outliers in terms of crack length, most trials yielded an average crack length of approximately 150μm.

Because the results seem to indicate that total fracture behaviour cannot be generalized for lamellae morphologies embedded in arbitrary pore distributions, effort was redirected into identifying qualitative fracture phenomena that occurs in all sets. Two sets of interactions between cracks and pores can be distinguished by examining the collections of crack patterns of all the samples. The crack patterns for A3 are available in appendix of this report. The first phenomena is crack propagation that “trails” clusters of pores, from those situated closer to the TC/TGO interface to those closer to the surface. Instances of this phenomena are contained in A3.1d, A3.4a and A3.4c. The second phenomena is crack initiation that occurs due to pores situated in the proximity of the TC/TGO interface, at a 45 degree angle from the interface peaks. Models that showed this response in A3.2e, A3.2f, A3.3e and A3.4d.

5-4 A4

Study A4 examined the fracture behaviour of TBC geometries without pores. Two sets of analyses were executed: A4a comprising of the standard initial substrate temperature of 800°C and A4b comprising of an overload cycle in which the substrate temperature is 900°C. The resulting crack patterns showed that damage was constrained mostly to the TGO and the TC/TGO interface. By consulting the SDEG distribution graph in Figure 5-10, it can be seen that in comparison to the SDEG distribution of A3 and A2, A4.3, which is the geometry with finer lamellae, shows visibly more damage than the rest of the trials in the set. The discrepancy is particularly prominent for the values $0.99<D<0.999$. However, A4.2, which is the model with coarse lamellae, is the only model to contain cohesive elements that exceed 0.999 and even show total damage ($D=1$). A4.2 also stands out as an outlier when observing the damage dissipation curves displayed in Figure5-11a. While the dissipation rates overlap for all other models, it is clear that A4.2 shows considerably higher dissipation rates at the beginning of the analysis. The growth rate converges to the rate shown by the other models later in the analysis, though still remaining slightly higher than the rest. Model 4.3a and 4.3b, which contain the finer lamellae representation, both show incrementally lower rates of fracture than the remainder of the models.

5-5 Discussion

Parametric study A investigated the fracture behaviour of conventional TBC systems. Most numerical investigations to date concerning TBCs idealize the top-coat as a monolithic matrix.

When the APS-TBC microstructure is characterized to be composed of lamellae. Study A therefore focused on bridging the knowledge gap by examining the effect that the lamellae structure influences the damage properties of the coating. The ultimate goal of the sub-study was to quantitatively link microstructure properties to fracture behaviour, so the former can be fine-tuned in order to control the latter. Set A1 focused on the effect of varying lamellae strength properties. Results derived from study A1 predictably shows that a sample will undergo more damage when attributed lower interface fracture properties, however, the crack growth graphs appears to imply a proportional relation between the level of property attenuation and damage. While different scaling factors were calculated for the different models used, a more extensive study (i.e Monte Carlo simulations) may yield more applicable heuristic information. Set A2, A3 and A4 focused on the effect of the physical dimensions of the lamellae. These studies heavily imply that finer lamellae impedes fracture. In addition to these conclusions, the results reveal a number of fracture phenomena.

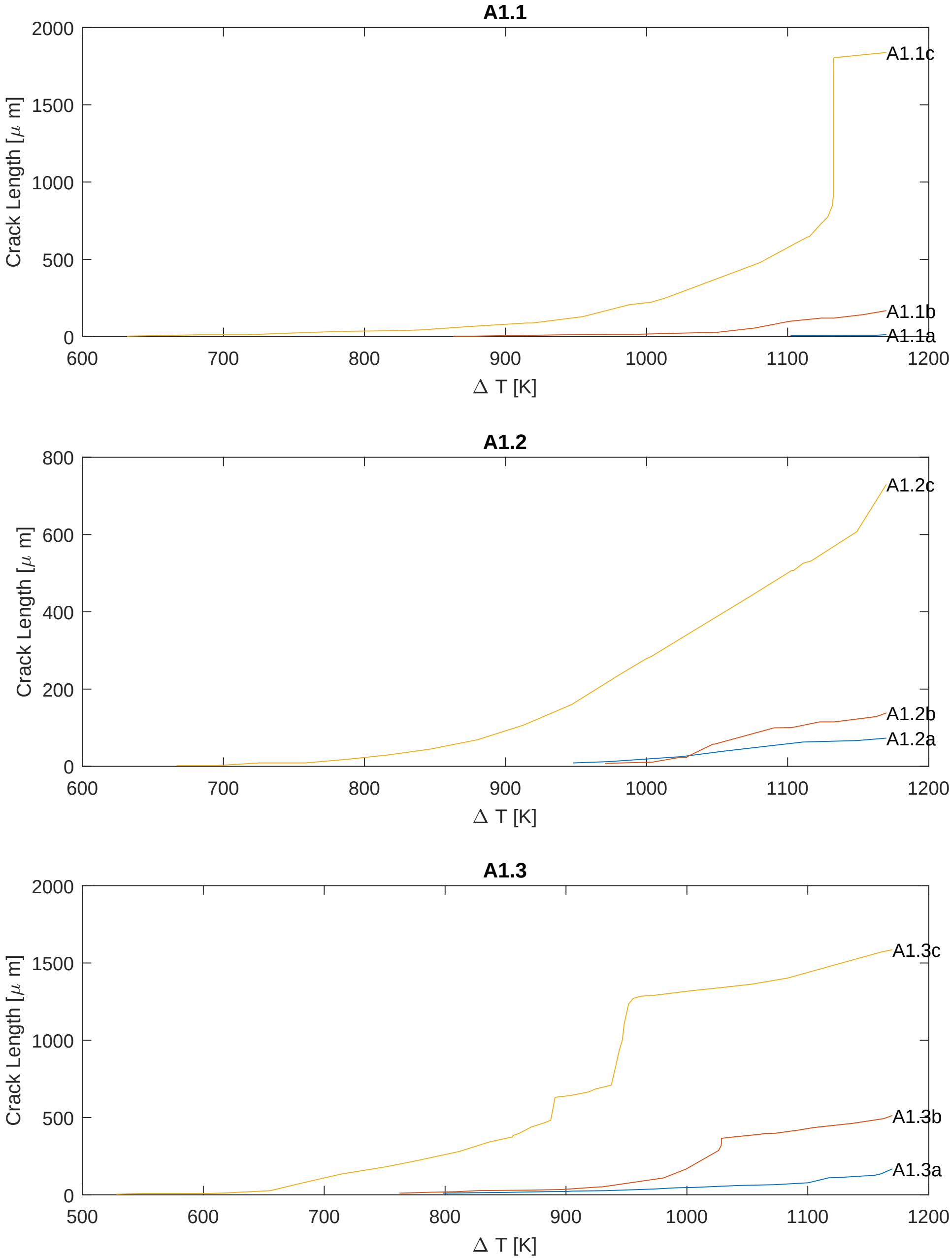

Figure 5-4: **A1** Crack Growth

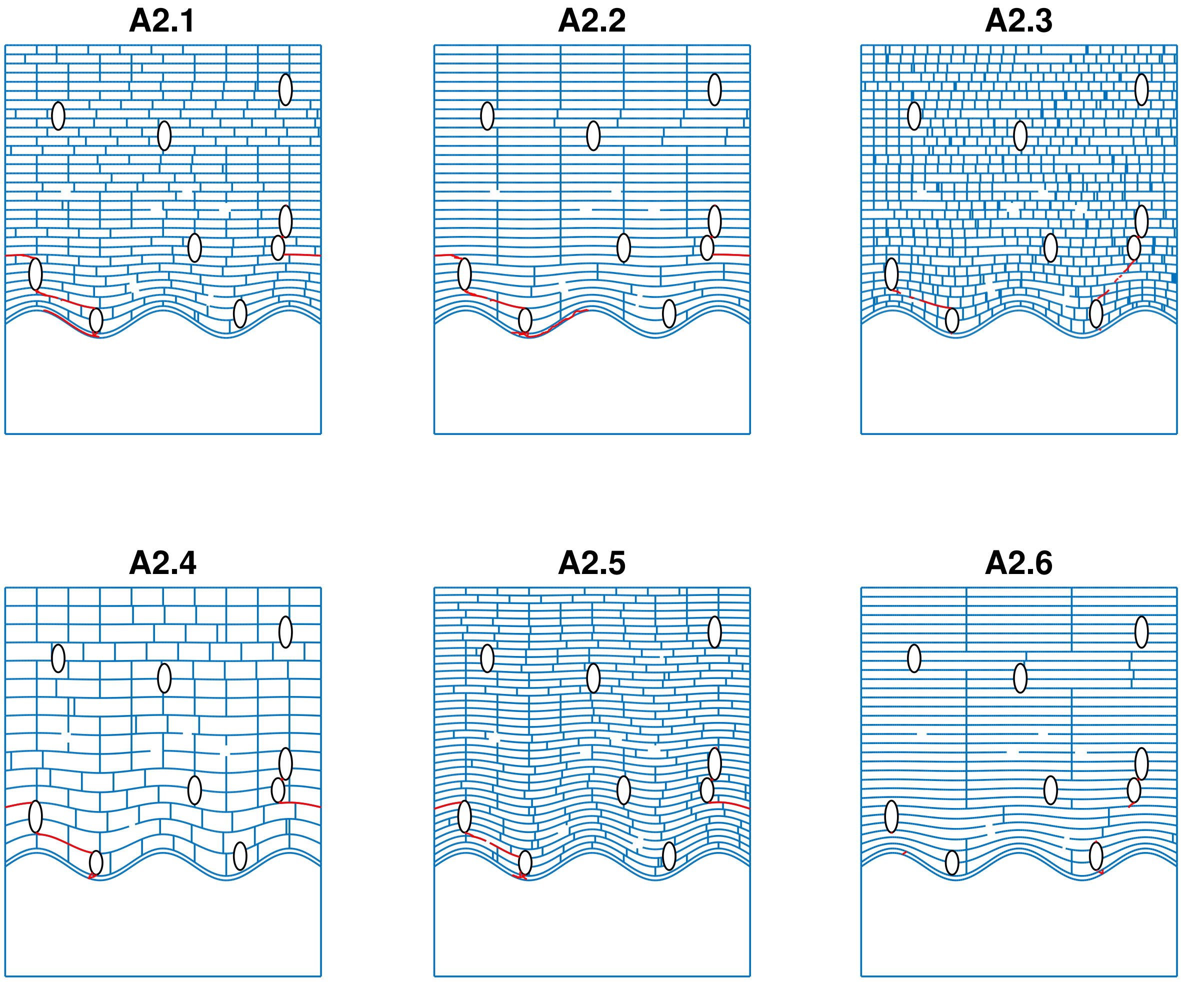

Figure 5-5: **A2** Crack Patterns

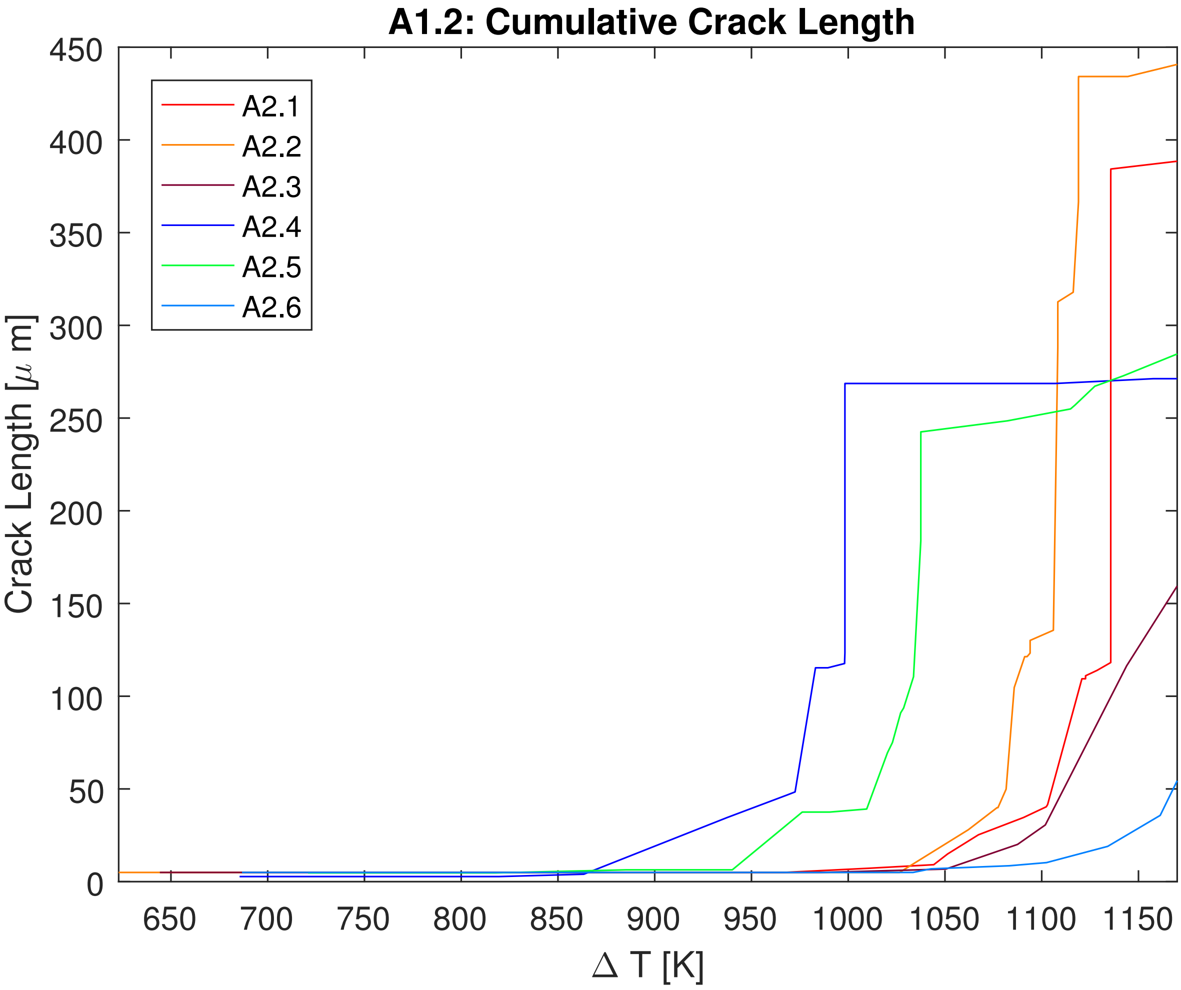

Figure 5-6: A2 Crack Length

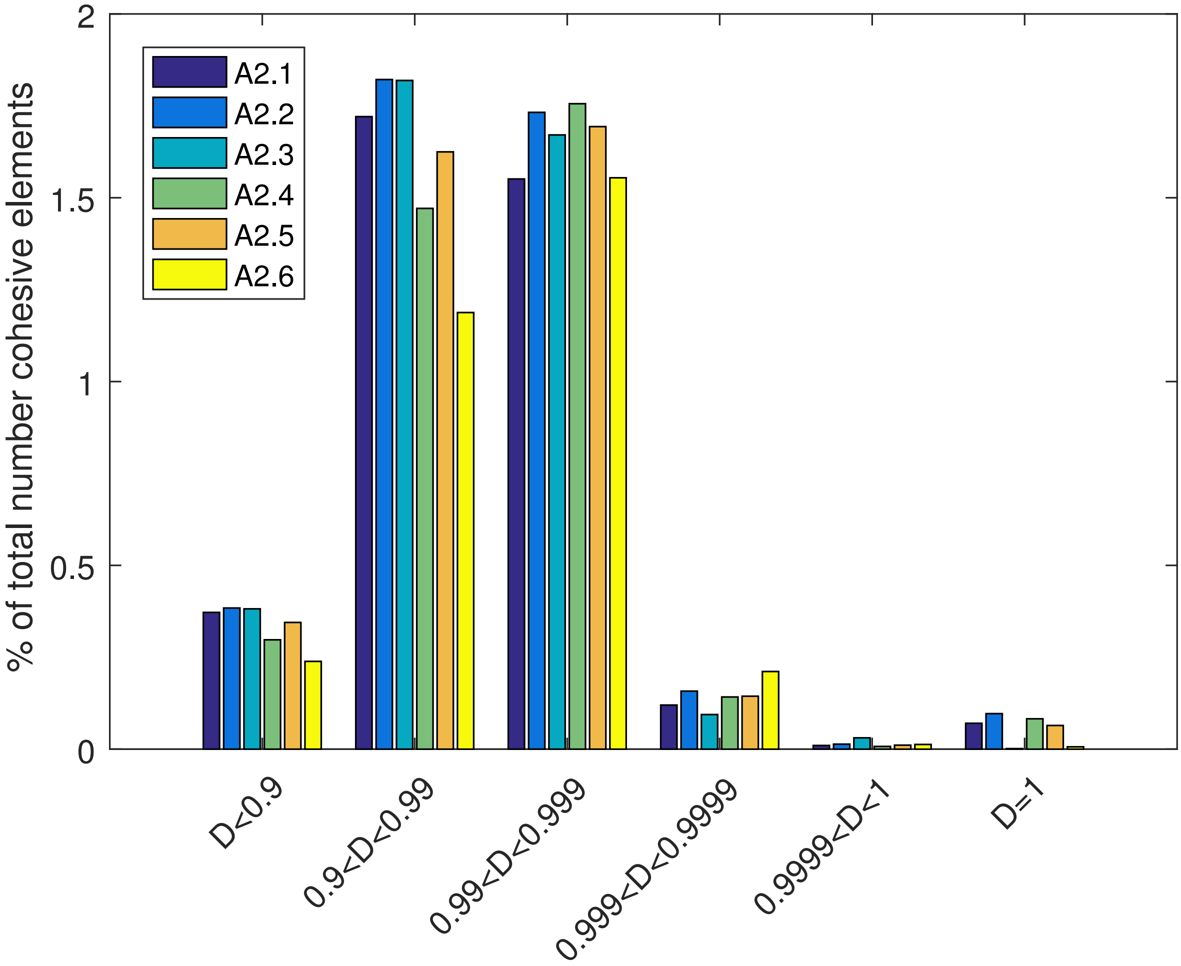

Figure 5-7: **A2** SDEG Distribution

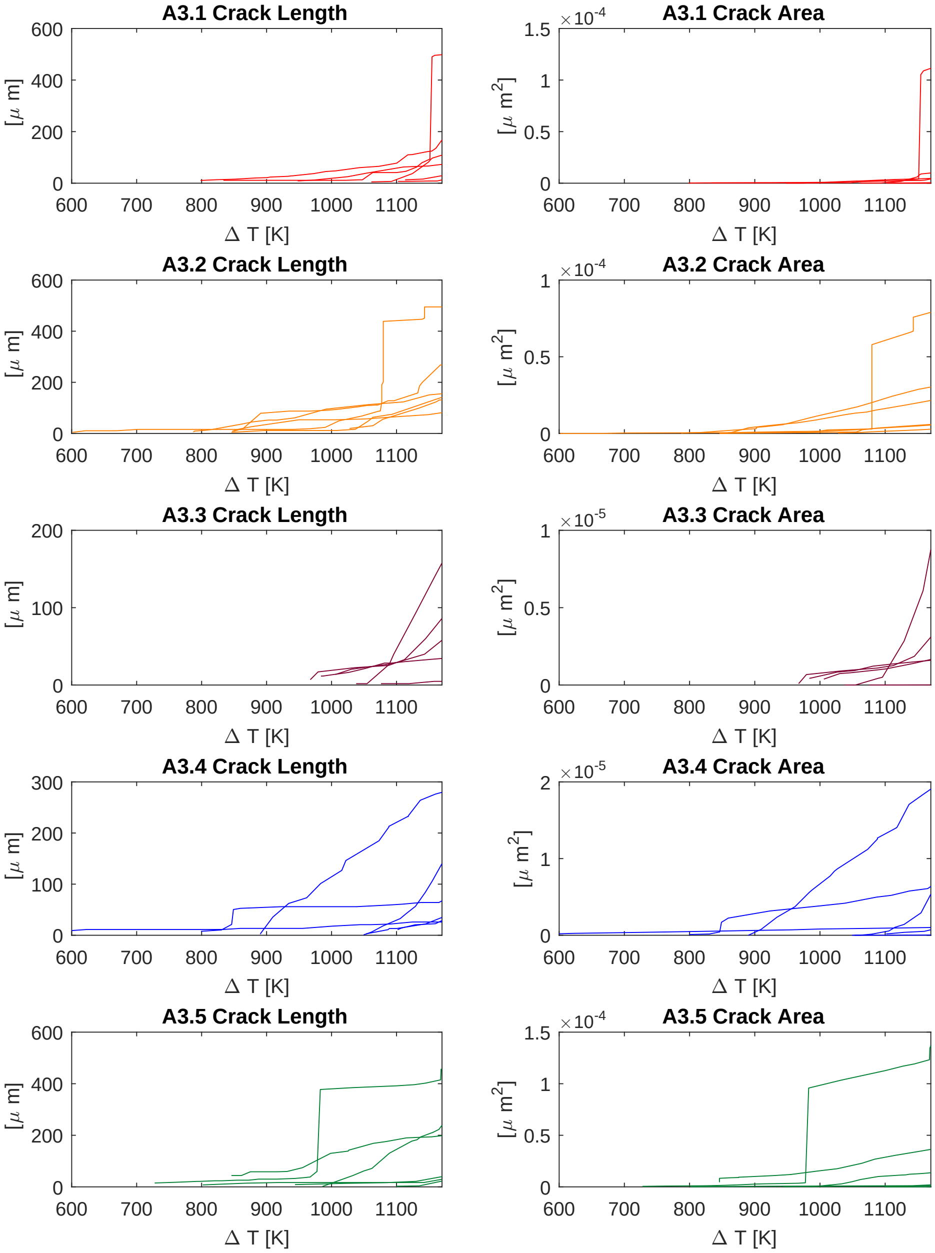

Figure 5-8: A3 Crack Lengths and Areas

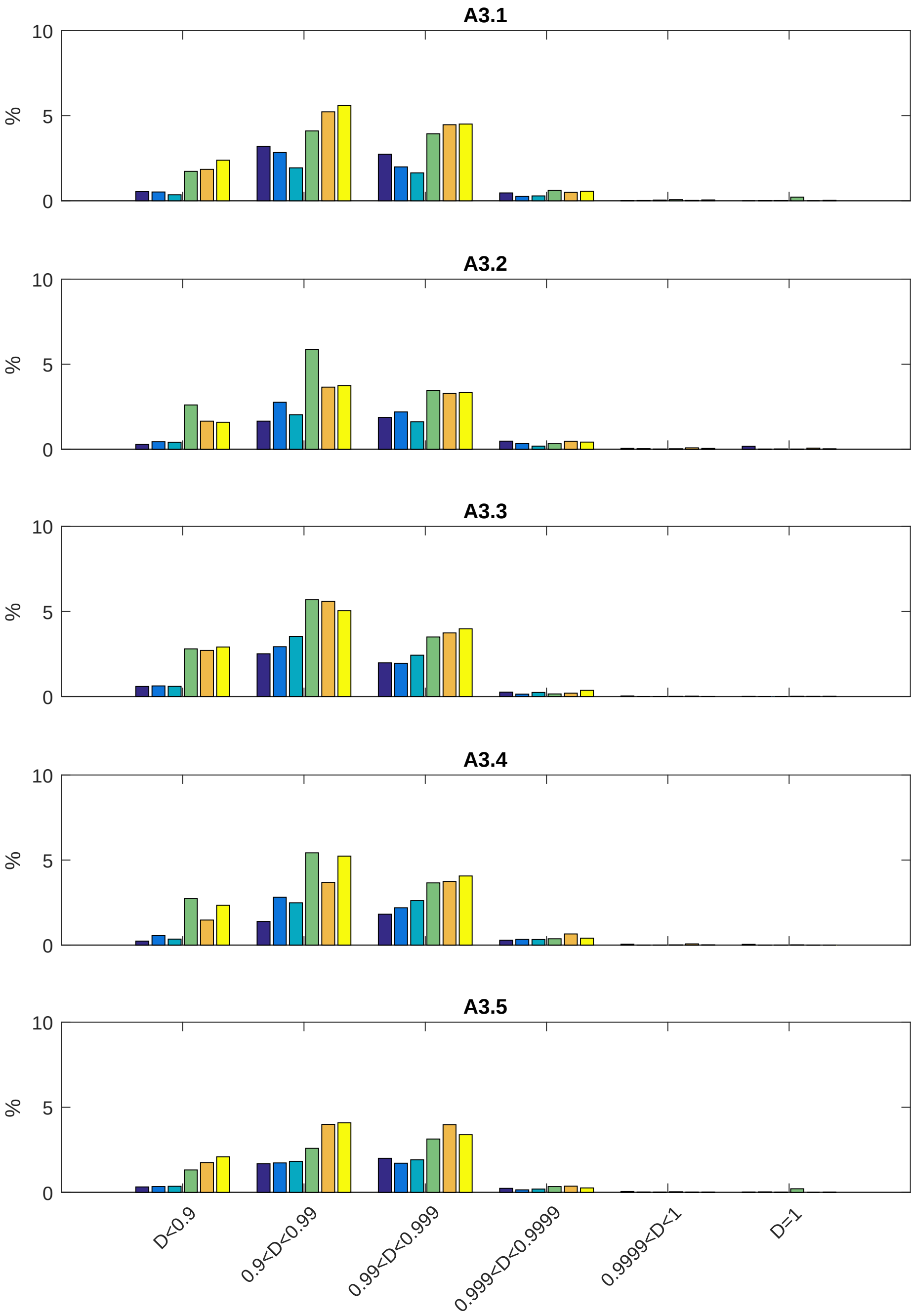

Figure 5-9: A3 SDEG Distribution

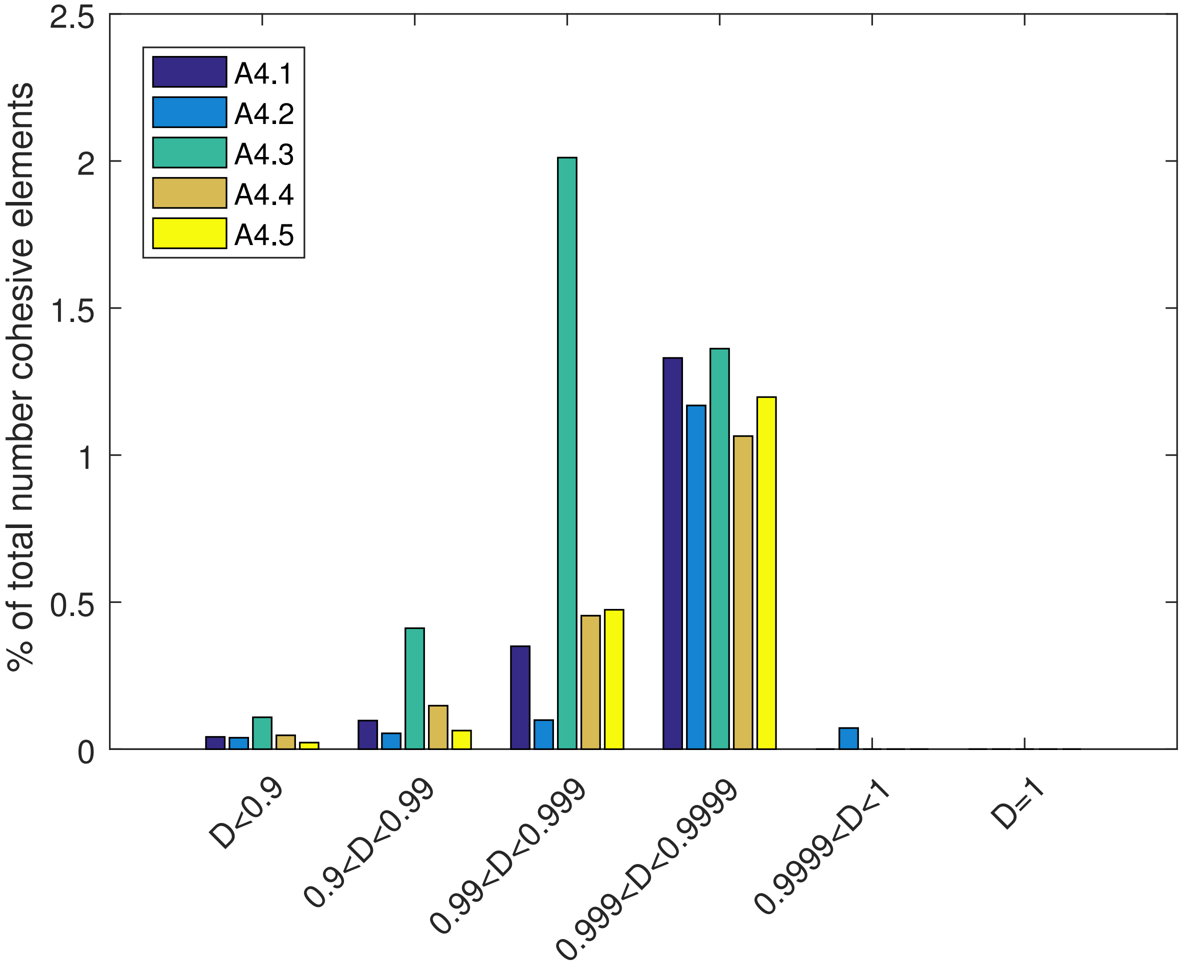

Figure 5-10: A4 SDEG distribution

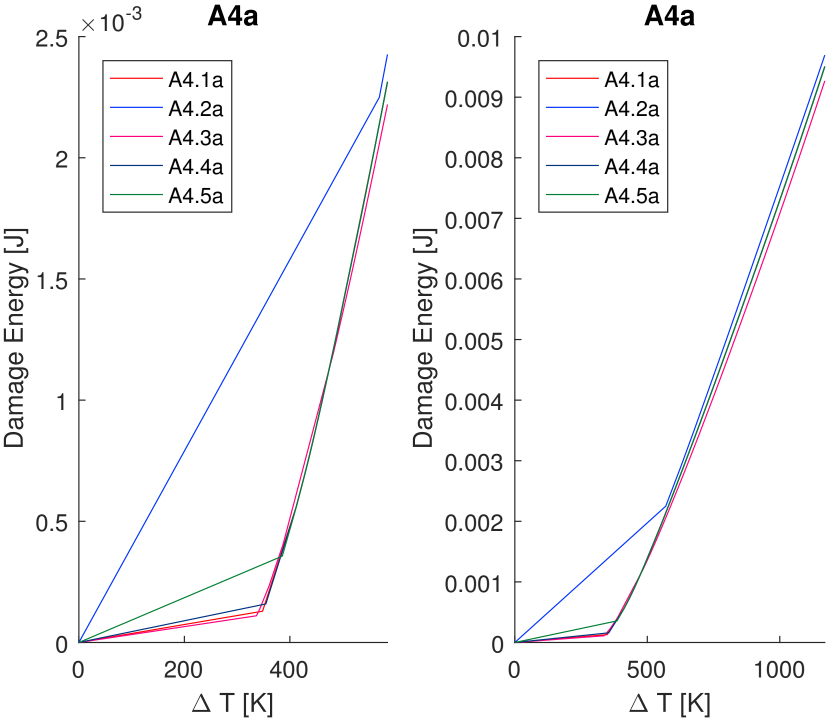

Figure 5-11a: **A4**a Damage Dissipation Energy

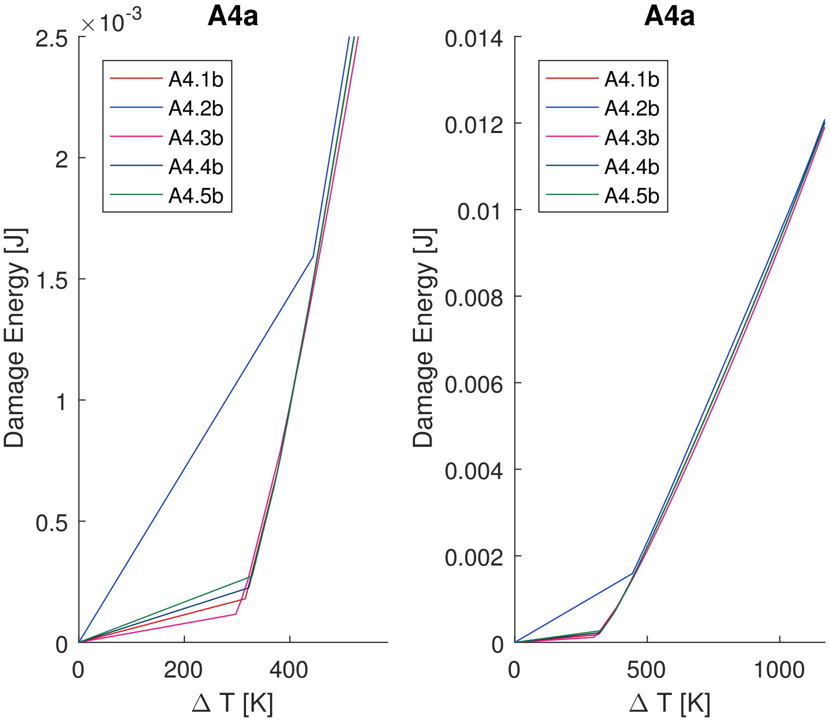

Figure 5-11b: **A4**b Damage Dissipation Energy

Chapter 6

Parametric Study B

This section outlines the results derived from Parametric Study B, which was designed to investigate the fracture behaviour of the self-healing TBC system. The geometries used in this study consisted of a heterogeneous top-coat that in addition to being comprised of contiguous lamellae units and pores, also contained circular healing particles. The healing particles were assigned the accepted material properties of $MoSi_2$.

Differences in fracture behaviour between models excluding and containing healing particles (Set A and Set B respectively) are to be expected. On one hand, damage may be exacerbated in set B since the presence of healing particles, is in addition to pores, a source of stress concentrations. Furthermore, that the healing particles are attributed a lower coefficient of expansion than YSZ, which effectively widens the mismatch between the top-coat and substrate contraction, the relative strain between the layers increases. However, since $MoSi_2$ is stiffer in comparison to YSZ, the global stiffness of the model will increase, as dictated by the rule of mixtures. Applying the rule of mixtures to estimate the resulting stiffness of the composite E_c (assuming a particle concentration of 10%) also implies an augmentation in properties, using the stiffness values of the TC E_m = 200000 MPa and particle E_p = 450000 MPa:

$$\text{(not including pores) } E_c = 0.1(450000) + 0.9(200000) = 225000$$

$$\text{(pore area fraction: 10\%) } E_c = 0.1(450000) + 0.8(200000) = 205000$$

A pore-free system experiences a 12.5% increase in global stiffness due to the presence of particles, whereas a porous sample will experience a 2.5% increase in stiffness. A cursory overview of the results derived from this study show that using the same loading conditions, self-healing materials in general show more fracture resistance than the traditional TBC samples exemplified by the models comprising Study A. Since considerably less (and in many cases, none) cohesive elements exceed the D_{thres}value of 0.9999 used in the post-processing of Study A, the D_{thres} was lowered to 0.9995 for the post-processing of B results.

The purpose of Parametric Study B was to discern the influence of healing particles on crack growth and trajectories, and to differentiate this behavior with that observed from Parametric Study A results. As was the case for Study A, the desired objective from the analyses is to find ways of controlling the fracture properties of the global system by fine-tuning the microstructure. The section first outlines the results derived from the three branches that constitute Study B. B1 studies the interaction between lamellae and healing particles by keeping the particle distribution constant, but changing the lamellae morphology. B2, analogous to A3, is comprised of 5 sets of 6 trials, with each set using varying healing particle dimensions and volume percentage. B3, which consists of two sets of 3 trials, studies the effect of the size of healing particles by keeping the particle positions constant but changing their radii.

6-1 B1

Parametric Study B1 consisted of six trials in which the pore and healing particle distribution are kept constant, while the lamellae morphology is varied. In some noticeable ways, the results from B1 are reflective of the results from A2, since both studies show that a model will contain regions of damage-sensitivity, which are shown to be influenced by subtle variations in its immediate vicinity. One of the most striking observation that can be taken from observing the crack patterns, shown in Figure 6-2, is that the TGO crack that grows into the TC in the monolithic model (B2.6) is actually suppressed in all the other models, with the exception of the thin lamellae representation (B2.5). Upon closer inspection, it can be seen that the damage in B2.1, B2.2 and B2.4, which produce more than B2.6, as is evident by Figure 6-1, accumulate fracture on other positions n the TGO. From this particular morphology, it can be inferred that healing particles suppress crack growth at the TGO, since the secondary cracks appear to be deflecting away from them. in the case of A2, it is shown that while damage appears to nucleate in the same regions in all of the trials, the propagation of the crack is definitively driven partially by particle distribution.

In corroboration with the previous results, it is shown that B1.3 model with the shortest lamellae length exhibited the most damage resilience, and interestingly, more so than the monolithic model (B1.6). When examining the crack patterns, it can be observed that TGO failure is induced by larger lamellae.

6-2 B2

Parametric Study B2 tested the effect of healing particle dimensions and distributions assuming constant average lamellae dimensions. One of the most striking features immediately evident from the B2 results is that the presence of healing particles- at all concentrations and sizes- induces damage on the TGO peaks. Despite having a more a irregular stress field and hence more opportunity for high stress concentration, results from B2 in general (a) show more consistent behaviour between trials and (b) have less cumulative crack areas that the TBC counterparts. The homogeneous response from all the models is illustrated in the SDEG distribution graph presented in Figure 6-4. As is evident in Figure 6-3 with the exception of one outlier in the B2.5 set and two in the B2.2 set, most models show stable crack behaviour

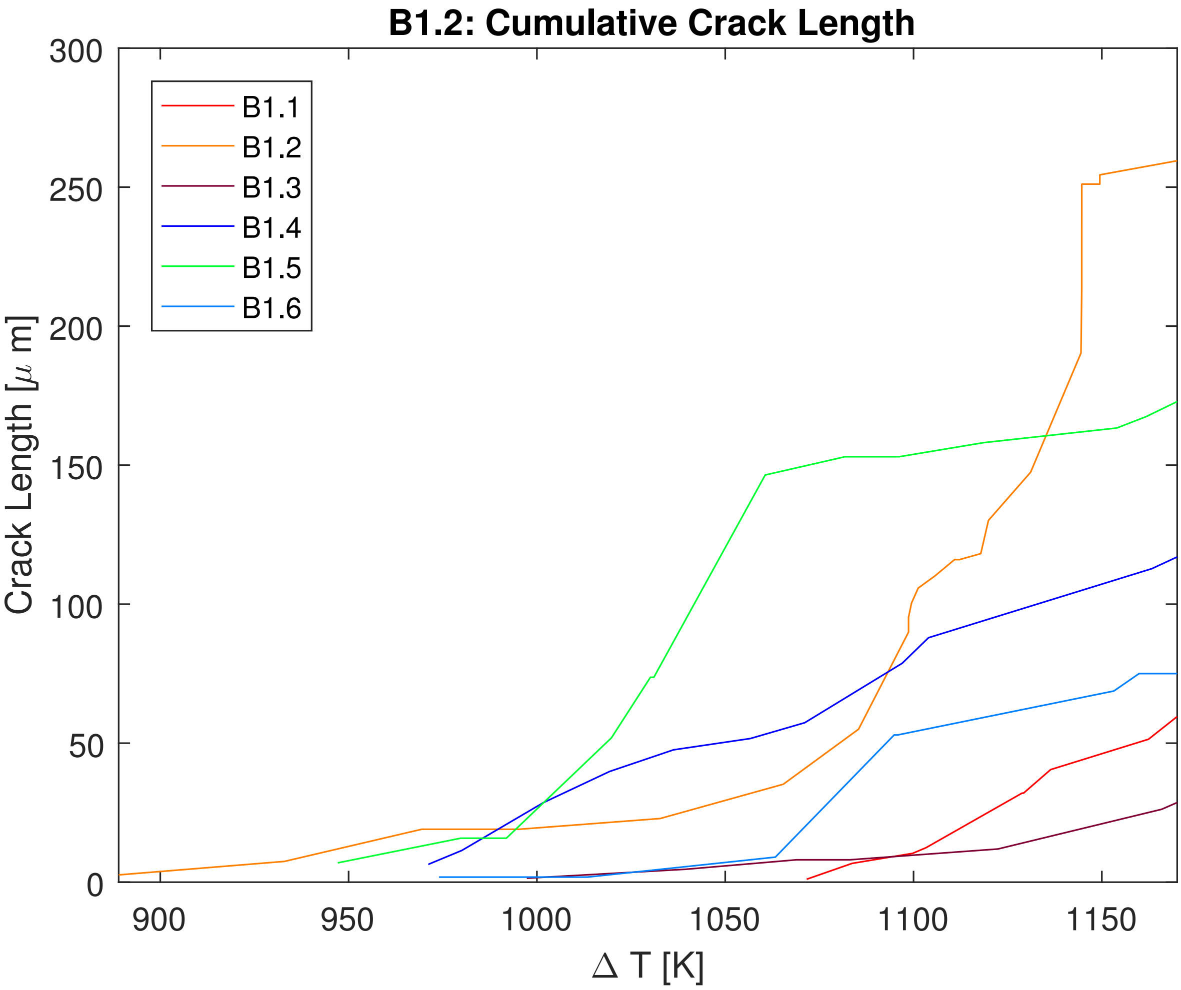

Figure 6-1: B1 Crack Growth

that remains under 100 μm. For a comparison, on average the crack lengths derived in Study A were 200 μm in length, with many more outliers that exceed this value. It should be noted that these lengths were computed using a lower damage threshold value as well. This may be due to the fact that the elliptical pores, which cause considerably higher stress concentrations in the solution space than the particles, are further away from the TC/TGO interface closer to the surface due to the presence of particles at the lower half of the domain. Another counter-intuitive observation is that model B2.5, which tested the effect of a lower healing particle volume, had the highest variability in fracture behaviour.

Several qualitative observations can be produced by examining the crack patterns extracted from the analyses. The crack patterns for sub-study B2 are included in the appendix of this report. Analogous to the results in derived from A2, the results show that cracks do deflect towards healing particles (i.e B2.2c, B2.3c and B2.4c) much in the same way cracks deflect towards pores. However, examining the crack pattern derived from O3.1a, crack trajectories that are tearing through the domain are not necessarily influenced by particle presence. However, higher degrees of clustering does fracture to the same degree that clusters of pores do. Furthermore, particles located in the proximity of the TC/TGO interface at a

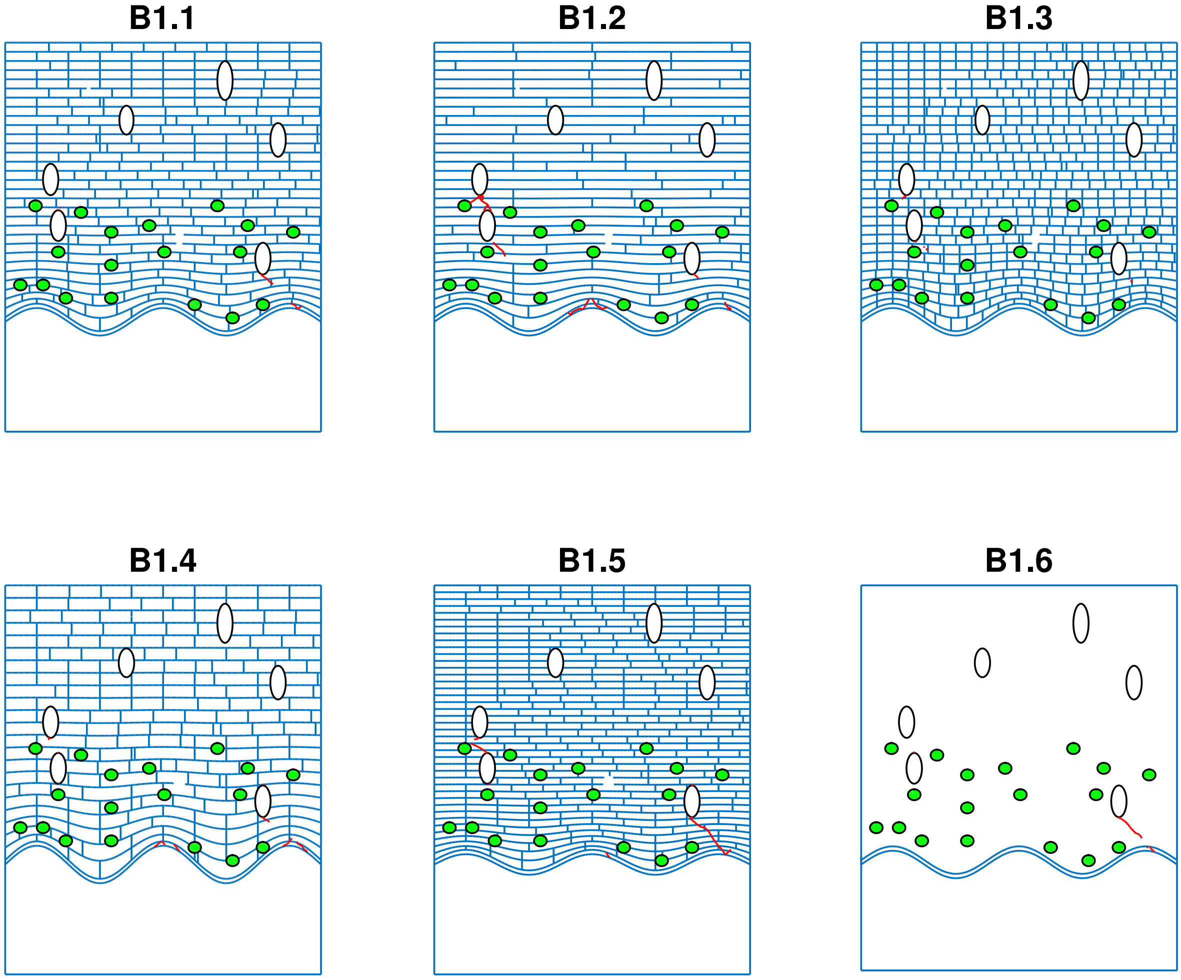

Figure 6-2: **B1** Crack Patterns

45 degree angle from the peaks do attract cracks that initiate at the interface. However, the attraction between cracks initiated at the TGO and at the particle is not as strong as between interface cracks and pores.Particles are also a susceptible for being sites of crack initiation (B2.2b).

6-3 B3

Parametric Study B3 consisted of two sets of three trials. All trials comprised of geometries characterized by the same pore distribution and particulate distribution, as well general lamellae properties. The sizes of the particles are adjusted in each trial, while the particle positions are maintained. Set B3a consisted of contiguous top-coats, whereas B3b trials contained a homogeneous top-coat. As can be inferred clearly from Figures 6-5 and 6-6, larger particles induce higher amounts of damage than smaller particles. Analogous to the results derived in A1, varying size appears to bring about a quantifiable shift in the system response. The consistent shifts displayed by the crack length against load increment curves in response to using lamellae and using larger particles suggests that a Monte Carlo analysis will yield valuable information on general particle size and damage relations. The results imply that the size of the healing particle and total damage experienced by the model may be tied by a scalar relation.

6-4 Discussion

Parametric Study B was developed to test the fracture behaviour of TBC systems embedded with self-healing particles. Set B1 studied the interaction between the healing particles, lamellae and pores, and revealed that the presence of healing particles suppresses crack growth and propagation. While discernible stress concentrations occur when the particles are situated near the TC/TGO interface, this results in significantly less damage than pores placed in the same position. All in all, the results from B1 echo the insights taken from Sets A2, A3 and A4, suggesting that finer lamellae results in higher fracture resistance. Study A2 examined the effect of varying the pores and particles. The variation in crack behaviour exhibited by all subsets imply that fracture behaviour cannot be generalized assuming arbitrary morphologies, and that the placement of pores and particles are significant aspects of fracture behaviour. However, the crack behaviour observed in this extensive set showed more consistency than set A3, which similarly tested fracture behaviour against constant lamellae dimensions but arbitrary morphologies. Two of the three outliers in terms of total crack length were both trials in B2.2, which modeled fracture behaviour of TCs embedded with larger particles. This observation find unequivocal agreement with the results garnered in Study B3, which fixes the placement of particles and varies size. Another point to note is that the results from this study are not aligned with the results shown from crack behaviour in a single-inclusion geometry. The fracture map that was developed by varying the elastic modulus, toughness and strength ratios of the inclusion and matrix imply that the composite system observed in this thesis would encourage crack fracture. This study seems to imply otherwise, though it must be noted that the Ponnusami's study involved simple Mode I loading and symmetric geometry , while this study involves mixed-mode loading and random geometry.

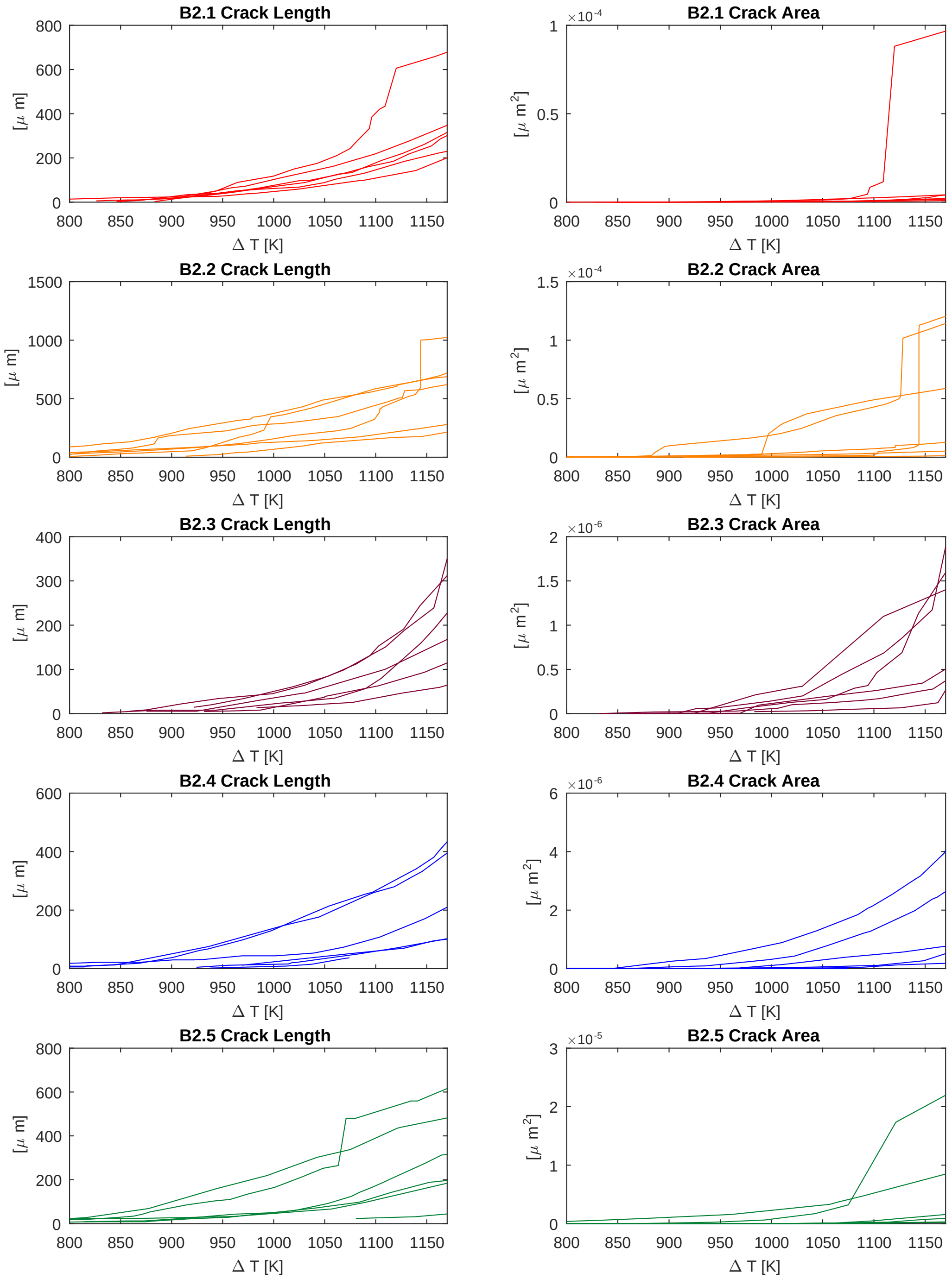

Figure 6-3: B2 Crack Lengths

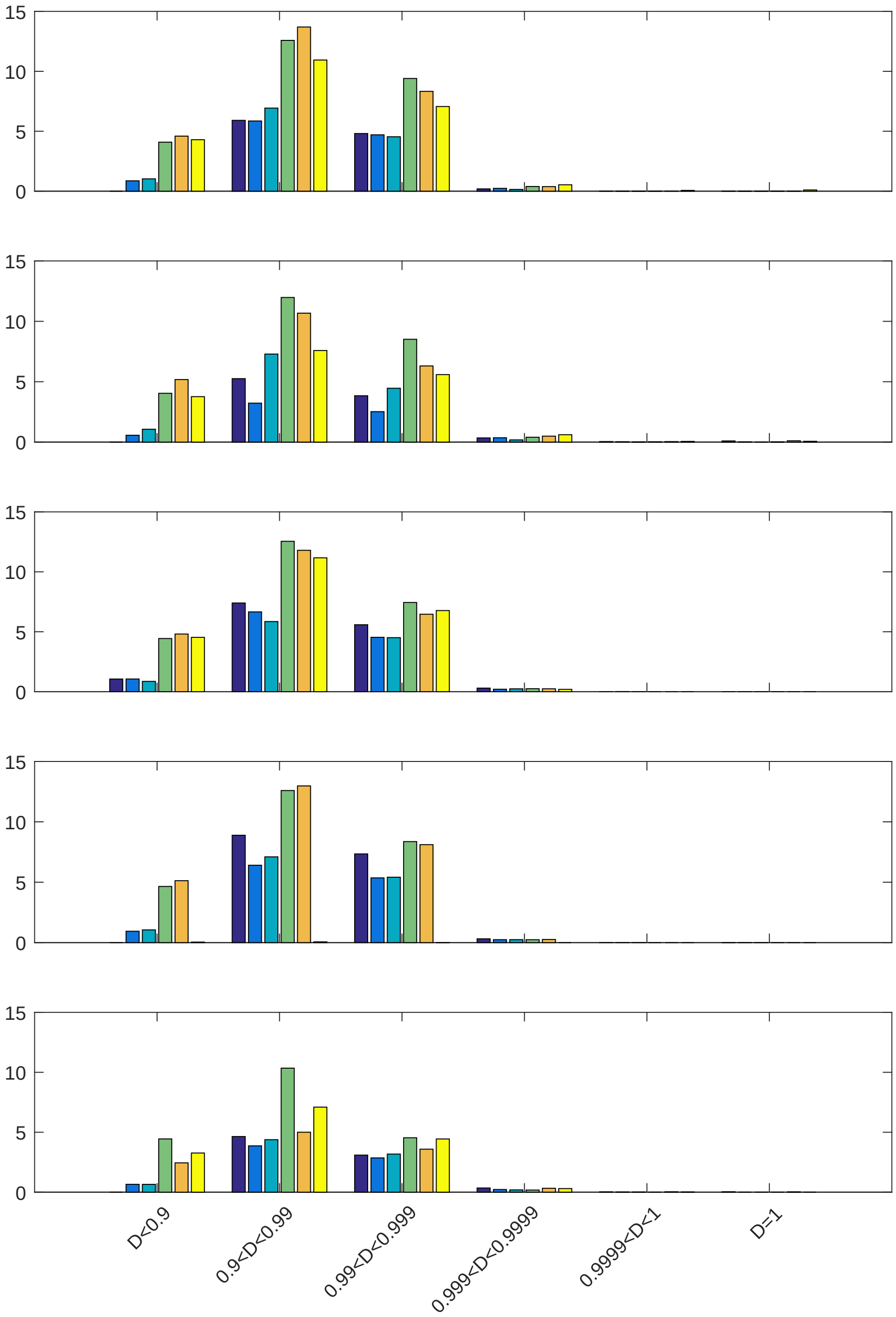

Figure 6-4: B2 SDEG Distribution

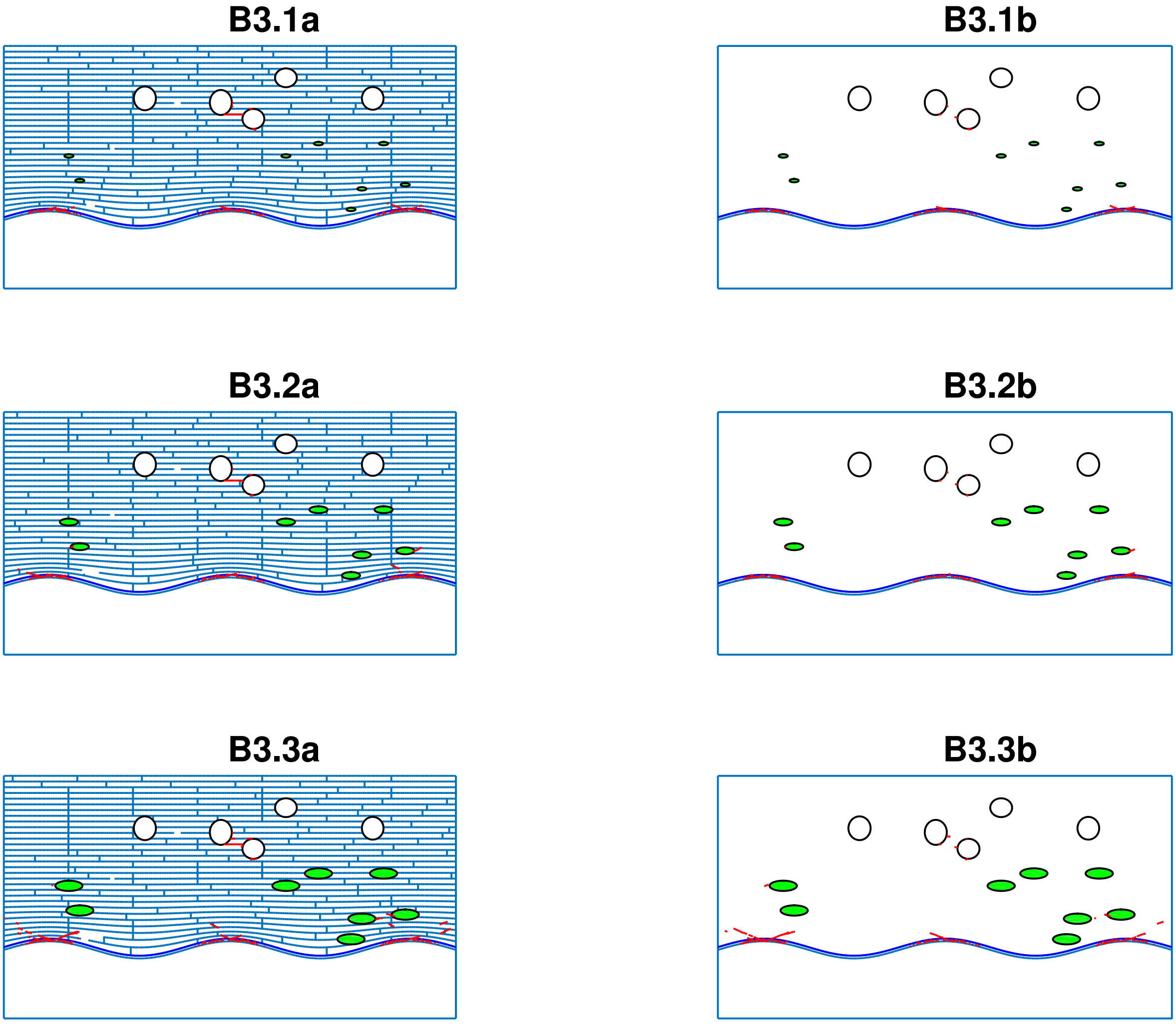

Figure 6-5: **B3** Crack Patterns

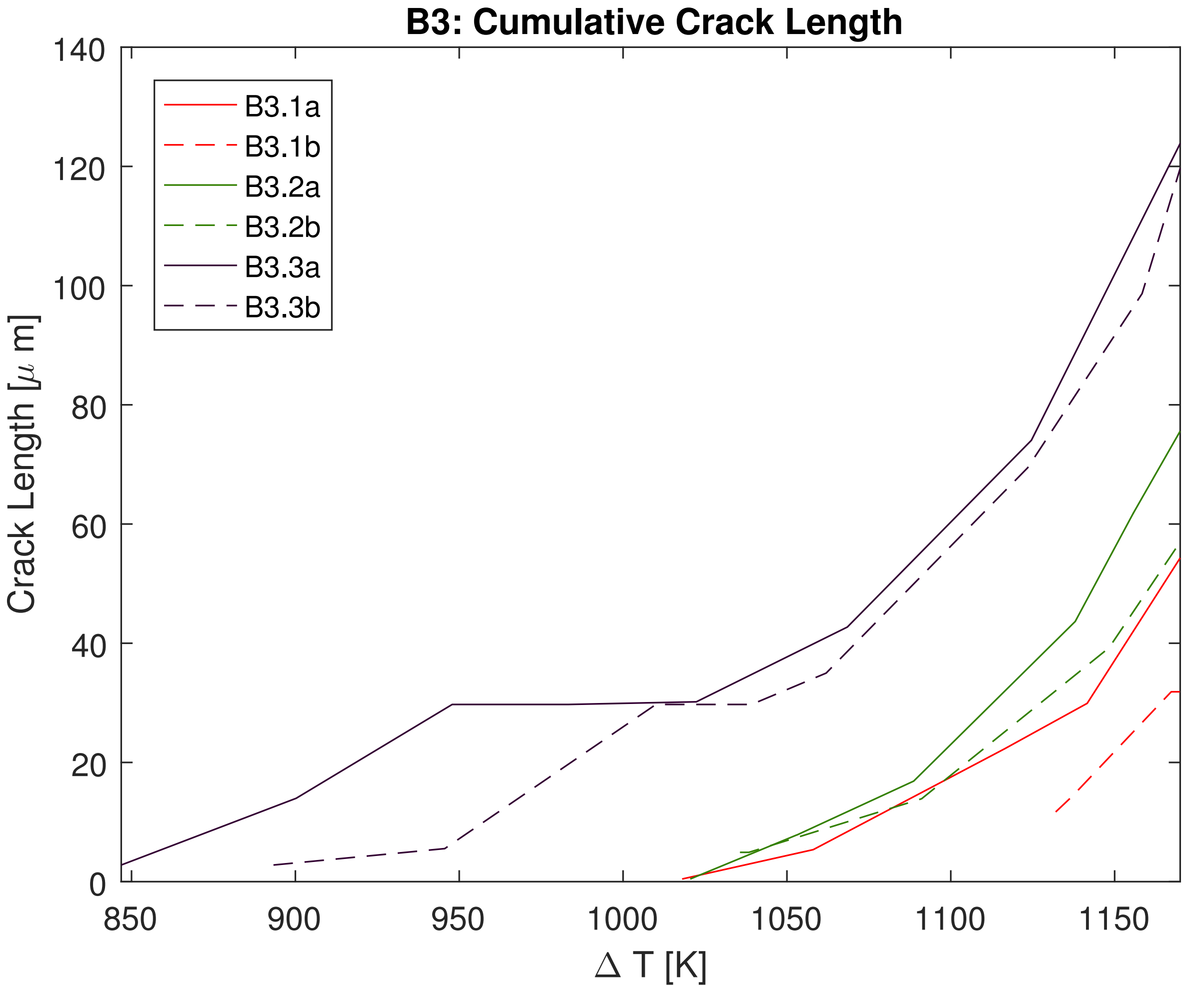

Figure 6-6: B3 Crack Length

Chapter 7

Conclusion

The TBC microstructure optimization study conducted in this thesis utilized CZM in conjunction with a thermo-mechanical FEM analysis to elucidate upon fracture behaviour in TBCs with top-coats containing contiguous lamellae structures and individuated inclusions and pores. The FEM geometry, which represented a randomized two-dimensional projection of the TC, TGO and BC, was meshed and embedded with zero-thickness cohesive elements. The model is the subjected to a cooling-down cycle, which is typical of many experiments involving TBCs and operational conditions in common applications such as the temperature exposure experienced by air-turbines. Crack patterns, SDEG distributions and crack-growth over load increment were derived from the FEM solution and used to evaluate each set of parameters. The first study, Set A, focused on the effect of the fracture properties and physical dimensions of lamellae. The explicit representation of the lamellae was a novel aspect of the study conducted, as structures and materials that can have comparable grain-like microstructures are typically idealized as a homogeneous component. Study A yielded the following results:

- Lamellae strength properties and damage energy dissipation show an inverse power relation.
- Studies examining the effect of the physical dimensions of lamellae suggest that finer lamellae contribute to more fracture-resistant microstructures
- Fracture paths are highly dependent on the relative placement of the pores to each other as well as the TC/TGO interface. Fracture behaviour is effected more by the pore distribution than it is by the lamellae morphology.

As explicated in Section 2-2-2, microstructures tailored to specific properties can by achieved by adjusting the plasma-spraying processing parameters. As mentioned before, the lamellae interface properties can be augmented by increasing the plasma power and spray distance. In addition to this, it is noteworthy to consider that the relationship between finer lamellae and higher durability has been demonstrated through experiment by Bai (Bai et al., 2011). Conventional coarse morphologies characteristic of conventional APS-TBCs and fine morphology observed in supersonic APS were compared, and it was found that the latter performed better when subjected to thermal cycling.

This study was followed by Set B, which studied a recently developed variant of TBCs that are embedded with healing particles included to prolong the lifetime of the TBC. The results gained from Set A is as follows:

- Healing particles increases the fracture resistance of the system as a whole.
- Larger Particles induce more damage.
- Crack deflection due to an inclusion does not occur in the same manner in response to mixed moding conditions as it does in Mode I condition.

The unequivocal positive relation between size of the particles used and the amount of damage caused introduces an interesting critique on current analytical models concerning stress fields around inclusions. Established fracture theory, such as the stress concentrations surrounding circular holes and Eshelby's tensors for inclusions, are both non-dimensional i.e the solution is independent of the feature's dimensions. This statement also applies to the heuristic relations reproduced in Chapter 2-1-2 The results, as dictated by CZM, appear to contradict these theories.

In addition to these qualitative observations, a strong potential for the future development of quantitative relations between model variables have been identified:

- The power in the power function that characterizes the damage energy dissipated with load increment increases with decreasing lamellae strength properties.
- The crack length over load increment shifts forward when the lamellae properties are increased.
- The crack length over load increment shifts forward and lower when smaller particles are used in self-healing samples.

A statistical analysis using many morphologies can be used to determine a scalable relation between property and fracture behaviour. While the tests in this study produced consistent results with easily discernable patterns, the different trials produced a range of response values that cannot be meaningfully averaged.

The insight gained from the study can be made more holistic by considering the effect of the microstructure on the thermal conductance. This is important because functionally, TBCs ideally have low thermal conductances. However, characteristics such as high porosity attributed to high thermal conductance have a detrimental effect on the durability. Furthermore, the thermo-mechanical behaviour is in many way informed by the thermal conductance of the system, and vice versa, engendering a feedback loop that propagates with every thermal cycle. As revealed by preliminary studies O2 and O3, the model response is sensitive to the initial temperature distribution.

In order to make longer-range predictions of TBC durability, a heating-up cycle should also be included to produce a more complete picture of TBC fracture behaviour subjected to thermal cycles. Damage until spallation in TBCs can be categorized as a thermal fatigue-load. In addition to this, swelling elements can be used at the TGO to simulate TGO growth, which along with the substrate-TBC thermal mismatch, is the other main driving mechanism of failure in TBCs.

Due to the fact that fracture growth in grain-like microstructures are limited in number, the random microstructure generator can be used to produce a set of simpler geometries subjected to simpler loadings, such as a pure tension load. Because the both the geometry and loading case used in this thesis were complex, each variable could not easily be uncoupled from the others. Therefore, a simpler set-up would help yield more definite sets of rules that would help further the field of fracture mechanics from a more generalized perspective.

Bibliography

Ahlquist, C. N. (1975). On the Interaction of Cleavage Cracks with Second Phase Particles. *Acta Metallurgica*.

Ahrens, M., Lampenscherf, S., Vaßen, R., & Stöver, D. (2004). Sintering and Creep Processes in Plasma-Sprayed Thermal Barrier Coatings. *Journal of Thermal Spray Technologiy*, *13*(September), 432–442. doi: 10.1361/10599630420434

Al-Athel, K., Loeffel, K., Liu, H., & Anand, L. (2013). Modeling decohesion of a top-coat from a thermally-growing oxide in a thermal barrier coating. *Surface and Coatings Technology*, *222*, 68–78. Retrieved from `http://dx.doi.org/10.1016/j.surfcoat.2013.02.005` doi: 10.1016/j.surfcoat.2013.02.005

Aliha, M. R. M., & Saghafi, H. (2013). The effects of thickness and Poisson ' s ratio on 3D mixed-mode fracture. *Engineering Fracture Mechanics*, *98*, 15–28. Retrieved from `http://dx.doi.org/10.1016/j.engfracmech.2012.11.003` doi: 10.1016/j.engfracmech.2012.11.003

Ando, K., Kodama, S., Yokouchi, M., Lee, S.-K., Nakao, W., & Takahashi, K. (1999). Self-Crack-Heling Behavior and Fracture Strength of Al 2 O 3 / Sic Composites At the High. In *Ecf15.*

Arai, M., Okajima, Y., & Kishimoto, K. (2007). Mixed-mode interfacial fracture toughness for thermal barrier coating. *Engineering Fracture Mechanics*, *74*, 2055–2069. doi: 10.1016/j.engfracmech.2006.10.021

Bai, Y., Han, Z. H., Li, H. Q., Xu, C., Xu, Y. L., Ding, C. H., & Yang, J. F. (2011). Structure-property differences between supersonic and conventional atmospheric plasma sprayed zirconia thermal barrier coatings. *Surface & Coatings Technology*, *205*, 3833–3839. doi: 10.1016/j.surfcoat.2011.01.056

Bäker, M. (2014). Influence of material models on the stress state in thermal barrier coating simulations. *Surface and Coatings Technology*, *240*, 301–310. Retrieved from `http://dx.doi.org/10.1016/j.surfcoat.2013.12.045` doi: 10.1016/j.surfcoat.2013.12.045

Becher, P. F., Hsueh, C.-H., Angelini, P., & Tiegs, T. N. (1988). Toughening Behavior in Whisker-Reinforced Ceramic Matrix Composites. *Journal of the American Ceramic Society*, *71*(12), 1050–1061. Retrieved from `http://onlinelibrary.wiley.com/doi/`

`10.1111/j.1151-2916.1988.tb05791.x/abstract` doi: 10.1111/j.1151-2916.1988.tb05791.x

Bednarz, P. (2006). *Finite Element Simulation of Stress Evolution in Thermal Barrier Coating Systems* (Unpublished doctoral dissertation). Research Centre Juelich.

Carabat, A. L., Zwaag, S. V. D., & Sloof, W. G. (2015). Creating a Protective Shell for Reactive MoSi 2 Particles in High-Temperature Ceramics. *The American Ceramic Society*, *2616*(35874), 2609–2616. doi: 10.1111/jace.13625

Chawla, K. K. (1998). *Ceramic Matrix Composites.* New York: Springer Science and Business Media New York.

Choi, S. R., Zhu, D., & Miller, R. A. (2005). Fracture behavior under mixed-mode loading of ceramic plasma-sprayed thermal barrier coatings at ambient and elevated temperatures. *Engineering Fracture Mechanics*, *72*, 2144–2158. doi: 10.1016/j.engfracmech.2005.01.010

Cluzel, C., Baranger, E., Ladevèze, P., & Mouret, A. (2009). Mechanical behaviour and lifetime modelling of self-healing ceramic-matrix composites subjected to thermomechanical loading in air. *Composites Part A: Applied Science and Manufacturing*, *40*(8), 976–984. Retrieved from `http://dx.doi.org/10.1016/j.compositesa.2008.10.020` doi: 10.1016/j.compositesa.2008.10.020

Cutler, R. A., & Virkar, A. V. (1985). The effect of binder thickness and residual stresses on the fracture toughness of cemented carbides. *Journal of Materials Science*, *20*(10), 3557–3573. doi: 10.1007/BF01113762

Czech, N., Mallener, W., Stamm, W., & Stover, D. (2001). Influence of impurity content and porosity of plasma-sprayed yttria-stabilized zirconia layers on the sintering behaviour. *Surface and Coatings Technology*, *141*, 135–140.

Evans, A. G., He, M. Y., & Hutchinson, J. W. (2001). Mechanics-based scaling laws for the durability of thermal barrier coatings. *Progress in Materials Science*, *46*(3-4), 249–271. doi: 10.1016/S0079-6425(00)00007-4

Genet, M., Marcin, L., Baranger, E., Cluzel, C., Ladevèze, P., & Mouret, A. (2012). Computational prediction of the lifetime of self-healing CMC structures. *Composites Part A: Applied Science and Manufacturing*, *43*(2), 294–303. Retrieved from `http://dx.doi.org/10.1016/j.compositesa.2011.11.004` doi: 10.1016/j.compositesa.2011.11.004

Gilbert, C., Dauskardt, R., & Ritchie, R. (1997). Microstructural mechanisms of cyclic fatigue-crack propagation in grain-bridging ceramics. *Ceramics International*, *23*(5), 413–418. doi: 10.1016/S0272-8842(96)00048-X

Green, D. J. (1981). Stress-Induced Microcracking at Second-Phase Inclusions. *Journal of the American Ceramic Society*, *64*(3), 138–141. Retrieved from `http://onlinelibrary.wiley.com/doi/10.1111/j.1151-2916.1981.tb10244.x/abstract$\delimiter"026E30F$nhttp://doi.wiley.com/10.1111/j.1151-2916.1981.tb10244.x` doi: 10.1111/j.1151-2916.1981.tb10244.x

Guo, H. B., Vaßen, R., & Sto, D. (2005). Thermophysical properties and thermal cycling behavior of plasma sprayed thick thermal barrier coatings. , *192*, 48–56. doi: 10.1016/j.surfcoat.2004.02.004

Guo, H. B., Vaßen, R., & Stöver, D. (2004). Atmospheric plasma sprayed thick thermal barrier coatings with high segmentation crack density. *Surface and Coatings Technology*, *186*(3), 353–363. doi: 10.1016/j.surfcoat.2004.01.002

Hille, T. S. (2009). *Lifetime Modeling of Thermal Barrier Coatings* (Unpublished doctoral dissertation). Technische Universiteit Delft.

Hillig, W. B. (1987). Strength and Toughness of Ceramic Matrix Composites. *Annual Review of Material Science*(17), 341–383. doi: 10.1039/c3nr00651d

Jian, C. Y. (2016). Determination of Interface Barrier Coating System. *ASME Journal of Applied Mechanics*, *125*(April 2003), 176–182. doi: 10.1115/1.1555658

Joulia, A., Bolelli, G., Gualtieri, E., Lusvarghi, L., Valeri, S., Vardelle, M., … Vardelle, A. (2014). Comparing the deposition mechanisms in suspension plasma spray (SPS) and solution precursor plasma spray (SPPS) deposition of yttria-stabilised zirconia (YSZ). *Journal of the European Ceramic Society*, *34*(15), 3925–3940. Retrieved from `http://dx.doi.org/10.1016/j.jeurceramsoc.2014.05.024` doi: 10.1016/j.jeurceramsoc.2014.05.024

Karger, M., Vaßen, R., & Stöver, D. (2011). Surface & Coatings Technology Atmospheric plasma sprayed thermal barrier coatings with high segmentation crack densities : Spraying process , microstructure and thermal cycling behavior. *Surface & Coatings Technology*, *206*(1), 16–23. Retrieved from `http://dx.doi.org/10.1016/j.surfcoat.2011.06.032` doi: 10.1016/j.surfcoat.2011.06.032

Kulczyk-Malecka, J., Zhang, X., Carr, J., Carabat, A. L., Sloof, W. G., Zwaag, S. V. D., … Xiao, P. (2016). Influence of embedded MoSi2 particles on the high temperature thermal conductivity of SPS produced yttria-stabilised zirconia model thermal barrier coatings. *Surface & Coatings Technology*. Retrieved from `http://dx.doi.org/10.1016/j.surfcoat.2016.07.113` doi: 10.1016/j.surfcoat.2016.07.113

Kulkarni, A., Vaidya, A., Goland, A., Sampath, S., & Herman, H. (2003). Processing effects on porosity-property correlations in plasma sprayed yttria-stabilized zirconia coatings. *Materials Science and Engineering A*, *359*(1-2), 100–111. doi: 10.1016/S0921-5093(03)00342-3

Li, C., & Ohmori, A. (2002). Relationships Between the Microstructure and Properties of Thermally Sprayed Deposits. *Journal of Thermal Spray Technologiy*, *11*(3).

Li, C. J., Yang, G. J., & Li, C. X. (2013). Development of particle interface bonding in thermal spray coatings: A review. *Journal of Thermal Spray Technology*, *22*(2-3), 192–206. doi: 10.1007/s11666-012-9864-9

Ma, W., & Dong, H. (2011). Ceramic thermal barrier coating materials. *Thermal Barrier Coatings*, 25–52. doi: 10.1016/B978-1-84569-658-0.50002-8

Malzbender, J., Wakui, T., & Steinbrech, R. (2004). Strain Analysis of Plasma Sprayed Thermal Barrier Coatings Under Mechanical Stress. *Journal of Thermal Spray Technology*, *13*(3), 390–395. doi: 10.1361/10599630420425

Nair, B. G., Singh, J. P., & Grimsditch, M. (2004). Stress analysis in thermal barrier coatings subjected to long-term exposure in simulated turbine conditions. *Journal of Materials Science*, *39*(6), 2043–2051. doi: 10.1023/B:JMSC.0000017767.36955.5c

Nielsen, C. V., Legarth, B. N., & Niordson, C. F. (2011). Extended FEM modeling of crack paths near inclusions. *Proceedings of the 2011 American Control Conference*, *2*(March), 1885–1891. doi: 10.1002/nme

Ohji, T. (1998). Strengthening and Toughening Mechanisms of Ceramic Nanocomposites. , *60*, 1453–1460.

Omar, B. (2016). A review of T-stress calculation methods in fracture mechanics computation computation. *Nature and Technology*(July).

Pindera, M.-j., & Arnold, S. M. (2003). Analysis of Plasma-Sprayed Thermal Barrier Coatings With Homogeneous and Heterogeneous Bond Coats Under Spatially Uniform Cyclic Thermal Loading. (December).

Ponnusami, S. A., Turteltaub, S., & van der Zwaag, S. (2015). Cohesive-zone modelling of crack nucleation and propagation in particulate composites. *Engineering Fracture Mechanics*, *149*, 170–190. Retrieved from `http://dx.doi.org/10.1016/j.engfracmech.2015.09.050` doi: 10.1016/j.engfracmech.2015.09.050

Ranjbar-Far, M., Absi, J., & Mariaux, G. (2012). Finite element modeling of the different failure mechanisms of a plasma sprayed thermal barrier coatings system. *Journal of Thermal Spray Technology*, *21*(6), 1234–1244. doi: 10.1007/s11666-012-9814-6

Rice, R. W. and Pohanka, R. C. (1979). Grain-size dependence of spontaneous cracking in ceramics. *J. Am. Ceram. Soc.*, *61*, 559–563.

Ruhle, M., Evans, A. G., Mcmeeking, R. M., Charalambides, P. G., & Hutchinson, J. W. (1987). Toughening in Alumina/Zirconia. , *35*(Ii), 2701–2710.

Ruiz, M. R. (2016). *Mechanical testing and quantification of crack healing in self-healing yttria- stabilized zirconia thermal barrier coating* (Tech. Rep. No. 1).

Smith, D. J., Ayatollahi, M. R., Pavier, M. J., & A, P. R. S. (2006). On the consequences of T-stress in elastic brittle fracture On the consequences of T-stress in elastic brittle fracture. In *Proceedings of the royal society* (pp. 2415–2437). doi: 10.1098/rspa.2005.1639

Tan, Y., Longtin, J. P., Sampath, S., & Wang, H. (2009). Effect of the starting microstructure on the thermal properties of as-sprayed and thermally exposed plasma-sprayed YSZ coatings. *Journal of the American Ceramic Society*, *92*(3), 710–716. doi: 10.1111/j.1551-2916.2009.02953.x

Taya, M., Hayashi, S., Kobayashi, A. S., & Yoon, H. S. (1990). Toughening of a Particulate-Reinforced Ceramic-Matrix Composite by Thermal Residual Stress. *Journal of the American Ceramic Society*, *73*(5), 1382–1391. Retrieved from `http://dx.doi.org/10.1111/j.1151-2916.1990.tb05209.x` doi: 10.1111/j.1151-2916.1990.tb05209.x

Taylor, R., Brandon, J. R., & Morrell, P. (1992). Microstructure, composition and property relationships of plasma- sprayed thermal barrier coatings*. *Surface and Coatings Technology*, *50*(1992), 141–149.

Tsipas, S. A., & Golosnoy, I. O. (2011). Effect of substrate temperature on the microstructure and properties of thick plasma-sprayed YSZ TBCs. *Journal of the European Ceramic Society*, *31*(15), 2923–2929. Retrieved from `http://dx.doi.org/10.1016/j.jeurceramsoc.2011.07.022` doi: 10.1016/j.jeurceramsoc.2011.07.022

Wang, Z., Kulkarni, A., Deshpande, S., Nakamura, T., & Herman, H. (2003). Effects of pores and interfaces on effective properties of plasma sprayed zirconia coatings. *Acta Materialia*, *51*(18), 5319–5334. doi: 10.1016/S1359-6454(03)00390-2

Wessel, E., & Steinbech, R. W. (2002). Crack propagation in plasma-sprayed thermal barrier coatings. *Key Eng. Mater.*, *223*, 55–60. doi: 10.4028/www.scientific.net/KEM.223.55

White, S. R., Sottos, N. R., Geubelle, P. H., Moore, J. S., Kessler, M. R., Sriram, S. R., … Viswanathan, S. (2001). Autonomic healing of polymer composites. *Nature*, *409*(6822), 794–797. Retrieved from `http://www.nature.com.proxy2.library.illinois.edu/nature/journal/v409/n6822/full/409794a0.html$\delimiter"026E30F$nhttp://www.nature.com.proxy2.library.illinois.edu/nature/journal/v409/n6822/pdf/409794a0.pdf` doi: 10.1038/35057232

Williams, J. G., & Ewing, P. D. (1972). Fracture under complex stress - The angled crack problem. *International Journal of Fracture*, *26*(4), 346–351. doi: 10.1007/BF00962967

Yao, S. W., Tian, J. J., Li, C. J., Yang, G. J., & Li, C. X. (2016). Understanding the Formation of Limited Interlamellar Bonding in PlasmaSprayed Ceramic Coatings Based on the Concept of Intrinsic Bonding Temperature. *Journal of Thermal Spray Technology*, *25*(8), 1617–1630. Retrieved from `"http://dx.doi.org/10.1007/s11666-016-0464-y` doi: 10.1007/s11666-016-0464-y

Appendix A

A3 Crack Patterns

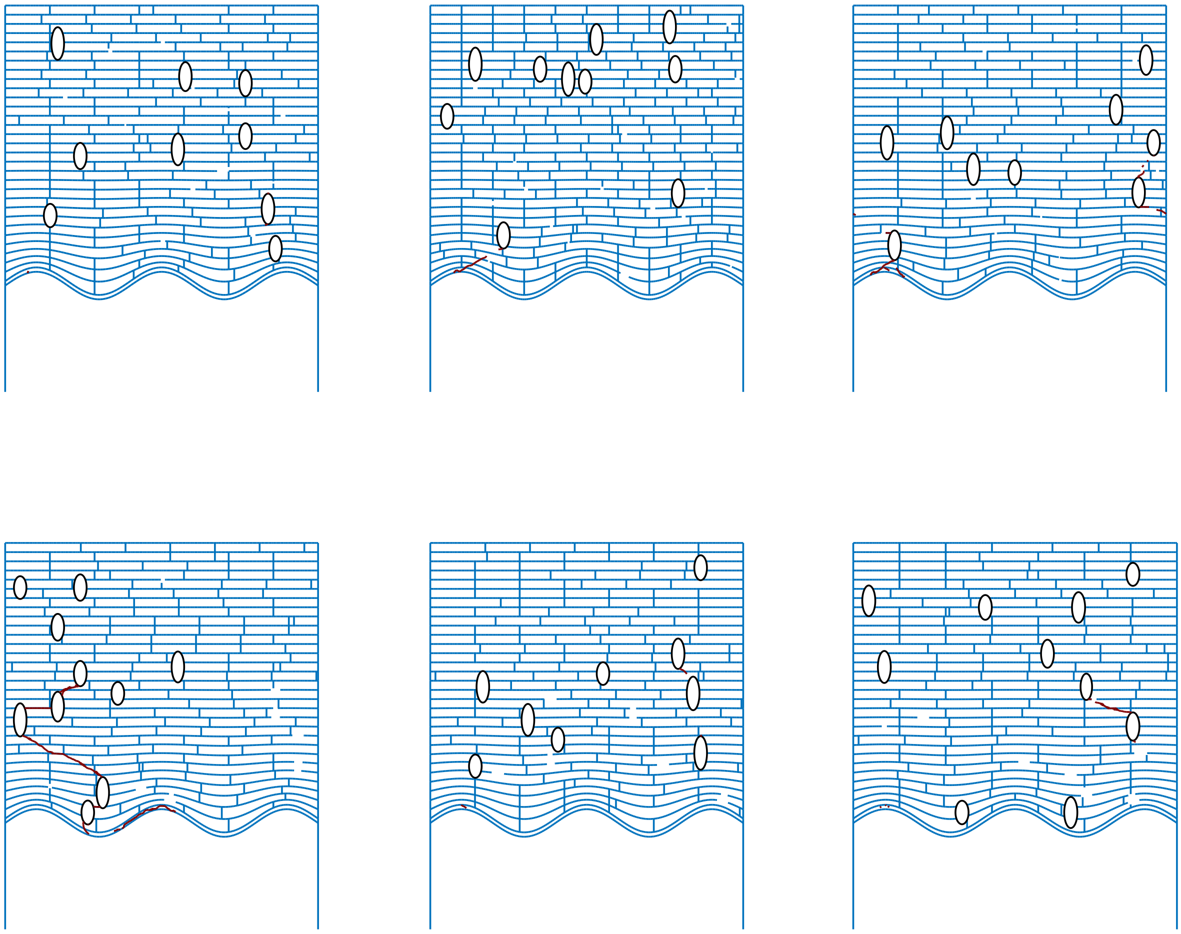

A3.1 Crack Patterns

Figure A-1: A3.1 Crack Patterns

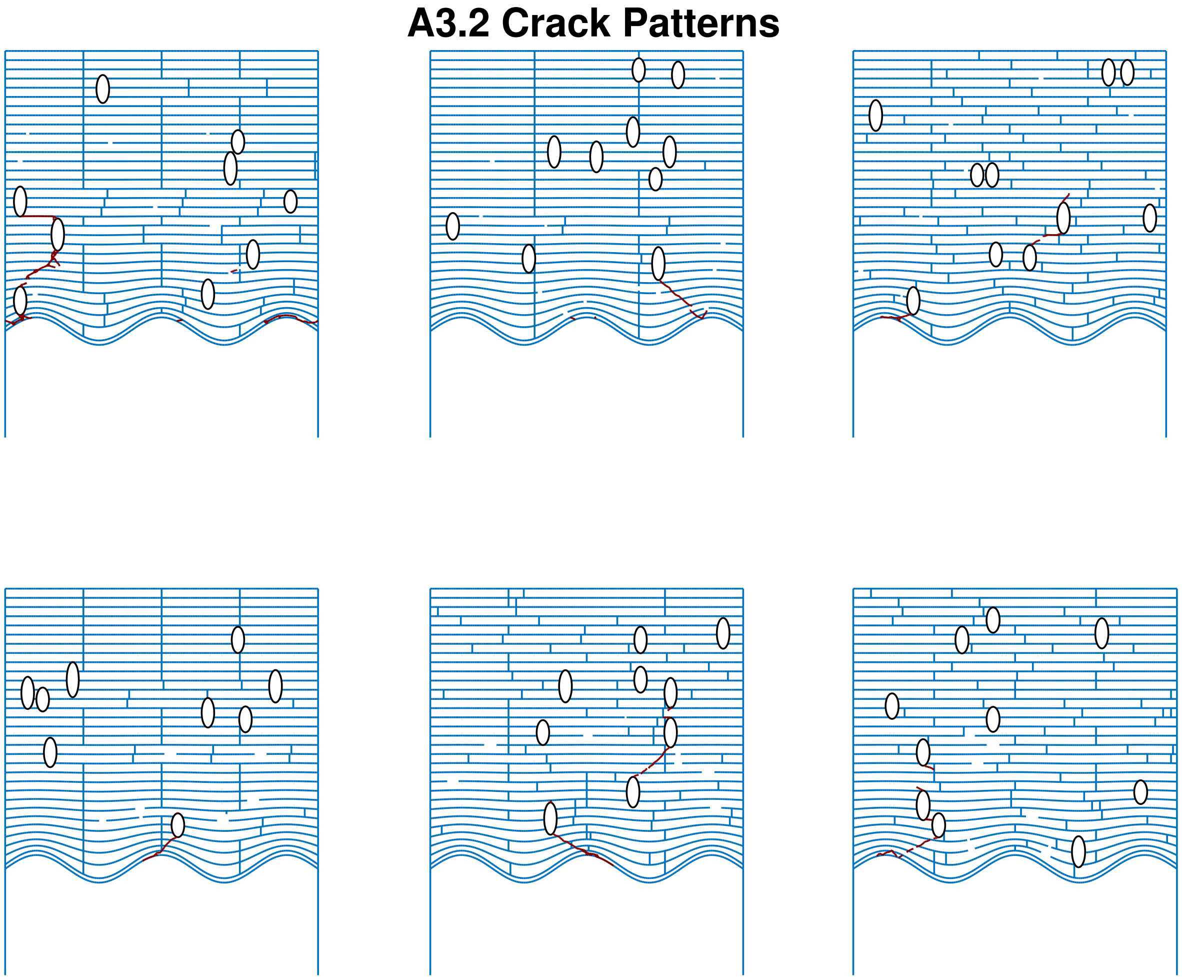

Figure A-2: A3.2 Crack Patterns

A3.3 Crack Patterns

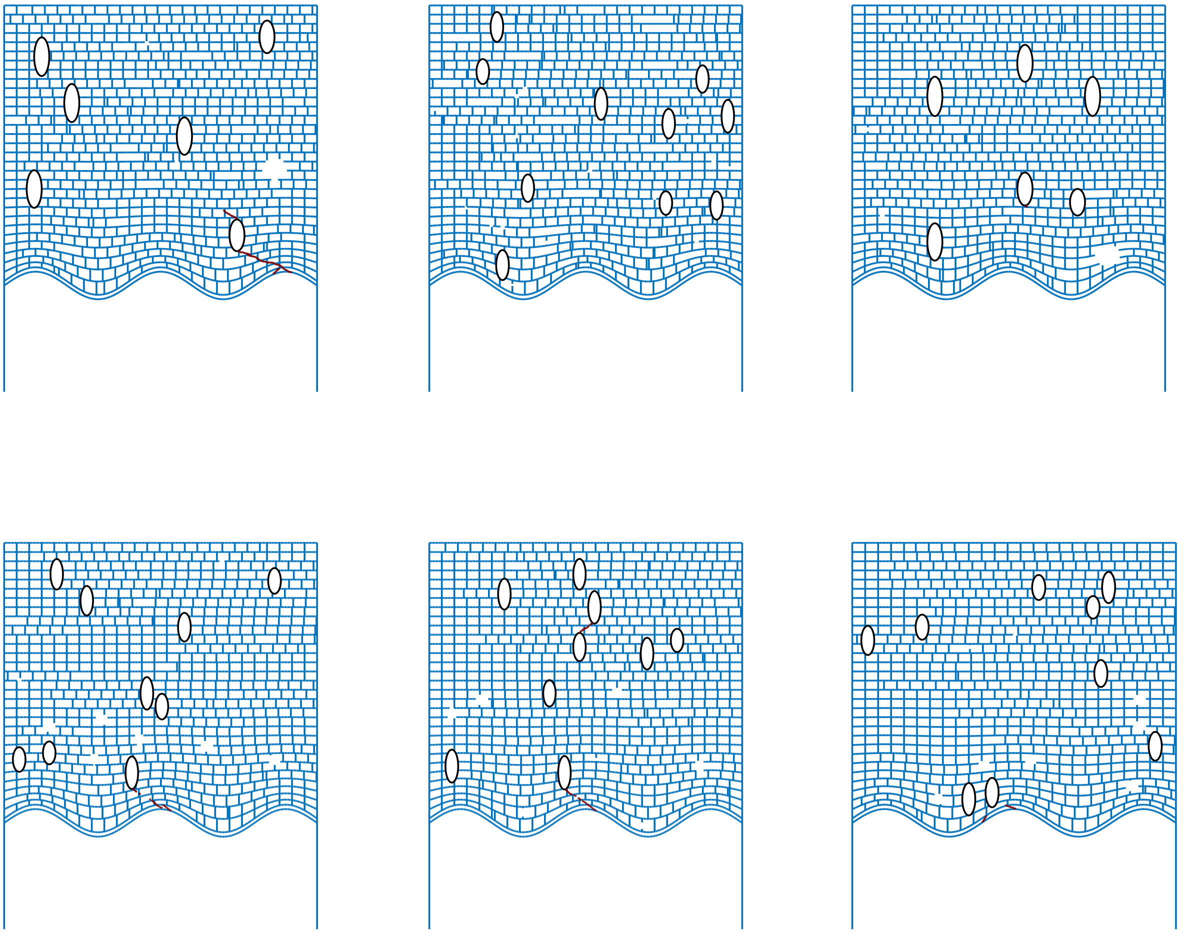

Figure A-3: A3.3 Crack Patterns

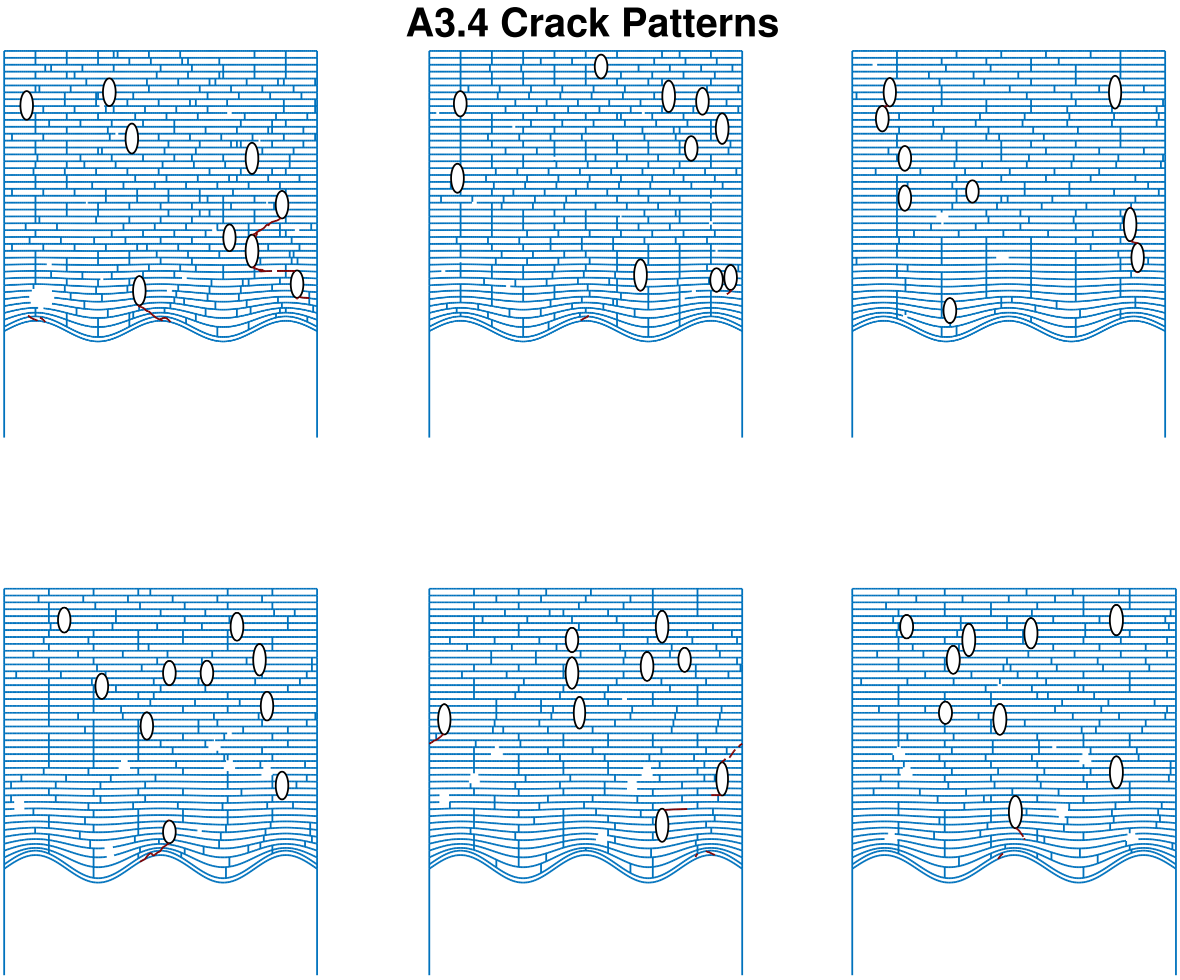

Figure A-4: **A3**.4 Crack Patterns

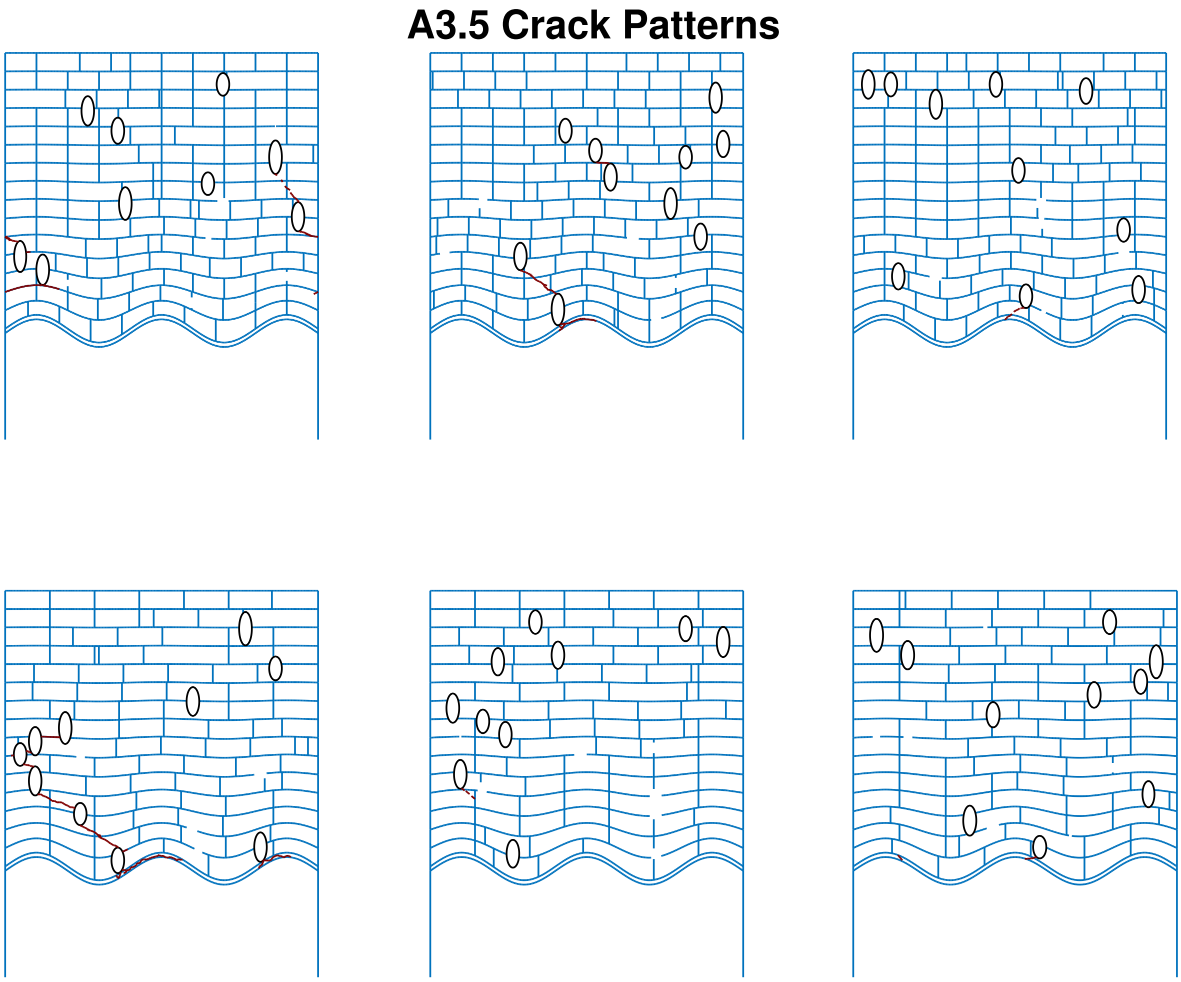

Figure A-5: **A3**.5 Crack Patterns

Appendix B

B2 Crack Patterns

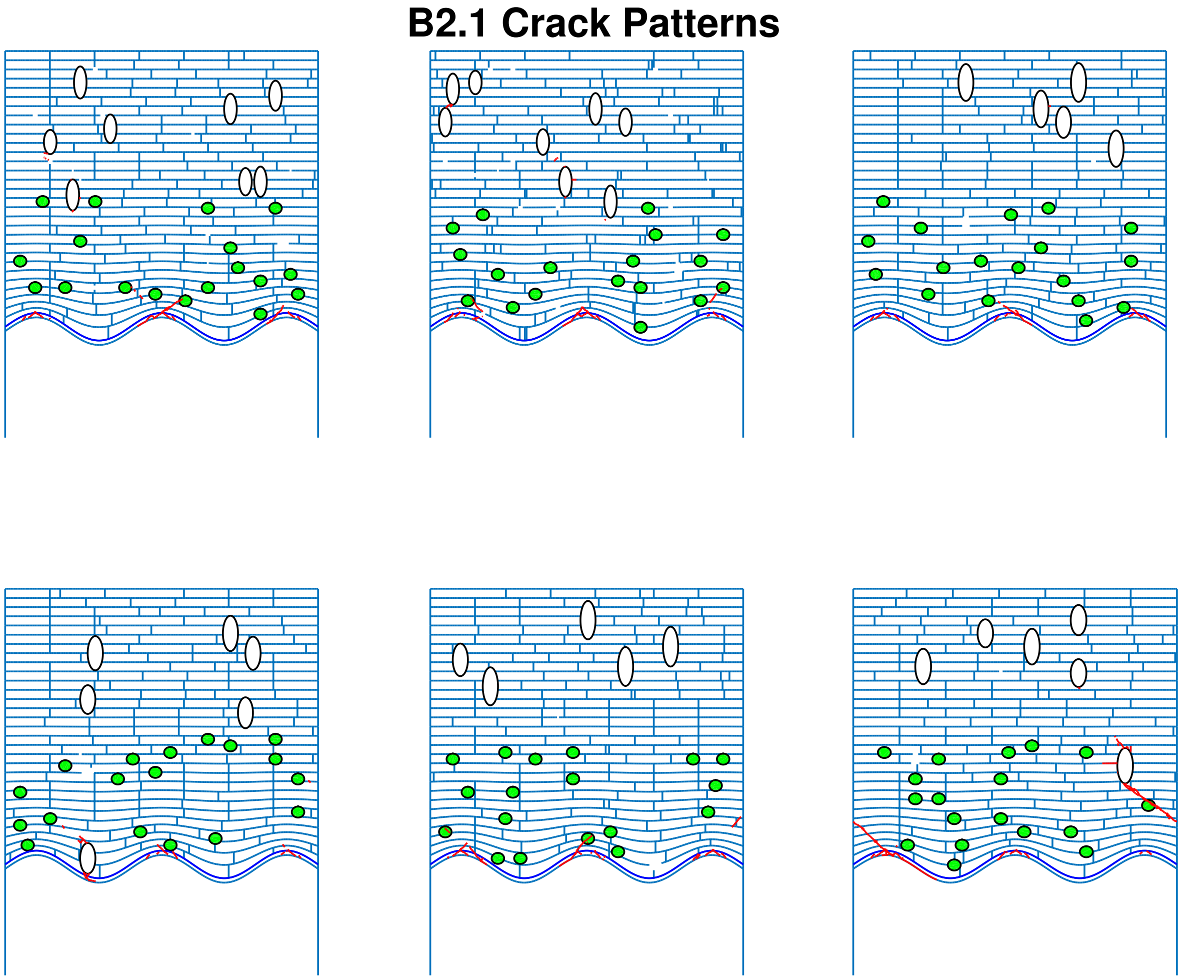

Figure B-1: **B2**.1 Crack Patterns

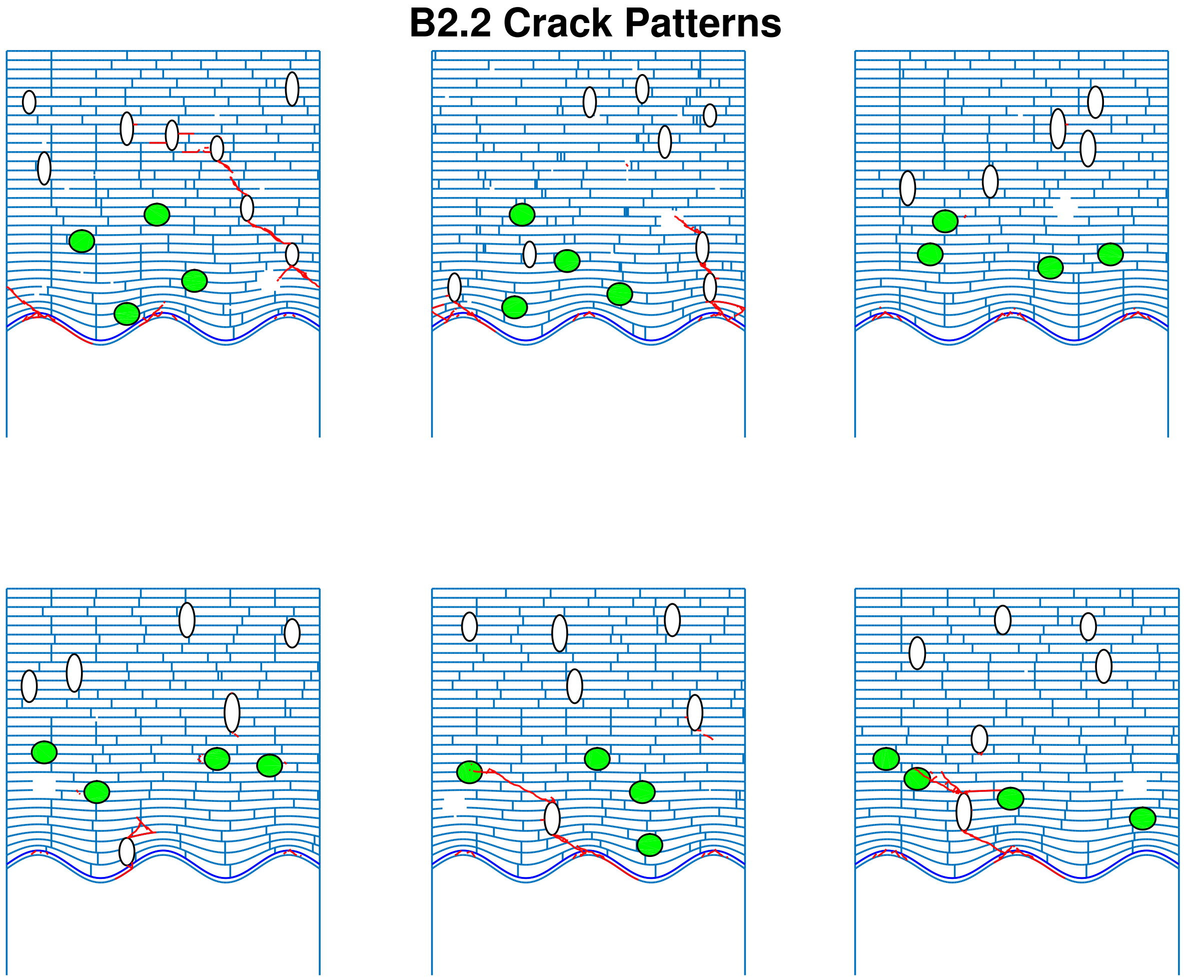

Figure B-2: B2.2 Crack Patterns

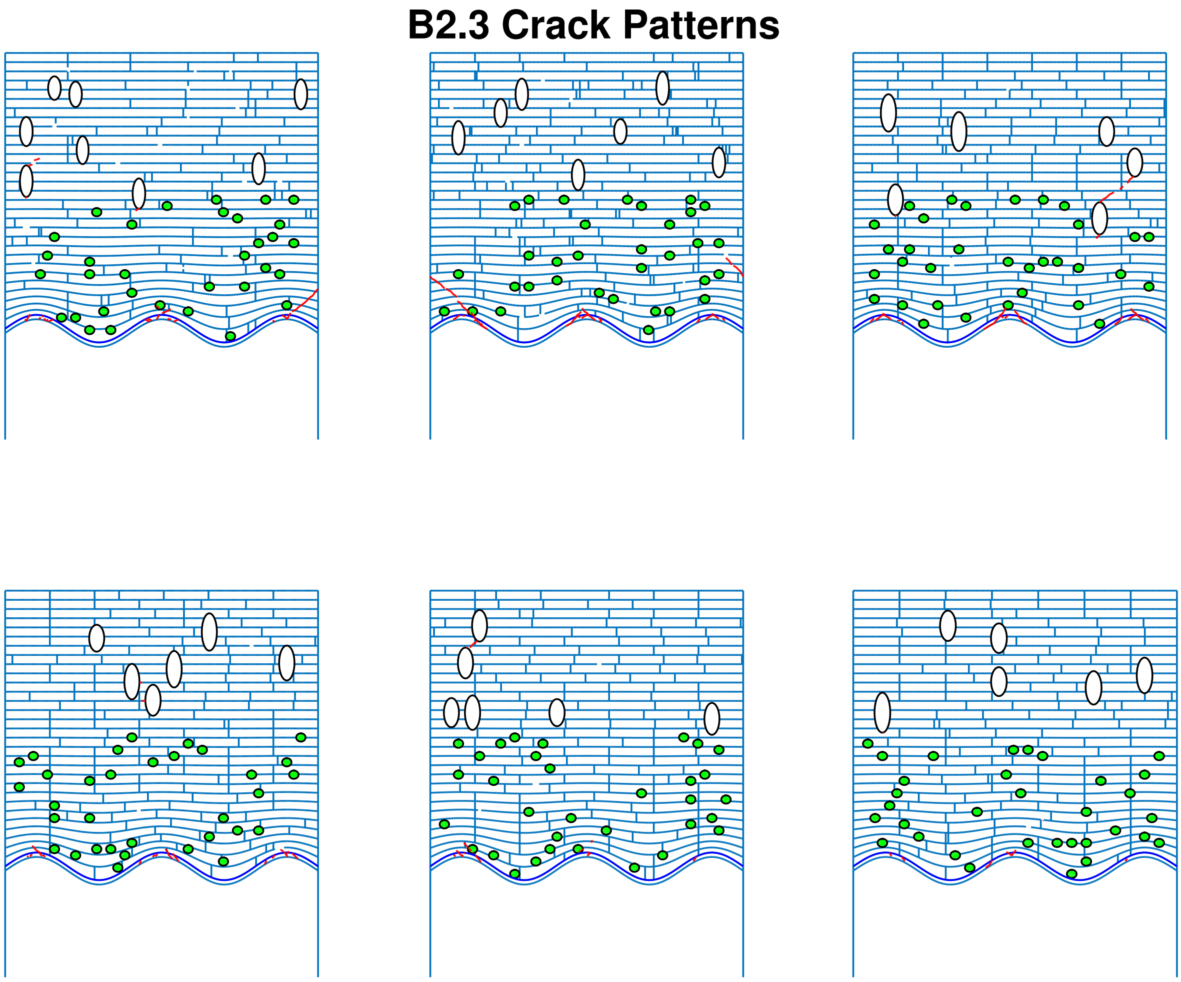

Figure B-3: **B2**.3 Crack Patterns

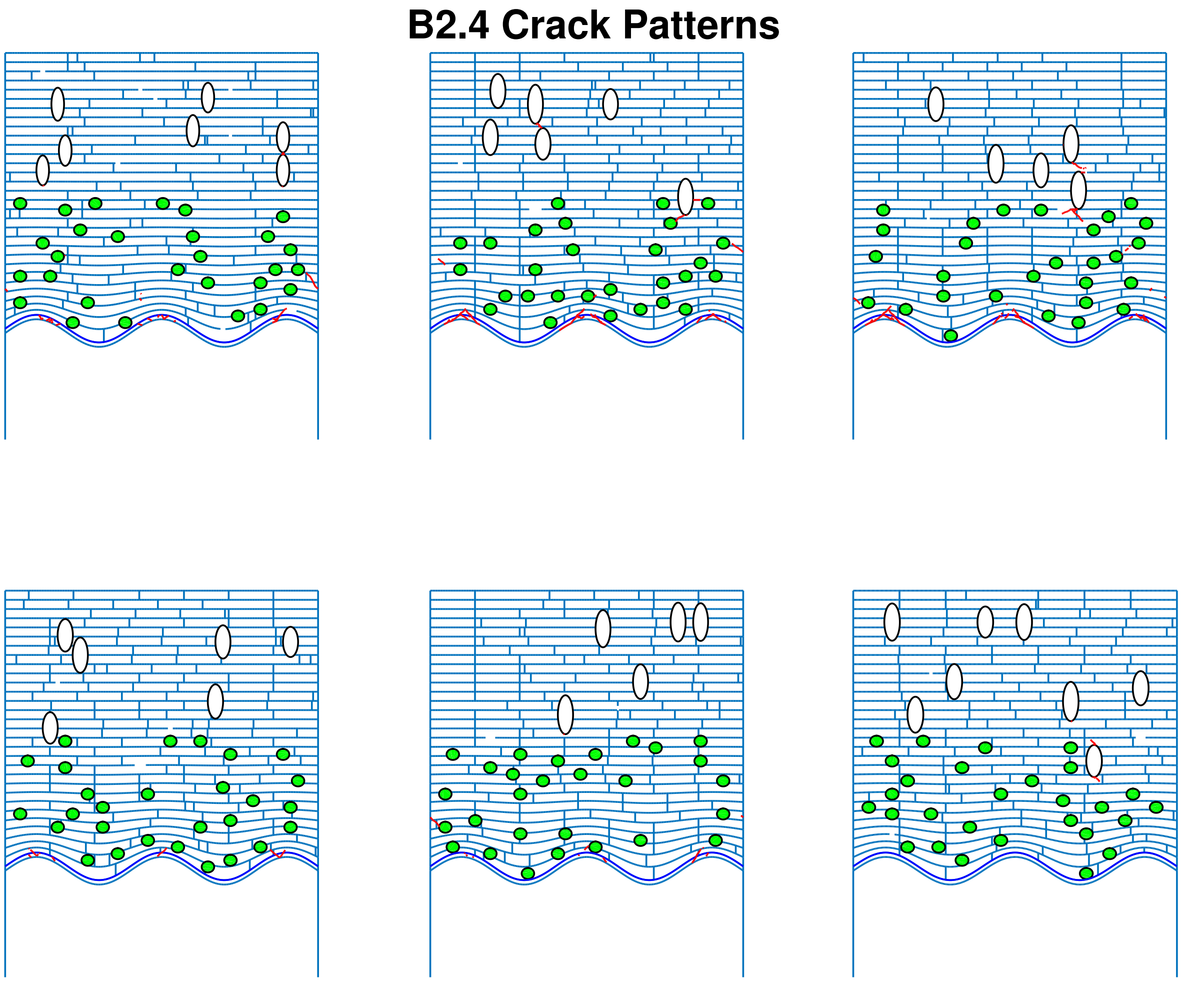

Figure B-4: B2.4 Crack Patterns

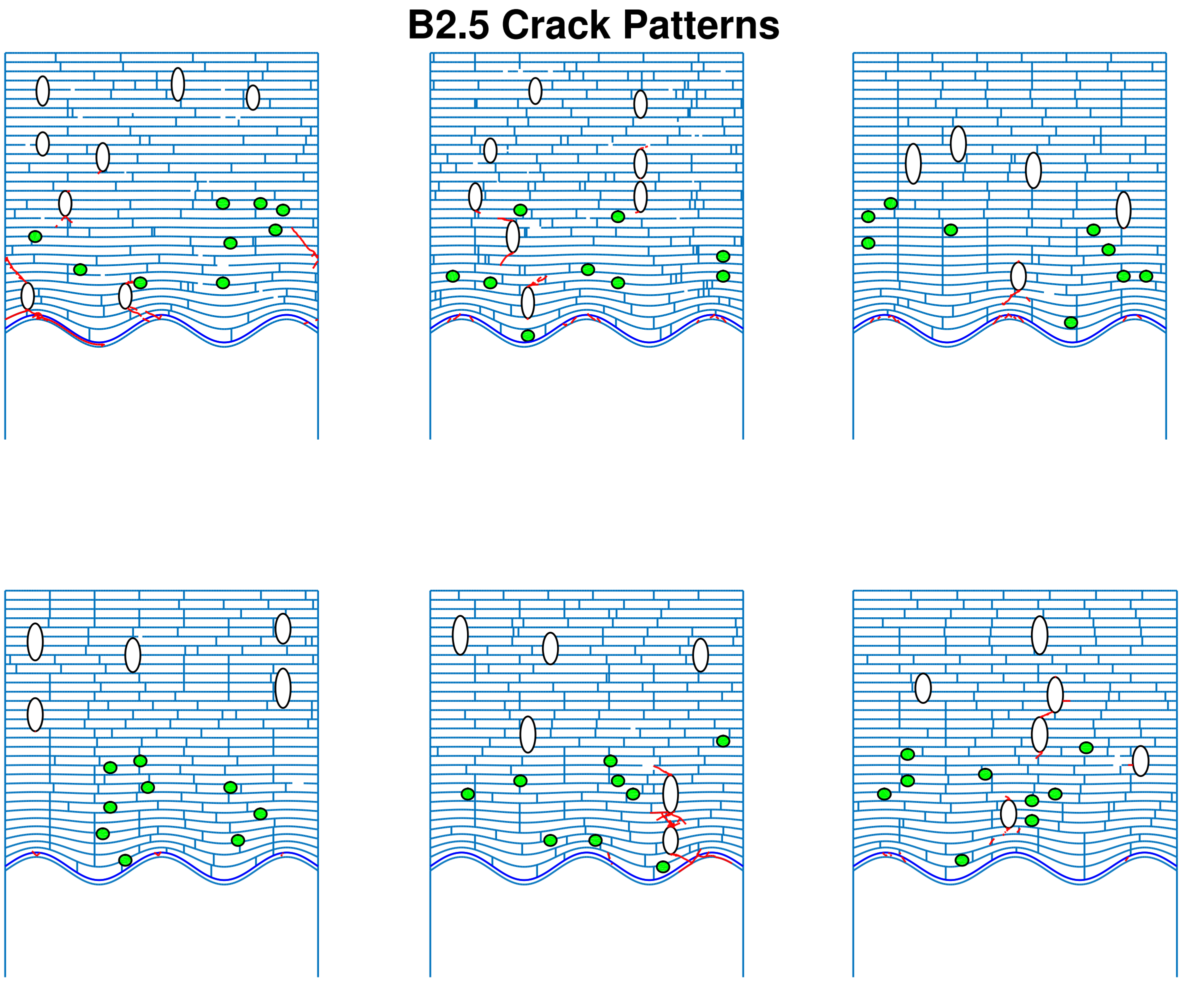

Figure B-5: **B2**.5 Crack Patterns